ENHANCING ICAL POTENTIAL WITH HADRONS,

AND DEVELOPMENT OF MULTIGAP RPC

By

Moon Moon Devi

PHYS01200904010

Bhabha Atomic Research Centre, Mumbai

A Thesis submitted to the
Board of Studies in Physical Sciences
in partial fulfillment of the requirements
for the Degree of

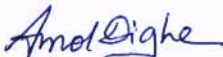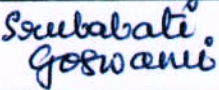# DOCTOR OF PHILOSOPHY

of

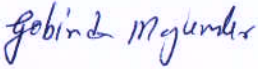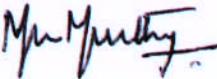# HOMI BHABHA NATIONAL INSTITUTE

September, 2015

Homi Bhabha National Institute

Recommendations of the Viva Voce Committee

As members of the Viva Voce Committee, we certify that we have read the dissertation prepared by Moon Moon Devi entitled "Enhancing ICAL Potential with Hadrons, and Development of Multigap RPC" and recommend that it may be accepted as fulfilling the thesis requirement for the award of Degree of Doctor of philosophy.
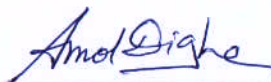
Chairman – Prof. V.M. Datar		Date:	14/9/15
Guide/Convener – Prof. A. Dighe	*Amol Dighe*	Date:	14/9/15
Examiner – Prof. S. Goswami	*Srubabati Goswami*	Date:	14/9/15
Member 1 – Dr. B. Satyanarayana		Date:	14/09/15
Member 2 – Prof. G. Majumder	*Gobind Majumder*	Date:	14/09/2015
Member 3 – Prof. M.V.N. Murthy	*M.V.N. Murthy*	Date:	14/9/15

Final approval and acceptance of this thesis is contingent upon the candidate's submission of the final copies of the thesis to HBNI.

I hereby certify that I have read this thesis prepared under my direction and recommend that it may be accepted as fulfilling the thesis requirement.

Date: 14/9/15

Place: Mumbai

Amol Dighe

Prof. Amol Dighe

Guide

STATEMENT BY AUTHOR

This dissertation has been submitted in partial fulfillment of requirements for an advanced degree at Homi Bhabha National Institute (HBNI) and is deposited in the Library to be made available to borrowers under rules of the HBNI.

Brief quotations from this dissertation are allowable without special permission, provided that accurate acknowledgement of source is made. Requests for permission for extended quotation from or reproduction of this manuscript in whole or in part may be granted by the Competent Authority of HBNI when in his or her judgement the proposed use of the material is in the interests of scholarship. In all other instances, however, permission must be obtained from the author.

Date: 14 – 09 – 2015

Place: Mumbai

Moon Moon Devi

(Enrolment Number PHYS01200904010)

DECLARATION

I, hereby declare that the investigation presented in the thesis has been carried out by me. The work is original and has not been submitted earlier as a whole or in part for a degree/diploma at this or any other Institution/University.

Date: 14 – 09 – 2015

Place: Mumbai

Moon Moon Devi

(Enrolment Number PHYS01200904010)

LIST OF PUBLICATIONS AND PREPRINTS

I. PUBLISHED

(1) M. M. Devi, A. Ghosh, D. Kaur, S. M. Lakshmi *et al.* "Hadron energy response of the Iron Calorimeter detector at the India-based Neutrino Observatory," JINST **8**, P11003 (2013), [arXiv:1304.5115 [physics.ins-det]].

(2) M. M. Devi, T. Thakore, S. K. Agarwalla and A. Dighe, "Enhancing sensitivity to neutrino parameters at INO combining muon and hadron information," JHEP **189**, 1410 (2014) , [arXiv:1406.3689 [hep-ph]].

(3) S. M. Lakshmi, A. Ghosh, **M. M. Devi**, D. Kaur *et al.* "Hadron energy resolution as a function of iron plate thickness at ICAL," JINST **9** T09003 (2014), [arXiv:1401.2779 [physics.ins-det]].
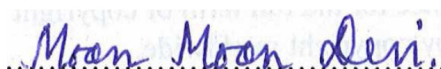
II. SUBMITTED

(1) M. M. Devi, N.K. Mondal, B. Satyanarayana, R.R. Shinde, "Development and performance study of glass multigap RPC detectors,"

III. MANUSCRIPT IN PREPARATION

(1) M. M. Devi, S. M. Lakshmi, A. Dighe and D. Indumathi "The hadron shower resonstruction at ICAL."

6

IV. CONFERENCE PROCEEDINGS

(1) M. M. Devi, T. Thakore, S. K. Agarwalla and A. Dighe, "Enhancing sensitivity to neutrino parameters at INO combining muon and hadron information," Proceedings of The Workshops on Neutrino Factories and Future Accelerator–based Neutrino Facilities (NuFact2014),

(2) M. M. Devi, N. K. Mondal, B. Satyanarayana, R. R. Shinde, "Performance of glass multi-gap RPC detectors," Proceedings of XII workshop on Resistive Plate Chambers and Related Detectors (RPC2014), submitted to JINST.

(3) M. M. Devi, N. K. Mondal, B. Satyanarayana, R. R. Shinde, "Development and characterization of glass multi-gap RPC detectors," Proceedings of the International Symp. on Nucl. Phys., PoS(ISNP2013)58.

(4) M. M. Devi, N. K. Mondal, B. Satyanarayana, R. R. Shinde, "Development and characterization of glass MRPC detectors," Proceedings of the DAE-BRNS National Symposium on Nuclear Instrumentation, PoS(NSNI2013).

(5) M. M. Devi, "A simulation study on the hadronic response of the INO-ICAL detector," Proceedings of the DAE Symp. on Nucl. Phys., PoS(SNP2011)56.

Moon Moon Devi

(Enrolment Number PHYS01200904010)

Dedicated to,

My Parents

ACKNOWLEDGEMENTS

Contents

SYNOPSIS

1. INTRODUCTION

The elusive neutrino has been among the most exciting particles since its postulation in 1930. The existence of neutrino was postulated by Pauli in a desperate attempt to save the 4–momentum and angular momentum conservations in nuclear β–decays [1]. After a wait of 26 years, it was detected experimentally in 1956, by Reines and Cowan [2, 3]. From then on, impressive results in the field of neutrino physics have amplified the excitement by many folds. Initially neutrino was assumed to be massless, which went well in accordance with the Standard Model of particle physics. However, the phenomenon of neutrino oscillations [4, 5], i.e, a propagating neutrino changing its flavour, implies that neutrinos are not massless, and thus opens a gateway for the physics beyond the standard model (BSM). The neutrino oscillations are parametrized in terms of a unitary transformation matrix connecting the flavor and mass eigenstates. In the 3–flavour basis, the elements of this matrix are expressed in terms of three mixing angles θ_{12}, θ_{13} and θ_{23}, and a CP violating phase δ_{cp}. The amplitude of the neutrino oscillations is determined by these three mixing angles, while the frequency is governed by the mass squared differences $\Delta m_{ij}^2 = m_i^2 - m_j^2$. The magnitude and sign of Δm_{21}^2 is established from our understanding of solar and reactor neutrino measurements. However in case of Δm_{31}^2 (or, Δm_{32}^2) only the magnitude is known, and the unknown sign of Δm_{31}^2 leads to two possible arrangements of the neutrino mass eigenstates. The normal mass hierarchy (NH) corresponds to

the ordering $m_1 < m_2 < m_3$, while the inverted hierarchy (IH) is with the ordering $m_3 < m_1 < m_2$. The hierarchy of the neutrino mass eigenstates can be confirmed once the sign of Δm_{31}^2 is determined.

Various experiments around the globe are now engrossed in exploring the neutrinos aiming at the determination of the mass hierarchy, the mixing parameters, leptonic CP violation and the absolute neutrino-mass scale. As a part of this effort the India-based Neutrino observatory (INO), a multi-institutional venture, has been initiated in India to build a underground neutrino laboratory [6]. The planned magnetized Iron Calorimeter (ICAL) detector at INO would study the oscillations in the atmospheric neutrinos in the GeV range. The ICAL will consist of the Resistive Plate Chamber (RPC) detectors as the active elements [7], interspersed with 5.6 cm thick iron plates. There will be 151 horizontal layers of the iron plates, with 4 cm gaps to place the RPC units. ICAL will be magnetized to about 1.5 Tesla. Three identical modules, of dimensions 16 m $\times$16 m $\times$14.4 m each, will be housed in a cavern with about 1 km of rock coverage, to reduce the cosmic muon background. It would mostly search for ν_μ induced charged current interactions in the iron target.

The ICAL aims at the determination of the neutrino mass hierarchy by exploring the matter effects for ν_μ and $\bar{\nu}_\mu$ separately, through the charge identification of the muons in the magnetic field. It will also look for precise estimation of the atmospheric mixing parameters (θ_{23} and $|\Delta m_{23}^2|$). Apart from these, ICAL would also explore the possibility of CPT violation, existence of the sterile neutrinos etc.

2. THE HADRON RESOLUTION OF ICAL

This is a GEANT4-based [8] simulation study to quantify the ICAL response to the hadrons, produced in the atmospheric neutrino interactions. The hits in the detector due to the hadrons are the observables in this work.

2.1 NEUTRINO INTERACTIONS IN ICAL

The atmospheric ν_μ and $\bar{\nu}_\mu$ interact with the iron target through quasi-elastic (QE), resonance scattering (RS) and deep inelastic scattering (DIS) processes. The charged-current (CC) interactions produce muons as well as hadrons. In the sub-GeV range, the QE process dominates, and apart from the recoil nucleons they do not have any other hadrons in the final state. As energy increases, RS and DIS processes start dominating and at a few GeV DIS becomes the most prominent process. Resonance events typically contain a single pion in the final state, though in a small fraction of events there are multiple pions. DIS events produce multiple hadrons. The momentum of the incident neutrino gets distributed among the final state particles i.e., the muon and the hadrons. The muon leaves a long track of hits in the detector with an average strip multiplicity per layer of about 1.4. The muon momentum is reconstructed using a Kalman Filter based algorithm [9]. The hadrons produce a shower, where the hits are confined to a few layers with a much higher strip multiplicity as compared to the muons. The hadron energy [10, 11] and direction [12] can be estimated using the shower hit information.

2.2 THE HADRON ENERGY CALIBRATION AND RESOLUTION

The propagation of particles in the ICAL detector is simulated using the GEANT4 package, taking into account the realistic input parameters of the RPC detectors and the magnetic field. This simulation provides the location of the passage of the particle in the X and Y strips of the RPC layers. As the hadron shower contains multiple hits per layer, the possibility of false counting (ghost hit) is reduced by using the maximum of X or Y hits for each event. Firstly, $\pi^\pm$, π^0, $K^\pm$, K^0 and protons of certain fixed energies are propagated through ICAL, and it is seen that ICAL cannot distinguish among individual hadrons. Then, the hadrons produced in the atmospheric neutrino interactions, generated using NUANCEv3.5 [13] event generator, are propagated through the detector.

The visible hadron energy depends on various factors such as, the shower energy fluctuation, leakage of energy and invisible energy loss mechanisms. To quantify the ICAL response to hadrons, we use the parameter E'_{had} [10] as

$$E'_{\text{had}} = E_\nu - E_\mu \ . \tag{1}$$

Note that, E'_{had} includes the visible and invisible hadron energies, as well as the energy of the recoil nucleons. All type of hadrons contribute to this energy, however at a few GeV it is dominated by pions.

A typical hadron hit distribution at $E'_{\text{had}} = (3.5 - 3.75)\,\text{GeV}$ for hadrons produced in the neutrino interactions in ICAL is shown in Fig 1a. These distributions are not symmetric and have long tails. After trials of fits with various probability distribution functions (PDF) such as, Gaussian, Landau, Landau convoluted with a Gaussian etc., a good fit is obtained with the Vavilov distribution function [14, 15]. The Vavilov function expresses the energy loss by particles propagating in moderately thick absorbers. The standard Vavilov distribution is described by the two parameters κ and β^2. For $\kappa \leq 0.05$, the Vavilov distribution may be approximated by the Landau distribution, while for $\kappa \geq 10$, it approaches the Gaussian approximation.

The Vavilov PDF is built into the analysis software package ROOT [16], and is modified with extra parameters P_2, P_3 and P_4 to account for x-scaling, the shifting of the peak to a non zero value and normalization, in order to fit the hadron hit distributions. The mean and variance of this modified PDF are

$$\text{Mean}_{\text{Vavilov}} = (\gamma \ - \ 1 \ - \ \ln \kappa - \beta^2)\,\text{P}_3 + \text{P}_2 \ , \quad \sigma^2_{\text{Vavilov}} = \frac{(2 - \beta^2)}{2\kappa}\text{P}_3^2 \ . \tag{2}$$

Using these parameters, the hit distributions can be reproduced.
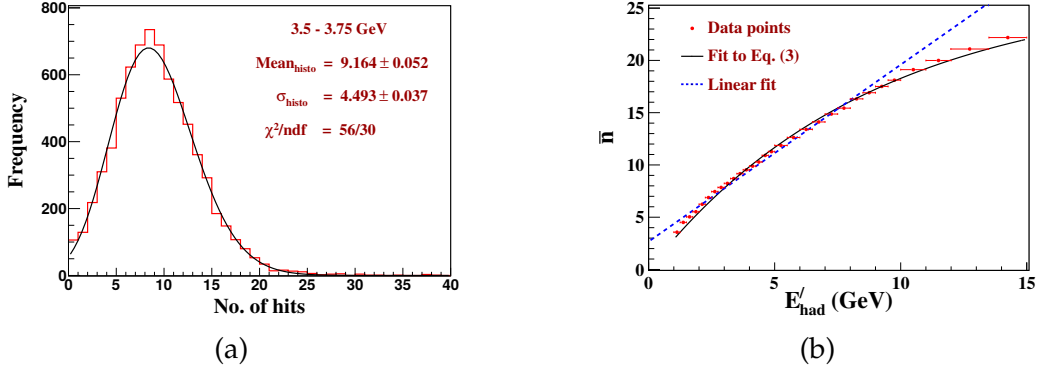
Figure 1: (a) The hadron hit distribution at $E'_{\text{had}} = (3.5 - 3.75)$ GeV, fitted to the Vavilov PDF. (b) The mean number of hits from the Vavilov fit, as a function of E'_{had}. A linear fit and a fit to Eq. (3) are also shown. [10]

As shown in Fig. 1b, the mean hit ($\bar{n}$) increases with the increase in hadron energy, and saturates at higher energies. It may be approximated by

$$\bar{n}(E'_{\text{had}}) = n_0[1 - \exp(-E'_{\text{had}}/E_0)] \, , \tag{3}$$

where n_0 and E_0 are constants. The value of E_0 is ~ 27 GeV for the E'_{had} range $(0 - 15)$ GeV. When $E'_{had} \ll E_0$, the increase in $\bar{n}$ with E'_{had} is linear. Using linear approximation, the hadron energy resolution can be defined as

$$\sigma/E = \Delta E'_{\text{had}}/E'_{\text{had}} = \Delta n(E'_{\text{had}})/\bar{n}(E'_{\text{had}}). \tag{4}$$

The $\sigma/$E may be parameterized by

$$\frac{\sigma}{E} = \sqrt{\frac{a^2}{E} + b^2} \, , \tag{5}$$

where a and b are constants. The hadron energy resolution of ICAL as a function of E'_{had} is shown in Fig. 2a. The energy resolution ranges from 85% (at 1 GeV) to 36% (at 15 GeV). Similar response have been obtained from the hadrons produced in the neutral current interaction processes. The hadron energy resolution is also studied as a function of the iron plate thickness [11].
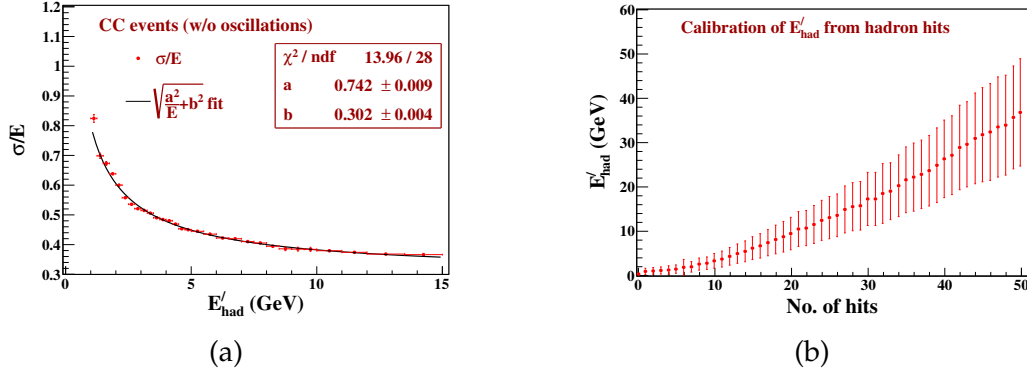
Figure 2: (a) The energy resolution for hadrons generated by NUANCEv3.5, as a function of E'_{had}. A fit to Eq. (5) is also shown. (b) Calibration plot for E'_{had}. The mean E'_{had} and the standard deviation σ from the Vavilov fits are represented by the circles and the error bars, respectively.[10]

The shower hits will be the only observable parameter for the hadrons, when the real ICAL detector starts taking data. Thus a calibration of the hit multiplicity with the E'_{had} becomes essential to reconstruct the hadron energy. The E'_{had} distributions for the events binned in hadron hits are fitted with Vavilov distribution function, and the mean and σ from this fit are used to produce the calibration as shown in Fig. 2b. This calibration can be used to estimate the E'_{had}. A look up table containing the Vavilov fit parameters is used to include the hadron response in the analysis to determine the physics reach of ICAL.

2.3 RECONSTRUCTION OF THE HADRON SHOWER DIRECTION

It is difficult to reconstruct the average direction of the hadron showers as accurately as that of muons. Still it is possible to use the position information of the hadron shower hits in the detector and reconstruct the shower direction [12]. When the muon track gets reconstructed in a CC event, the position vectors of the shower hits with respect to the reconstructed interaction vertex can be used. Two methods, namely the centroid method and the orientation matrix method have been used in such cases.

The direction of the centroid of the shower is reconstructed by summing over the position vectors (with respect to the vertex) of each hit in that event. However the accuracy of reconstruction may be slightly increased by taking into account the higher order moments by the use of the orientation matrix technique [17]. In this method, for a collection of unit vectors (x_i, y_i, z_i), $i = 1, ..., n$, the orientation matrix T is defined as

$$T = \begin{pmatrix} \Sigma x_i^2 & \Sigma x_i y_i & \Sigma x_i z_i \\ \Sigma x_i y_i & \Sigma y_i^2 & \Sigma y_i z_i \\ \Sigma x_i z_i & \Sigma y_i z_i & \Sigma z_i^2 \end{pmatrix}. \tag{6}$$

The eigenanalysis of this symmetric matrix gives an idea of the shape of the underlying distribution. If we think of a unit mass being placed at each point, then the variation of the moment of inertia of these n points about any arbitrary axis would provide information about the scatter of the points. The axis about which the moment of inertia is least is defined to be the shower direction. The MIGRAD minimizer algorithm, which is inbuilt in TMinuit class in ROOT has been used for the minimization of the moment.

The hadron shower direction resolution is obtained to be in the range of $(15° - 5°)$. Further, the spread of hits with respect to this direction can also be used to distinguish between the shower due to RS and DIS processes. Since RS events mostly produce a pion, the shower would be confined to a narrower cone compared to the shower produced by multiple hadrons in DIS events.

2.4 THE NEUTRINO ENERGY AND DIRECTION RESOLUTIONS

The energy and direction of the incident neutrino have been estimated from the reconstructed momentum of the final state particles through the application of the 4–momentum conservation [12]. The neutrino energy is reconstructed by adding up the reconstructed energies of the muon and the hadrons in each event. For the events fully confined in ICAL, the energy resolution of neutrinos in the ICAL is in

the range $(22 - 26)\%$, whereas for the partially contained events in the detector it is $\sim 30\%$.

The muon and hadron momentum information is used to calculate the X, Y and Z projections of the neutrino momenta and eventually the neutrino direction. The resolution of the neutrino zenith angle at the ICAL is in the range $(19° - 7.5°)$. In an alternative approach, the neutrino direction has also been estimated from the average scatter angle between the incident neutrino and the reconstructed final state muon.

3. ENHANCING THE PHYSICS REACH OF ICAL WITH HADRONS

The initial analysis of the physics potential of ICAL was performed using the muon momentum (E_μ, $\cos\theta_\mu$) only [18, 19]. The ICAL capability of measuring the hadron energy, though with a relatively poorer resolution, provides additional information on the incident neutrino energy. This information is expected to enhance the ICAL physics reach. The hadron energy can be added to the analysis in multiple ways. First the neutrino momentum (E_ν, $\cos\theta_\nu$) was used in place of the muon momentum. However this gives poorer mass hierarchy (MH) sensitivity than the muon-only analysis. The main drawback is that while adding E_μ and E'_{had} to calculate E_ν, the advantage of high precision in the E_μ measurement is partially lost due to the coarser estimation of E'_{had}. Another approach with (E_ν, $\cos\theta_\mu$) improves the MH result slightly over the neutrino-only analysis, yet it is not even at par with the result obtained using muon momentum. However, treating E_μ and E'_{had} as two separate variables improve the result significantly. In this approach, the correlation between these two quantities in each event is included in the study. The enhancement of the ICAL physics potential with the inclusion of hadron energy has then been obtained using the values E_μ, $\cos\theta_\mu$ and E'_{had} from each event as independent variables [20].

The analysis procedure is discussed in the following.

3.1 THE ANALYSIS PROCEDURE

1. **Event Generation:** NUANCEv3.5, with the ICAL specifications as input, is used as the Monte Carlo event generator to produce atmospheric neutrino interactions. The atmospheric neutrino flux provided by Honda et al. at the Super Kamiokande site is used [21]. In order to minimize the statistical fluctuations, CC ν_μ events are produced for a large exposure of 50000 kt – yr and then scaled down to the required exposures. Producing events with such a large exposure at all possible sets of the oscillation parameters is practically impossible, so the event generator is run only once for un-oscillated neutrino flux, and later a re-weighting algorithm is used to incorporate the oscillations.

2. **Inclusion of the oscillations and detector response:** The events are re-weighted using a random selection algorithm. The survival/ oscillation probabilities for the certain channel is calculated [22] using the given set of oscillation parameters. The benchmark values of the oscillations parameters are used as in [23, 24, 25]. Then for each event, a uniform random number R between 0 and 1 is generated and compared to the probability to pick/discard that event. The re-weighted events are then binned in the observables (E_μ, $\cos\theta_\mu$, E'_{had}) and folded with the ICAL response. The ICAL lookup tables for both muon and hadron response are used. First, the events in each bin were multiplied by the muon reconstruction efficiency and CID efficiency. Then the integrals of the detector response functions of the three observables are evaluated, and using them the measured distribution of the events are obtained.

3. **The χ^2 analysis:** For the χ^2 analysis the events are re-distributed in wider and non-uniform bins, the bin widths being comparable to the respective resolutions. A scheme of 20 E_μ bins in the range $(1 - 11)$ GeV, 21 $\cos\theta_\mu$ bins in the range $[-1, +1]$, and 4 $E'_{\rm had}$ bins in the range $(0 - 15)$ GeV are used for each polarity of muon.

The Poissonian $\chi^2_\pm$ for events with a $\mu^\pm$ is defined as

$$\chi^2_\pm = \min_{\xi_l} \sum_{i=1}^{N_{E'_{\rm had}}} \sum_{j=1}^{N_{E_\mu}} \sum_{k=1}^{N_{\cos\theta_\mu}} \left[2(N_{ijk}^{\rm theory} - N_{ijk}^{\rm data}) - 2N_{ijk}^{\rm data} \ln\left(\frac{N_{ijk}^{\rm theory}}{N_{ijk}^{\rm data}}\right) \right] + \sum_{l=1}^{5} \xi_l^2 .$$
(7)

The following five systematic errors are included in the analysis using the method of pulls [26] : (i) Flux normalization error (20%), (ii) cross–section error (10%), (iii) tilt error (5%), (iv) zenith angle error (5%), and (v) overall systematics (5%). The total χ^2 is obtained by adding the individual contributions from μ^- and μ^+ events and a 8% prior (at 1σ) on $\sin^2 2\theta_{13}$.

$$\chi^2_{\rm ICAL} = \chi^2_- + \chi^2_+ + \chi^2_{\rm prior} .$$
(8)

This $\chi^2_{\rm ICAL}$ is marginalized over the pull variables ξ_l and over the 3σ allowed range of the relevant oscillation parameters.

3.2 THE MASS HIERARCHY SENSITIVITY OF ICAL

The statistical significance of the analysis to discard the wrong hierarchy is quantified by

$$\Delta\chi^2_{\rm ICAL-MH} = \chi^2_{\rm ICAL}({\rm false\ MH}) - \chi^2_{\rm ICAL}({\rm true\ MH}),$$
(9)

where $\chi^2_{\rm ICAL}$ (true MH) and $\chi^2_{\rm ICAL}$ (false MH) are obtained by performing a fit to the *observed* data assuming true and false mass hierarchy, respectively.

The comparison of the $\Delta\chi^2_{\text{ICAL-MH}}$ obtained in this analysis with that from the muon-only analysis is shown in Fig. 3a, as a function of the ICAL run–time for true NH. After including the E'_{had} information, 10 years of running can rule out the wrong hierarchy with $\Delta\chi^2_{\text{ICAL-MH}} \approx 9.5$ (for true NH), and $\Delta\chi^2_{\text{ICAL-MH}} \approx 8.7$ (for true IH), which mark an improvement of about 40% over the muon-only analysis. Fig. 3b shows the range of $\Delta\chi^2_{\text{ICAL-MH}}$ for different true $\sin^2\theta_{23}$.

(a)   (b)
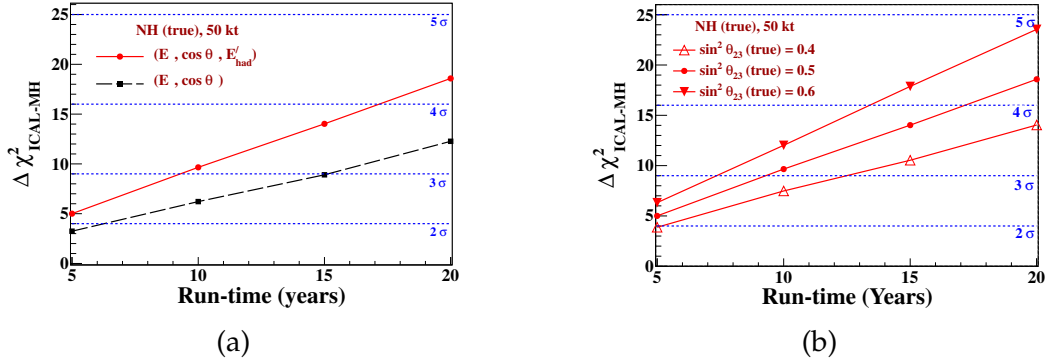
Figure 3: (a) $\Delta\chi^2_{\text{ICAL-MH}}$ as a function of the run-time assuming NH as true hierarchy. The red line shows the results with hadron information, while the black dashed line shows the same without including hadron information. (b) The variation of $\Delta\chi^2_{\text{ICAL-MH}}$ for different true values of $\sin^2\theta_{23}$. The value of $\sin^2 2\theta_{13}$ (true) is taken to be 0.1 and NH is assumed to be the true hierarchy. [20]

3.3 PRECISION ON θ_{23} and $|\Delta m^2_{32}|$

The precision in the measurements of the parameter λ ($\lambda = \sin^2\theta_{23}$ or $|\Delta m^2_{32}|$), is quantified as

$$\Delta\chi^2_{\text{ICAL-PM}}(\lambda) = \chi^2_{\text{ICAL-PM}}(\lambda) - \chi^2_0 \,, \tag{10}$$

where χ^2_0 is the minimum value of $\chi^2_{\text{ICAL-PM}}$ in the allowed parameter range. It is observed that with the inclusion of E'_{had} information, 500 kt–yr of ICAL exposure would be able to measure $\sin^2\theta_{23}$ to a relative 1σ precision of 12% and $|\Delta m^2_{32}|$ to 2.9%. With the muon-only analysis, the same relative precisions would be 13.7% and 5.4%, respectively. The $\sin^2\theta_{23}$ precision mainly depends on the event statistics, which is not changed by the addition of the E'_{had} information, thus only a small difference is observed in the two analyses. However, independent measurements of E_μ and E'_{had}

31

corresponds to a better estimation of E_ν, which appears in the oscillation expression as $\sin^2(\Delta m^2 L/E_\nu)$, thus leading to a significant improvement of the measurement of Δm^2_{32}. Fig. 4a shows the comparison of $\Delta\chi^2_{\text{ICAL}-\text{PM}} (\Delta m^2_{32})$, with and without hadron energy information. The ICAL $500\,\text{kt}-\text{yr}$ projected reach has been compared to the current results from other experiments in Fig. 4b.

(a)   (b)
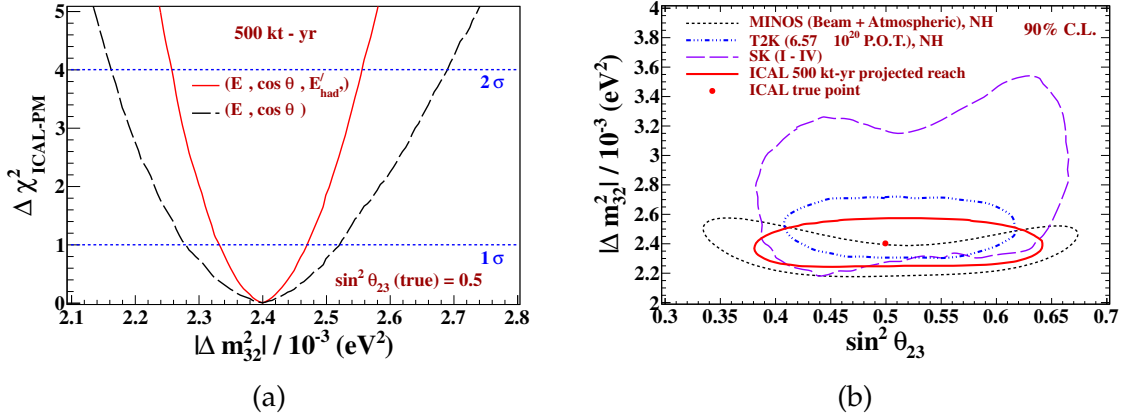
Figure 4: (a) $\Delta\chi^2_{\text{ICAL}-\text{PM}} (\Delta m^2_{32})$, with and without hadron energy information. The true hierarchy is assumed to be NH. (b) 90% C.L. (2 dof) contours in the $\sin^2\theta_{23} - |\Delta m^2_{32}|$ plane. The current limits from Super- Kamiokande [27], MINOS [28], and T2K [29] have been shown along with the projected ICAL reach for the exposure of 500 kt-yr, assuming true NH. [20]

3.4 OCTANT OF θ_{23}

In analogy with the MH discovery potential the statistical significance of the analysis to rule out the wrong octant of θ_{23} is defined as

$$\Delta\chi^2_{\text{ICAL}-\text{OS}} = \chi^2_{\text{ICAL}}(\text{false octant}) - \chi^2_{\text{ICAL}}(\text{true octant}). \qquad (11)$$

It is observed that the potential of distinguishing the θ_{23} octant with the ICAL data alone is rather weak. A 2σ identification of the octant is possible with the 500 kt–yr ICAL data alone only when the true hierarchy is NH and the true octant is LO ($\sin^2\theta_{23}(\text{true}) < 0.395$).

4. DEVELOPMENT OF MULTIGAP RPC DETECTORS

The Multigap Resistive Plate Chambers (MRPCs) [30] are gas ionization detectors with multiple gas sub–gaps made of highly resistive electrodes. The high voltage (HV) is applied at the outer surfaces of the two outermost resistive plates only, while the interior plates are left electrically floating. The presence of multiple gas sub-gaps enables the detector to induce faster signals on the outer electrodes, thus improving the detector's time resolution. MRPCs have been chosen as optimal elements for many Time–Of–Flight (TOF) detector systems (including ALICE and STAR) due to their excellent time resolution (< 100 ps) and higher efficiency for particle detection [31, 32]. A typical single-gap RPC detector, designed for ICAL, has a time resolution of $\sim (1 - 1.5)$ ns. The use of MRPCs in ICAL would enable us to use the time count of the hits efficiently, and is likely to further improve the direction reconstructions of the muon and the hadron shower. In this work, glass MRPCs with 6 sub-gaps are developed and characterized to probe their potential applications in future ICAL upgrades, as well as in TOF experiments, imaging etc.

4.1 FABRICATION

MRPCs with 6 sub-gaps and of dimensions 305 mm $\times 305$ mm $\times 7.5$ mm are designed and fabricated. Glasses of 2 mm thickness with a conductive coat are used for the outer electrodes. The intermediate glass plates are 400 μm thick.

Small circular spacers of diameter 4 mm, which are made of two sided non conducting adhesive tapes, are used to maintain 250 μm gaps between floating electrodes. The configuration is optimized with sealing the gas gaps by gluing side spacers between the outermost electrodes. To ensure a proper gas flow through the sub–gaps, appropriate blockers are placed. The pickup panel consists of honeycomb panels laminated with copper strips of width 2.8 cm. Figure 5 shows a schematic diagram of the MRPC detector configuration.
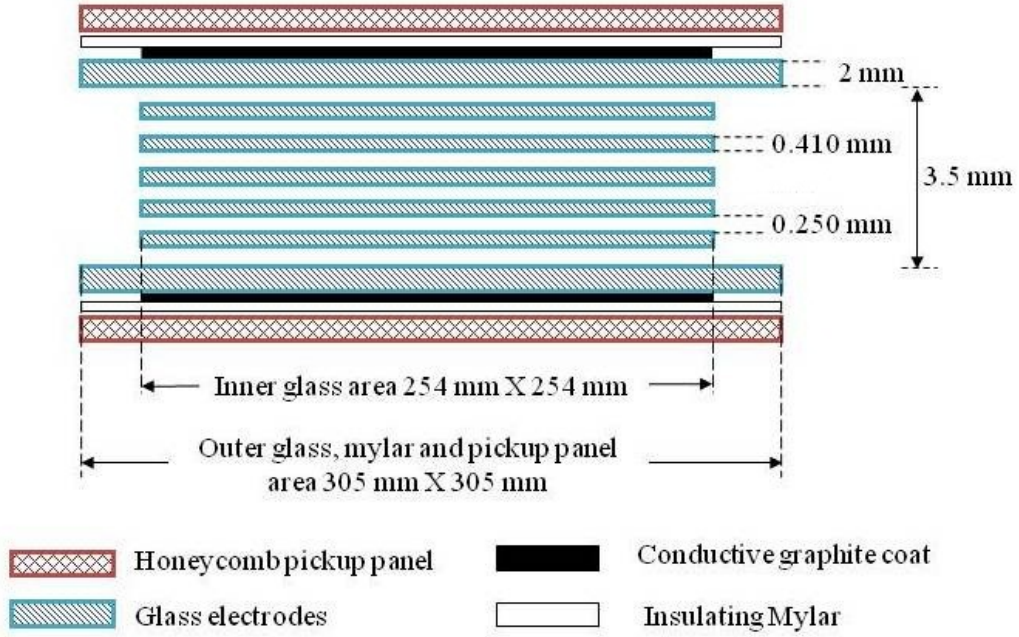
Figure 5: The configuration of the MRPC.

4.2 DETECTOR SETUP AND DATA ACQUISITION

The MRPCs are tested and characterized in avalanche mode using a cosmic muon telescope consisting of three scintillator paddles (two on the top of the MRPCs under test and one at the bottom) The coincidence signal from these three paddles are used to trigger the data acquisition system. Signals from the MRPC pickup strips are amplified using NINO ASIC [33] and then taken with the time coincidence of the trigger.

A CAMAC based data acquisition (DAQ) system for the MRPC detector test is set up to record the strip counting rate, strip efficiency and time count. The efficiency is recorded with respect to the trigger through a 2–fold coincidence. The start and stop to the TDC counter are given by the trigger and MRPC signal respectively, and the corresponding time count are recorded.

4.3 CHARACTERIZATION

The MRPCs are operated in avalanche mode using the standard gas mixture of R134a, C_4H_{10} and SF_6. The MRPC characteristics such as the strip counting rate, chamber current, efficiency and time resolution are studied as a function of the concentration of the gas mixture. Based on this study, the gas mixture is optimized to R134a (91%), C_4H_{10} (5%), and SF_6 (4%).
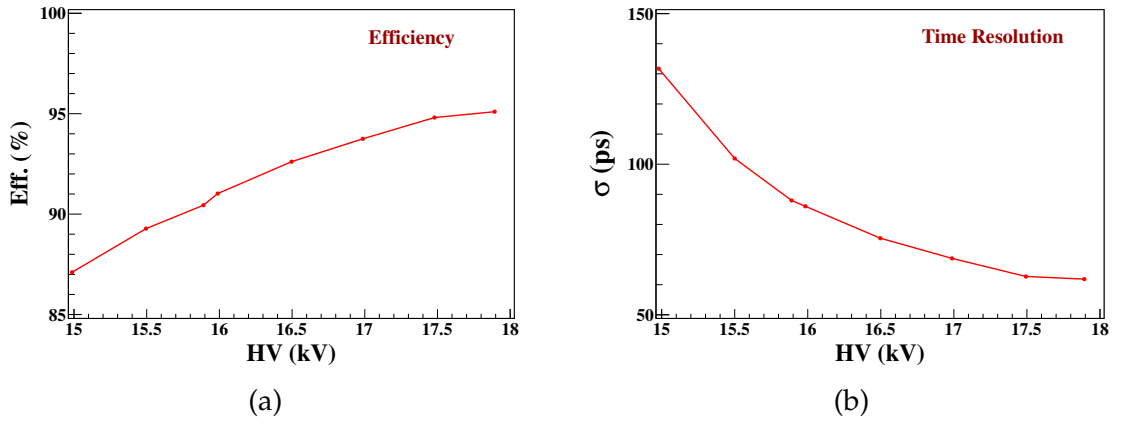
Figure 6: (a) The efficiency and (b) the time resolution of the MRPC as a function of the applied high voltage.

The efficiency and time resolution of the MRPC with the optimized gas mixture, as a function of the applied high voltage, are shown in Fig. 6. The efficiency increases with the high voltage, and reaches about 95% at 17.9 kV. The time distributions are corrected for the time jitter through an off line calibration of the time count with the charge count of the signal. Note that, for this calibration NINO ASIC is replaced by Anusparsh, which is designed for the ICAL experiment, as the later also provides the analog output required to obtain the charge count. A time resolution of ~ 60 ps is obtained at 17.9 kV. The MRPC is also tested with a Cs-137 source. This reduces the jitter due to the spread in location of the incident particle, and improves the time resolution further by about 10 ps. Thus the introduction of the sub-gaps results in a much improved time resolution over the single-gap configuration which has a typical time resolution in the range of $(1-1.5)$ ns.

In addition, MRPCs with their fast timing characteristics, can reduce the jitter in a trigger scheme. This is confirmed by including an MRPC in the trigger set-up of scintillator paddles, to test a single gap RPC. The inclusion of the MRPC reduces the time jitter in the trigger by 50%.

5. SUMMARY AND FUTURE SCOPE

5.1 SUMMARY

The INO collaboration plans to study the neutrino oscillations in the atmospheric sector, with the 50 kt ICAL detector. Though primarily designed to measure the muon momentum, ICAL is also capable of detecting the hadron shower and measure its momentum. A simulation study is performed to quantify the hadron energy resolution of ICAL using the shower hit information. The hadron energy, parametrized in terms of $E'_{\mathrm{had}} \equiv E_\nu - E_\mu$, is estimated from the hadron hit multiplicity which follows the Vavilov PDF. A calibration of E'_{had} for the number of hadron hits in an event has been obtained. The hit positions are used to reconstruct the average direction of the hadron shower using orientation matrix technique. The hadron momentum information is further used to obtain the neutrino response of the ICAL.

The reach of ICAL is then studied using the correlated information on the muons and the hadrons. The inclusion of the hadron information improves the ICAL physics potentials by significant amounts. It is found that the ICAL, with 500 kt–yr exposure, would be able to determine the neutrino mass hierarchy with a significance of $\Delta\chi^2_{\mathrm{ICAL-MH}} \sim 9$, which implies about 40% enhancement over the muon-only analysis. The atmospheric neutrino mixing parameters can also be measured more precisely by the inclusion of hadron energy information.

MRPC detectors, with six sub-gaps in each of them, have been developed and characterized in order to probe their potential in the future upgrades of ICAL as well as other applications such as, TOF experiment. The design of the single cell structure has been optimized. These detectors are operated in the avalanche mode with a optimized gas mixture, and their efficiency, time resolution, strip counting rate etc have been studied using a CAMAC based DAQ system. A time resolution of $\sim$ 60 ps is obtained at 17.9 kV.

The MRPCs are tested as a part of the external trigger system consisting of scintillators to characterize single gap RPCs, which shows 50% reduction in the time jitter of the trigger. A stack of four MRPCs is now fully operational.

5.2 FUTURE SCOPE

The separation of the muon track and the hadron shower hits would be crucial to use the real data, once ICAL becomes operational. Thus a simulation study to develop an efficient track-shower separation algorithm is important. Also, the neutrino response of the ICAL is coarse, and can be improved by stricter cuts, and with possible improvement in the measurements of the muon momentum and the hadron momentum. The inclusion of the hadron shower direction as the fourth independent variable in the oscillation analysis may be checked for further improvements. A promising work is to modify the oscillation analysis algorithm to study the ICAL potential to detect the sterile neutrinos. The MRPC detectors show good detection efficiency and time resolution, and now they are ready to be tested for possible applications as trigger detector, and in TOF experiments.

List of Tables

List of Figures

LIST OF ABBREVIATIONS

AGN   Active Galactic Nuclei

ASIC   Application – Specific Integrated Circuit

CAMAC   Computer Automated Measurement And Control

CC   Charged – Current

CERN   Conseil Europen pour la Recherche Nuclaire,

  i.e., The European Organization for Nuclear Research

CMB   Cosmic Microwave Background

DAQ   Data Acquisition

DIS   Deep Inelastic Scattering

ECL   Emitter – Coupled Logic

FC   Fully – Contained

FWHM   Full Width at Half Maximum

GEANT   GEometry And Tracking

GRB   Gamma Ray Burst

HV   High Voltage

HWHM   Half Width at Half Maximum

ICAL   Iron CALorimeter

IH   Inverted Hierarchy

INO   India–based Neutrino Observatory

KamLAND Kamioka Liquid Scintillator Anti Neutrino Detector

KS   Kolmogorov – Smirnov

LVDS	Low – Voltage Differential Signaling
MH	Mass Hierarchy
MINOS	Main Injector Neutrino Oscillation Search
MRPC	Multigap Resistive Plate Chamber
MSW	Mikheyev – Smirnov – Wolfenstein
NC	Neutral – Current
NH	Normal Hierarchy
NIM	Nuclear Instrumentation Module
OS	Octant Sensitivity
PDF	Probability Distribution Function
PM	Precision Measurement
PREM	Preliminary Reference Earth Model
QE	Quasi – Elastic
RENO	Reactor Experiment for Neutrino Oscillations
RPC	Resistive Plate Chamber
RS	Resonance Scattering
SCCM	Standard Cubic Centimeter per Minute
SLAC	Stanford Linear Accelerator Center
SK	Super Kamiokande
SNO	Sudbury Neutrino Observatory
SSM	Standard Solar Model
TDC	Time – to – Digital Converter
TOF	Time – Of – Flight

Chapter 1

INTRODUCTION

So close, yet so far,

Let's bring them nearer and nearer!

Right from its postulation in the early 20th century, the neutrino has been among the most exciting particles. It stands second in the list of the most abundant particles in the universe, next only to the photons. However, it rarely interacts with matter via weak force, and thus, is very difficult to detect. Intense amount of work is going on now, in various parts of the world, for detecting neutrino and studying its salient features. This thesis attempts a tiny contribution to this ongoing effort.

This chapter focuses on the concept of the elusive neutrino, its features, motivation for experimental study and a brief overview of the India–based neutrino observatory (INO), the Indian effort to explore the world of neutrino. An overview of the concept and postulation of the neutrino marks the beginning, followed by its features as described in the Standard Model of Particle Physics. The phenomenon of neutrino oscillations is then illustrated. The status of the major experiments that have provided crucial information on the neutrino oscillations are mentioned, and the open problems in this area are listed. The chapter is concluded with a discussion on the motivations of the INO experiment.

1.1   THE ELUSIVE NEUTRINO

The continuous energy spectrum of electrons, observed in nuclear β–decays, was contradictory to the discrete spectrum expected in two-body decays. As repeated attempts became unsuccessful to account for the missing energy [35], the law of conservation of energy and momentum in subatomic processes was in great danger. This even led Niels Bohr speculating the relinquishment of those conservation laws [36]. However, in the year of 1930, W. Pauli, in a desperate attempt to save the conservation laws, postulated that the β–decay may be a three body decay, and an undetected neutral particle could carry the missing fraction of the energy [1, 37]. This particle was later christened as neutrino by E. Fermi, who in 1934 formulated an effective theory of the β–decay [38, 39, 40].

Based on Fermi's theory, H. Bethe and R. Peierls predicted the strength of the neutrino interactions with matter ($\sigma \sim 10^{-44} cm^2$) to be 20 orders of magnitudes weaker than the typical β–decays and hence claimed that neutrino might never be detected [41]. However a long wait of 26 years came to an end, when F. Reines and C.L. Cowan were successful in contradicting that prediction by detecting neutrino through the following inverse β–decay process [2, 3]

$$\bar{\nu}_e + p \rightarrow e^+ + n. \tag{1.1}$$

In this experiment, a huge flux of antineutrinos from a nuclear reactor was used. Two kinds of photon signals were expected —- prompt signals coming from positron annihilation, and delayed photon signals originating from neutron capture on cadmium in the liquid scintillator detector. The detection of both of the signals provided the much sought after evidence of the existence of the antineutrinos.

The next experimental detection was of the muon neutrino (ν_μ) in 1962 [42]. In the first ever high–energy accelerator neutrino experiment at the Brookhaven National Accelerator Laboratory, Leon Lederman, Mel Schwartz, and Jack Steinberger

detected ν_μ, which were produced from the decay of charged pions. It was found that the interaction of these neutrinos with nuclei produced only muons, and no electrons. This showed the distinction of muon neutrinos produced in pion decays and the electron neutrinos produced in β–decays. The discovery of the τ lepton and the missing energy in τ– decays [43] at the Stanford Linear Accelerator Center (SLAC) automatically infers the existence of the third variety of neutrino (ν_τ). The DONuT collaboration succeeded in direct detection of ν_τ in 2000 [44]. The detection of ν_τ completed the three lepton families, consisting of three charged leptons (e, μ, τ) and the associated neutrinos (ν_e , ν_μ , ν_τ).

Neutrinos played an important role in the discovery of parity violation. Cosmic ray experiments indicated that K^+ decay into two different modes with opposite parity (the famous $\tau - \theta$ puzzle), which was later confirmed by precise accelerator experiments. Lee and Yang proposed the violation of parity in weak interactions, in an attempt to solve this puzzle [45]. Subsequently, experiments involving neutrinos confirmed parity violation. The experiment of C.S. Wu, showed parity violation in terms of the forward - backward asymmetry of the electrons emitted from the β decay of polarized ^{60}CO [46]. The V – A model of the weak interaction was then formulated in 1958, by R.P. Feynman and M. Gell-Mann [47], E.C.G. Sudarshan and R.E. Marshak [48], and J.J. Sakurai [49]. In this formulation, only left handed neutrinos and right handed antineutrinos couple in weak interactions.

1.2   SOURCES OF NEUTRINOS

There have been a wide range of sources, both natural and man–made, from which neutrinos are emitted. The generation of neutrinos and its energy range vary significantly depending on the source. The neutrinos, due to their extremely low interaction cross sections, are very efficient messengers of the characteristics of their sources. The important sources of the neutrino are discussed here.

1.2.1   NATURAL SOURCES

- **SOLAR NEUTRINOS:** According to the Standard Solar Model (SSM) [50], the emission of the energy inside the Sun takes place through the exothermal thermonuclear fusion of hydrogen to helium. This process can be written as

$$4p \rightarrow {}^4He + 2e^+ + 2\nu_e + 26.7 \text{ MeV}. \tag{1.2}$$
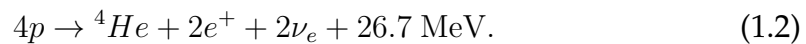
  Most of the energy released in this fusion process is emitted as thermal energy, however, a small fraction (about 2%) of it is transferred to the neutrinos. The energy production mechanism inside the sun is divided into two cycles: (i) Proton – Proton (PP) cycle, and (ii) Carbon – Nitrogen – Oxygen (CNO) cycle. The total solar neutrino flux on earth, the energy being in the range of few MeVs, is about $6 \times 10^{10} \text{ cm}^{-2} \text{ s}^{-1}$.

- **ATMOSPHERIC NEUTRINOS:** The neutrinos in the atmosphere are produced by the cosmic ray interactions with the nuclei in the atmosphere. Primary cosmic rays, mostly protons, interact with the nuclei in the atmosphere to generate secondary cosmic rays, composed of pions and kaons. The pions then decay to muons and muon neutrinos.

$$\pi^- \rightarrow \mu^- + \bar{\nu}_\mu, \qquad \pi^+ \rightarrow \mu^+ + \nu_\mu. \tag{1.3}$$

  The kaons too, at high energies, contribute to the production of muons and muon neutrinos. These muons further decay to electrons, electron neutrinos and muon neutrinos.

$$\mu^- \rightarrow e^- + \bar{\nu}_e + \nu_\mu, \qquad \mu^+ \rightarrow e^+ + \nu_e + \bar{\nu}_\mu. \tag{1.4}$$

  The energy of the neutrinos produced in the above processes vary from a few

hundreds of MeV to 8 GeV. Depending on the position of the detector, and the production point of the neutrinos, the oscillation length may vary from 15 km to $13,000$ km. The wide energy spectrum and baseline of the atmospheric neutrinos offer ample scope to study neutrino oscillations.

- **SUPERNOVA NEUTRINOS:** A huge neutrino flux is generated in supernova explosions, through the electron capture of nuclei and free protons. The hot core of the resultant proto–neutron star, too, produces neutrinos through various processes. The weakly interacting neutrinos escape the extremely dense core. The neutrino burst from a galactic supernova, with a very high flux, is a very efficient source to study the neutrino characteristics. The SN1987A, the only supernova that has been detected through the neutrino burst, has provided landmark results in the neutrino astronomy [51, 52, 53].

- **ULTRA HIGH ENERGY ASTROPHYSICAL NEUTRINOS:** Neutrinos, at nery high energies, are emitted by the astrophysical sources like active galactic nuclei (AGN) and gamma ray bursts (GRB).These neutrinos do not interact with CMB and can reach the Earth from these distant astrophysical sources. Also, the neutrino trajectories do not get bent in the interstellar magnetic fields. Due to the extremely low flux of such neutrinos, very large neutrino telescopes are required to detect them. The IceCube detector has already detected a number of such neutrinos [54, 55, 56].

- **GEO–NEUTRINOS:** The radioactive isotopes like, ^{238}U, ^{232}Th and ^{40}K, embedded in the Earth's crust emit antineutrinos [57, 58, 59]. Radioactive decay of those isotopes is a prominent source of the heat produced at the Earth's core. Precise measurement of the geo-neutrino flux and their spectrum provide crucial insight into the composition of the Earth's core and radiogenic heat production.

- **RELIC NEUTRINOS:** Relic neutrinos are among the most prominent products

of the Big Bang. They are the second most abundant particle in the universe after photons, the number density being 336 neutrinos per cm^3. Initially the neutrinos were in thermal equilibrium via weak interaction with other particles. However, they quickly got decoupled from matter, and thus are expected to provide elaborate probes to the early universe. The kinetic energy of the relic neutrinos has been predicted to be about 10^{-4} eV, which implies a very weak interaction cross section. Thus, the direct detection of the relic neutrinos remains to be an extremely difficult challenge.

1.2.2   ARTIFICIAL SOURCES:

- **REACTOR NEUTRINOS:** Nuclear reactors are the main sources of artificially produced neutrinos. The first experimental detection of neutrinos was done using reactor neutrinos [2, 3]. Power generation in nuclear reactor takes place through the fission of neutron–rich isotopes, such as ^{235}U, ^{238}Th, ^{239}Pu and ^{241}Pu. Electron antineutrinos, in the energy range of $0.1 - 10$ MeV, are produced by the chain of β–decays of the fission products.

- **ACCELERATOR NEUTRINOS:** The decays of charged pions and kaons produced by a proton beam on a target in particle accelerators produce neutrino beams, composed mainly of muon neutrinos. The pions and kaons are focused using a magnetic horn and are made to enter an evacuated decay tunnel where they decay to muons and neutrinos. The muons and the remaining mesons are absorbed in a beam dump at the end of the tunnel, producing a neutrino beam. Focusing positive mesons produces a neutrino beam while negative mesons are focused to produce an antineutrino beam. Alternatively, when a high energy proton beam is stopped in a thick target to generate heavy hadrons, the semi–leptonic decays of the charmed particles are used to produce neutrinos. The charmed heavy hadrons decay promptly emitting equal fluxes of high-energy electron and muon neutrinos.

1.3   NEUTRINOS IN THE STANDARD MODEL

The Glashow–Weinberg–Salam Standard Model (SM) of Particle Physics which contains a description of the elementary particles and the fundamental forces of nature (except gravitational force), was formulated in 1967 by S. Weinberg and A. Salam [60, 61]. This model is based on a SU(2) × U(1) gauge model by S.L. Glashow, which predicted the existence of weak neutral currents and the Z–boson [62]. In the Standard Model the Higgs Mechanism, which allows the original massless gauge bosons in the local gauge group model to acquire mass, is incorporated into Glashow's formulation [63, 64, 65, 66, 67, 68]. The validation of the Standard Model was indicated by the Gargamelle experiment at CERN which discovered neutral-current neutrino interactions in 1973 [69, 70, 71], and was subsequently confirmed at Fermilab [72]. The intrinsic building blocks of the universe are 12 spin–$\frac{1}{2}$ fermions (6 leptons and 6 quarks) and their antiparticles, which interact via 4 spin–1 gauge bosons, termed as force carriers. The fermions and W and Z gauge bosons acquire mass through interactions with the Higgs field, with the associated particle being termed as the Higgs boson, predicted to be a massive and scalar particle. The existence of these particles have been confirmed experimentally, the latest one being the discovery of a Higgs–like boson at the LHC experiments at CERN [73, 74]. The accurate measurement of the invisible decay width of the Z boson by the LEP experiments at CERN constraints the number of active neutrino species, with mass less than half the mass of Z, to three [75, 76, 77, 78].

The neutrinos can interact only through weak interactions via the following two modes, charged current (CC), mediated by W boson, and neutral current (NC), mediated by Z boson. This makes the experimental detection of the neutrinos very very difficult. All neutrinos have left–handed helicity and all antineutrinos have right–handed helicity. Within the Standard Model, the neutrinos are massless and they favour leptonic flavour conservation, i.e., they cannot undergo flavour transforma-

tion. However, experimental observations of neutrino oscillation, the phenomena in which a neutrino changes its flavour, indicates that neutrinos are massive and mixed. The understanding of the mechanism through which neutrinos gain tiny masses, as well as the mixing of the neutrinos are beyond the scope of the Standard Model. Thus, the neutrino is playing a crucial role on the way to the new physics beyond the SM.

1.4   NEUTRINO OSCILLATIONS

The phenomenon of neutrino oscillation was proposed by B. Pontecorvo in the late 1950s [4, 5]. It arises due to the rotation between the flavour eigenstates and the mass eigenstates of neutrinos. The neutrino flavour eigen states ($|\nu_\alpha\rangle$, $\alpha = e, \mu, \tau$), taking part in the weak interaction processes, can be expressed as the linear superpositions of the mass eigen states ($|\nu_j\rangle$, $j = 1, 2, 3$) through a mixing matrix U. This matrix is called the PMNS matrix, named after Pontecorvo, Maki, Nakagawa and Sakata, who formulated the oscillation model for the mixing of different neutrino flavours [79, 80]. The mixing between the flavour and the mass eigenstates can be represented as

$$|\nu_\alpha\rangle = \sum_j U_{\alpha j} |\nu_j\rangle . \tag{1.5}$$

For a basis with three neutrino flavours, the mixing matrix can be expressed in terms of three mixing angles between the mass eigenstates (θ_{12}, θ_{13} and θ_{23}) and a complex phase δ characterizing possible CP violation [81].

As the neutrino propagates in time, the constituent mass eigenstates travel with different velocities and thus get out of phase from each other. As a result, a neutrino with a certain flavor α at $t = 0$, gets transformed into another flavor β with a certain probability. This probability depends on the distance traveled by the neutrino, its energy and the medium it passes through. This phenomenon is feasible only if the neutrinos are massive and they have distinct mass eigenstates.

The neutrino oscillation probability can be obtained by calculating the probability amplitude from the evolution of the flavour eigenstates (using Eq. (1.5)) in time. In the case of the neutrinos traveling through vacuum, the neutrino oscillation probability (for the two flavour mixing) from flavour α to flavour β is given by

$$P(\nu_\alpha \rightarrow \nu_\beta) = \sin^2 2\theta \sin^2 \left(\frac{\Delta m^2 L}{4E} \right), \tag{1.6}$$

where E and L are the energy and distance traveled by the neutrino respectively. In the case of mixing of three flavours, the oscillation probability can be expressed as

$$P(\nu_\alpha \rightarrow \nu_\beta) = \delta_{\alpha\beta} - 4 \sum_{i>j} Re\,(\square) \sin^2 \left(\frac{\Delta m_{ij}^2 L}{4E} \right) + 2 \sum_{i>j} Im\,(\square) \sin \left(\frac{\Delta m_{ij}^2 L}{2E} \right), \tag{1.7}$$

where $\square = U_{\alpha i}^* U_{\beta i} U_{\alpha j} U_{\beta j}^*$, and $\Delta m_{ij}^2 = m_i^2 - m_j^2$.

However, in the presence of matter, the oscillation probability differs significantly from the probabilities in vacuum. The evolution equation of a neutrino, propagating in matter, is affected by effective potentials due to the coherent interactions with the medium through coherent forward elastic weak CC and NC scatterings. The tiny contribution from incoherent scatterings may be neglected. All the three flavours of neutrino interact with the matter they are passing through via NC mode, while the ν_e also interacts via CC mode with the electrons. The NC interactions lead to terms which are irrelevant for the oscillation probabilities, and the matter effects basically arise due to the CC interactions. In the simplistic case of two flavour mixing, the oscillation probability can be expressed with the same form as Eq. (1.6), but with the mass eigenstates and mixing angle replaced by their effective values in matter :

$$P(\nu_\alpha \rightarrow \nu_\beta) = \sin^2 2\theta_m \sin^2 \left(\frac{\Delta m_m^2 L}{4E} \right). \tag{1.8}$$

The Δm_m^2 and θ_m are functions of the effective matter potential A and the mass eigenstates and mixing angle in vacuum. When A = $\Delta m^2 \cos 2\theta$, the mixing is maximal ($\theta_m = \frac{\pi}{4}$) even if the vacuum mixing angle is vanishingly small. This mechanism

is known as the Mikheyev – Smirnov – Wolfenstein (MSW) resonance effect [82, 83]. In the case of three flavour mixing, the oscillation probability expressions in matter are rather complicated, and, exact solutions of the evolution equation of the neutrino can be obtained numerically.

The amplitude of the neutrino oscillations is determined by the three mixing angles, while the frequency is governed by the mass squared differences $\Delta m_{ij}^2 = m_i^2 - m_j^2$. The probability also depends on the Dirac phase (δ), the source-detector distance (L), the neutrino energy (E) and the density of matter through which it propagates. The distance, neutrino energy and matter density are specific to a certain experiment and they determine the sensitivity of the experiment. The oscillation experiments provide information on the the mixing angles and the mass-squared differences. The Δm_{21}^2 and θ_{12} can be estimated from solar neutrino experiments and thus usually referred to as Δm_{sol}^2 and θ_{sol} respectively. Similarly, atmospheric neutrino experiments provide measurements of Δm_{32}^2 and θ_{23}, and hence they are termed as Δm_{atm}^2 and θ_{atm} respectively.

The magnitude and sign of Δm_{21}^2 is established, however in case of Δm_{31}^2 (or, Δm_{32}^2) only the magnitude is known. The unknown sign of Δm_{31}^2 leads to two possible arrangements of the neutrino mass eigenstates as shown in Fig. 1.1. The normal hierarchy (NH) corresponds to the ordering $m_1 < m_2 < m_3$, while the inverted hierarchy (IH) is with the ordering $m_3 < m_1 < m_2$. The hierarchy of the neutrino mass eigenstates can be confirmed once the sign of Δm_{31}^2 is determined. This has been one of the most intriguing challenges in the field of neutrino oscillations at this moment.
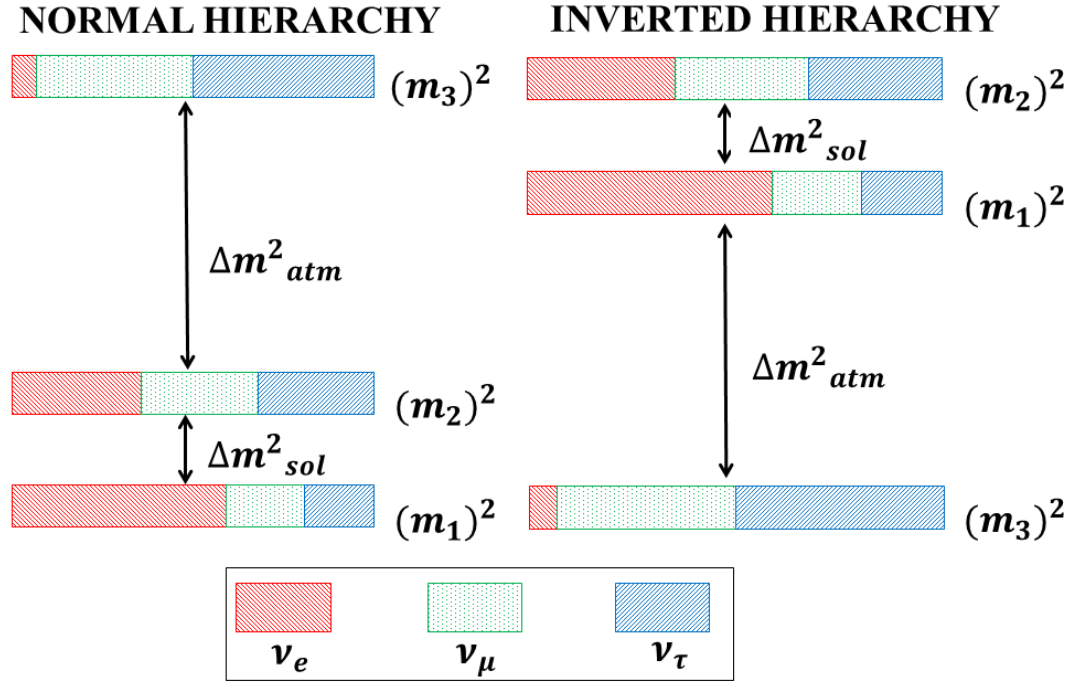
Figure 1.1: The normal (left) and inverted (right) mass hierarchy for neutrinos. The coloured bands signify the respective contributions of the flavour components in the mass eigen states.

1.5 NEUTRINO OSCILLATION EXPERIMENTS

Several neutrino experiments are currently engrossed in the effort of parameterizing the neutrino oscillations. These experiments use neutrinos coming from various sources at various energy ranges. The research and development on a number of future detectors are also ongoing. A few prominent ones are mentioned below.

- Kamioka Liquid Scintillator Anti Neutrino Detector (KamLAND): This is a reactor neutrino experiment [84], with a 1000 ton liquid scintillator detector located in the Kamioka mine, Japan. The antineutrino flux came from 55 reactors, the average source – detector distance being about 180 km.

- Super Kamiokande (SK): This experiment, which involves a large ring imaging Cherenkov detector, is located in the Kamioka mine, with $\sim$ 1 km of rock

coverage [85]. SK has produced splendid results with atmospheric, solar as well as accelerator neutrinos. It has also contributed in the search for supernova neutrinos.

- The Sudbury Neutrino Observatory (SNO): It was a heavy–water Cherenkov detector, located about 2 km below the ground in Sudbury, Canada [86, 87]. It was primarily designed to detect solar neutrinos as well as to study neutrino oscillations. This detector was operational till November, 2006.

- The Main Injector Neutrino Oscillation Search (MINOS): MINOS is a long–baseline neutrino oscillation experiment with two neutrino detectors [88]. The near detector is located at Fermilab, about 1 km away from the source, while the far detector is stationed 735 km away at the Soudan Underground Laboratory. The neutrino beam comes from the Main Injector (NuMI) facility at Fermi National Accelerator Laboratory (FNAL).

- T2K: This the first ever long–baseline neutrino experiment which uses an off–axis beam (by about $2.5°$) [89]. The beam, from the JPARC accelerator facility at Tokai, is sent to the Super-Kamiokande detector at Kamioka at a distance of 295 km.

- Double Chooz: It is a reactor neutrino experiment, the active detector being a liquid scintillator (with 8.3 tons of fiducial mass) at aproximately 1 km away from the two reactor cores [90]. This experiment is being upgraded with a near detector at about 450 m away from the cores.

- Reactor Experiment for Neutrino Oscillations (RENO): It is a short baseline reactor antineutrino experiment in South Korea [91]. It consists of a near detector and a far detector, and uses neutrinos from six powerful reactor cores.

- The Daya Bay reactor experiment: This is a reactor antineutrino experiment as well [92]. This experiment will have 4 near detectors and 4 far detectors. Right

now, it is running with 6 detectors and has already produced exciting results.

- The NuMI Off–Axis ν_e Appearance Experiment (NOνA): NOνA is a neutrino oscillation experiment, consisting of two–detectors, which is optimized for ν_e detection [93]. The NOν_eA experiment will shoot a $3.3°$ off–axis neutrino or antineutrino beam from NuMI at Fermilab to the 15 kt Totally Active Scintillator Detector (TASD) located in Northern Minnesota at a distance of 810 km. The 200 ton near detector at Fermilab is similar to the far detector.

1.6 PRESENT STATUS OF THE NEUTRINO OSCILLATION PARAMETERS

Several experiments have been in action to probe the neutrino oscillation with neutrinos from different sources and in different energy ranges. The present best-fit values of the neutrino oscillation parameters, obtained from global analyses [24, 25] of the existing neutrino oscillation data from those experiments, have been summarized in Table 1.1 .

The solar neutrino oscillation parameters Δm^2_{sol} and θ_{sol} have been measured from the combined analysis of the KamLAND reactor $\bar{\nu}_e$ data and the solar neutrino data [94]. The atmospheric neutrino oscillation parameters (Δm^2_{atm} and θ_{atm}) are constrained by the Super-Kamiokande (SK) atmospheric data [95] , and by the long baseline experiments MINOS as well as T2K ν_μ disappearance data [96, 97, 98]. The recent discovery of non zero (in fact, large) value of θ_{13} has been an exciting finding. After decades of speculations on whether θ_{13} was non-zero, results from the short baseline neutrino experiments Daya Bay [99, 100, 101], Reno [102] and Double Chooz [103, 104] have given the value of θ_{13} to be just below the previous upper bound from the Chooz experiment. In addition to these, the ν_e appearance events in T2K [105, 106, 107] and MINOS [96, 108], have provided a clear indication of non-zero θ_{13} . These experiments continue to improve the precision bounds

on θ_{13}. The Dirac phase has not been measured accurately yet. No information is available on the Majorana Phases so far.

Table 1.1: The neutrino oscillation parameters summary from the global analysis, updated after Neutrino 2014 conference [25].

Parameter	Best fit $\pm$ 1σ	2σ range	3σ range
Δm_{21}^2 [$10^{-5}\ eV^2$]	$7.60^{+0.19}_{-0.18}$	7.26–7.99	7.11–8.18
$|\Delta m_{31}^2|$ [$10^{-3}\ eV^2$] (NH)	$2.48^{+0.05}_{-0.07}$	2.35–2.59	2.30–2.65
$|\Delta m_{31}^2|$ [$10^{-3}\ eV^2$] (IH)	$2.38^{+0.05}_{-0.06}$	2.26–2.48	2.20-2.54
$\sin^2\theta_{12}/10^{-1}$	3.23 ± 0.16	2.92–3.57	2.78–3.75
$\theta_{12}/°$	34.6 ± 1.0	32.7–36.7	31.8–37.8
$\sin^2\theta_{23}/10^{-1}$ (NH)	$5.67^{+0.32}_{-1.24}$ [1]	4.14–6.23	3.93–6.43
$\theta_{23}/°$	$48.9^{+1.8}_{-7.2}$	40.0–52.1	38.8–53.3
$\sin^2\theta_{23}/10^{-1}$ (IH)	$5.73^{+0.25}_{-0.39}$	4.35–6.21	4.03–6.40
$\theta_{23}/°$	$49.2^{+1.5}_{-2.3}$	41.3–52.0	39.4–53.1
$\sin^2\theta_{13}/10^{-2}$ (NH)	2.26 ± 0.12	2.02–2.50	1.90–2.62
$\theta_{13}/°$	$8.6^{+0.3}_{-0.2}$	8.2–9.1	7.9–9.3
$\sin^2\theta_{13}/10^{-2}$ (IH)	2.29 ± 0.12	2.05–2.52	1.93–2.65
$\theta_{13}/°$	8.7 ± 0.2	8.2–9.1	8.0–9.4
δ/π (NH)	$1.41^{+0.55}_{-0.40}$	0.0–2.0	0.0–2.0
$\delta/°$	254^{+99}_{-72}	0–360	0–360
δ/π (IH)	1.48 ± 0.31	0.00–0.09 & 0.86–2.0	0.0–2.0
$\delta/°$	266 ± 56	0–16 & 155–360	0–360

As discussed above, various experiments has produced very exciting results, however certain questions are still not solved. This invokes the requirement of experiments with higher capability as well as sensitivity. The major challenges for the neutrino oscillation experiments are mentioned below.

- **Finer measurement of the oscillation parameters –** The bounds on the oscillation parameters may be made more precise by studying the complete neutrino oscillation pattern.

- **Neutrino Mass Hierarchy –** The determination of the true mass hierarchy is

very crucial to identify the correct mass ordering. The sign of Δm^2_{32} can possibly be determined by probing the matter effects on neutrinos as they propagate through the Earth over long distances [109, 110, 111, 112, 113]. The matter effects experienced by the neutrinos and the antineutrinos are different, and separate study of these effects is important for the mass hierarchy identification [114, 115].

- **CP violation in the leptonic sector –** Possible leptonic CP violation, analogous to the quark sector, may be probed in future long-baseline experiments.

- **Existence of the sterile neutrinos –** Though results from current experiments disfavour the existence of another flavour, further investigations are required to probe the existence of the sterile neutrinos.

- **The neutrino mass generation mechanism –** It is yet another challenge to be explored through a better understanding of the neutrino mixing.

Apart from those in the neutrino oscillation sector, there are also various open questions regarding neutrinos, in general. The absolute mass scale of the neutrino is yet to be obtained. This may be done through sensitive direct mass measurement experiments like β–decay as well as using supernovae and cosmological constraints. The Dirac or Majorana nature of the neutrinos may be established through the unambiguous observation of neutrinoless double beta decay. The detection of the relic neutrinos, at present, seems to be extremely difficult due to their low energy and low interaction cross section. However, new detection techniques with the sensitivity improved by a few orders of magnitude would provide a boost to the search of relic neutrinos.

1.7   THE INDIA-BASED NEUTRINO OBSERVATORY

The first Indian initiative in the field of experimental neutrino physics dates back to the 1960s, when the atmospheric neutrino induced muon events were detected for the first time in the underground detector at the Kolar Gold Field in South India [116, 117]. Several decades later, the India–based Neutrino Observatory (INO) [6], a multi–institutional venture to build a underground neutrino laboratory, revives the Indian effort.

The observatory will be located at West Bodi Hills, in Pottipuram village, 110 km away from the city of Madurai in South India. The facility will be developed within a large underground cavern with 1 km or more rock overburden, which would significantly reduce the background due to the cosmic muons.

The prime experiment at INO would be a huge magnetized Iron Calorimeter (ICAL) detector of approximate mass of 50 kt, which will study the oscillation with atmospheric neutrino. Due to the magnetic field, the ICAL will be able to distinguish between neutrinos and antineutrinos. The main goal of the ICAL experiment would be to determine the neutrino mass hierarchy through studying Earth matter effects separately in the atmospheric muon neutrinos and muon antineutrinos. Apart from that, ICAL would also determine the atmospheric neutrino mixing parameters. The ICAL detector is also expected to provide hints of any non standard interaction, and new physics. The R&D of this experiment in various aspects, like, the detector construction, the simulation of the detector and its sensitivity to fulfill the physics goals, are in progress. In addition to the ICAL, INO will also host other experiments like neutrinoless double beta decay, dark matter experiments, etc.

The ICAL detector, its physics motives as well as the configuration will be detailed in the following chapter.

Chapter 2

THE ICAL DETECTOR

The prime aim of INO is to study the neutrino oscillations with atmospheric neutrinos. Unlike the accelerator and reactor neutrino experiments where the energy (E) and the distance (L) between the neutrino source and the detector are fixed or within a narrow window, the atmospheric neutrinos provide a wide range of E and L. The atmospheric neutrino flux is feeble, and hence the requirement of a detector with a large volume becomes essential to have significant event statistics. In order to fulfill this goal, the INO collaboration plans to build a huge magnetized Iron Calorimeter (ICAL) detector, which would be sensitive to the energy, direction and the electric charge of the final state leptons produced in charged–current (CC) interactions of the neutrinos with the target material [6]. It will use magnetized Iron plates as the target mass and Resistive Plate Chamber (RPC) detectors as the active detector elements [7]. It will be mostly sensitive to the muon neutrinos. The main physics goals of the ICAL are as listed below.

- The reconfirmation of the oscillations in the atmospheric neutrinos through explicit observation of the first oscillation swing in ν_μ disappearance, as a function of L/E.

- The study of matter effects in ν_μ and $\bar{\nu}_\mu$ separately through muon charge identification in order to determine the sign of Δm_{32}^2 and hence to determine the neutrino mass hierarchy.

- Precise determination of the atmospheric neutrino mixing parameters θ_{23} and Δm_{32}^2.

- Determination of the true octant of θ_{23} and its deviation from the maximal value.

Apart from the above, the ICAL will also search for the hint of new physics, such as

- Charge conjugation – parity – time (CPT) violation in the leptonic sector.

- The possible existence of sterile neutrinos.

- The signature of non standard interactions (NSI) in neutrino oscillations.

- Indirect search for dark matter.

The design of the ICAL is motivated by the physics goals mentioned above. In this chapter, the configuration of the ICAL along with a description of its active element RPC are discussed. The various neutrino interactions in ICAL with their specifications and importance to the physics study have also been mentioned.

2.1 THE STRUCTURE OF THE ICAL

The ICAL will mostly look for ν_μ and $\bar{\nu}_\mu$ induced CC interactions using magnetized iron as the target and about $28,800$ RPCs as the active detector elements. It will consist of three identical and adjacent modules, each of dimension $16\,\text{m} \times 16\,\text{m} \times 14.5\,\text{m}$. Each detector module will be made up of 151 horizontal layers of 5.6 cm thick low carbon iron plates interspersed with 4 cm gaps into which the Resistive Plate Chamber (RPC) assemblies. The total mass of the ICAL will be 50 kt.

Table 2.1: The specifications of the ICAL Detector.

No of modules	3
Modular dimension	16 m × 16 m × 14.4 m
Total dimension	48 m × 16 m × 14.4 m
Number of layers	151
Iron plate thickness	5.6 cm
Gap for RPC assembly	4 cm
Magnetic field	1.4 T
RPC unit dimension	195 cm × 184 cm × 2.4 cm
Readout strip width	2.8 cm
Number of RPCs/Road/Layer	8
Number of Roads/Layer/Module	8
Number of RPC units/Layer	192
Total RPC units	$28,800$
Number of electronic channels	3.7×10^6

The schematic of the ICAL detector is shown in Fig 2.1. The blue lines in the three modules as shown in the figure show the placement of the Copper coils through which a current will be passed to generate a non–uniform magnetic field. There will be four coils in each module with 32 turns/coil. The ICAL will be magnetized to a non–uniform field peaking at 1.4 T, to distinguish between the muon and the antimuons produced in the ν_μ and $\bar{\nu}_\mu$ interactions respectively. The total number of readout channels will be about 3.7 million. The important detector specifications have been highlighted in Table 2.1.
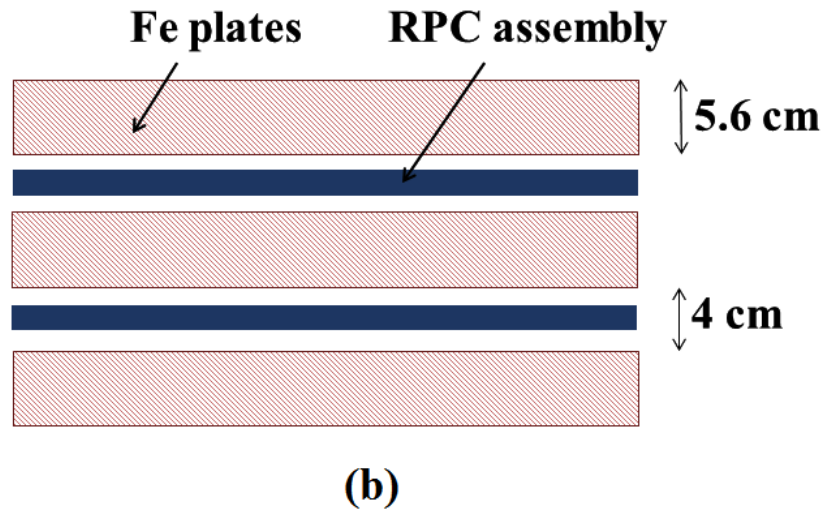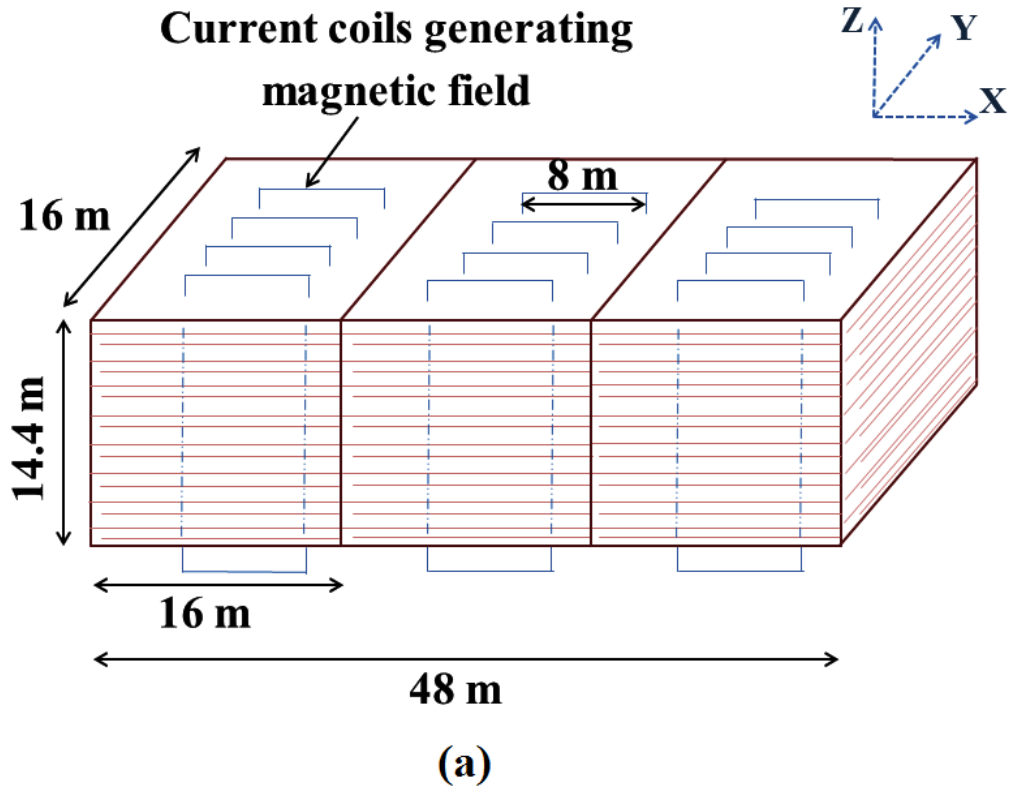
Figure 2.1: (a) The schematic representation of the ICAL detector with dimensions. All the three modules are shown here. The blue lines represent the current coils which magnetize the detector. (b) The placement of the iron plates and the RPC assembly in the ICAL. Each of the three modules of the ICAl consists of 151 such layers.

2.2   THE RPC DETECTORS

The Resistive Plate Chambers (RPCs) are gaseous parallel plate detectors, made of highly resistive electrodes such as glass or Bakelite, to track charged particles. The concept of the RPC was introduced in 1981 by R. Santonico and R. Cardarelli as an alternative to the localized discharge spark counters [118]. The main features of the RPCs are excellent detection efficiency, good spatial as well as position resolutions, wide area coverage and low production cost.
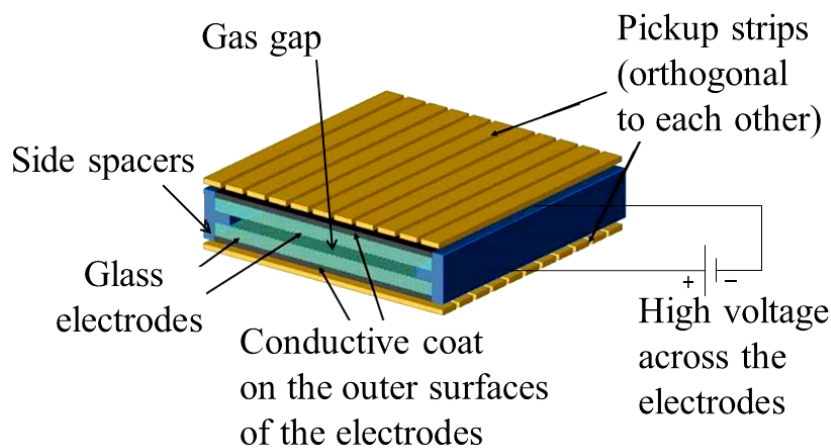
Figure 2.2: The configuration of an RPC detector.

A schematic diagram of the RPC detector configuration is shown in Fig. 2.2. A gas mixture is enclosed by two planar electrodes (glass in our case) with a bulk resistivity of about 10^{12} Ω cm. The gas gap is maintained by cylindrical polycarbonate spacers (bulk resistivity $>10^{13}$ Ω cm). The sides of this chamber are sealed by gluing certain spacers, with inlets and outlets for a continuous gas flow. The two electrodes have conductive graphite coat at their outer surfaces, and they are connected to a high voltage power supply, in order to maintain a uniform and fixed electric field (about 5 kV/mm) across the gas gap.

The formation of the electric signal in the RPC detectors is based on electron multiplication process. When a charged particle passes through the detector, a certain number of primary electrons are produced. These electrons may be grouped into

some clusters. The electrons in any cluster are accelerated by the electric field and they start multiplication. This process is characterized by the following two parameters – the number of ionization per unit length α (first Townsend coefficient), and the number of electrons captured by the gas per unit length β (attachment coefficient). The number of electrons n that reaches the anode can be expressed by the following formula [119]

$$n = n_0 \exp[(\alpha - \beta)x], \tag{2.1}$$

where n_0 is the number of primary electrons in that cluster, and x is the distance between the point at which the cluster was created and the anode.

The gain of the detector is given by

$$M = \frac{n}{n_0}. \tag{2.2}$$

Depending on the value of the gain, the mode of operation of the RPCs are classified as streamer or avalanche. When $M > 10^8$, the primary ionizations will give rise to streamers with high probability. On the other hand, for $M \ll 10^6$, smaller amount of charge is created through simple charge multiplication, and the RPC is said to be operated in the avalanche mode. The mode of operation, as can be seen from Eq. (2.1), is governed by the two parameters α and β which are characteristics of the gas used. A gas mixture of R134a, Isobutane and SF_6 has been used to operate the RPCs in the ICAL R&D program in avalanche mode [7, 120].

When the gas is ionized by the passage of a charged particle, the avalanches of electrons originate a discharge. Due to the high resistivity of the electrodes, the discharge is prevented from spreading through the whole gas volume, and the electric field drops down in a small area around the point where the discharge initiates. The discharged area recharges slowly through the high resistive glass plates and recovery time is about 2 s. The propagation of the electron avalanche induces a current on external electrodes. This is collected by external copper pickup strips of width

2.8 cm. As shown in Fig. 2.2, the pickup strip on the two electrodes are mounted orthogonal to each other, which enables the detection of the location of the passage of the particle in pixels of area 2.8 cm $\times 2.8$ cm. In the rest of this thesis, the measured location of a charged particle in the RPCs will be termed as *hits*. A complete detail of the working principle and design of the RPC detectors can be found in [120].

2.3   NEUTRINO INTERACTIONS IN THE ICAL

The ICAL has been configured to make it primarily sensitive to the ν_μ induced charged–current CC events. Typically a 1 GeV muon can pass through $5 - 12$ RPC layers in the detector depending on the angle of its incidence [9]. The electrons generated in ν_e induced events will hardly cross a few layers, and suitable criteria on the number of layers crossed by the particle can be used to remove such events.
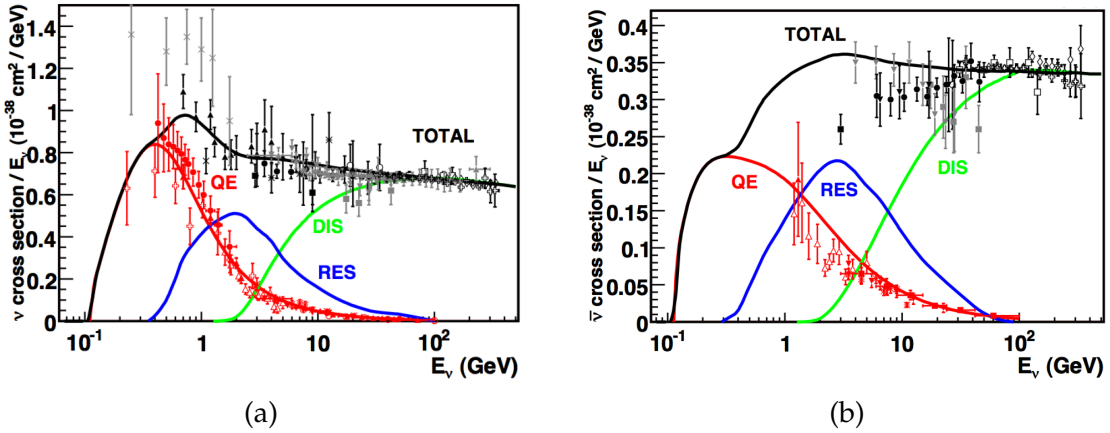
Figure 2.3: The cross sections of (a) CC ν_μ interaction processes, and (b) CC $\bar{\nu}_\mu$ interaction processes. [121]

The atmospheric ν_μ and $\bar{\nu}_\mu$ interact with the iron target through quasi–elastic (QE), resonance scattering (RS) and deep inelastic scattering (DIS) processes as well as a negligible fraction of diffractive and coherent processes. The CC interactions produce muons as well as hadrons. Fig. 2.3 presents the current knowledge on the cross sections of the three prominent CC ν_μ and CC $\bar{\nu}_\mu$ interactions [121]. As can be seen from these figures, in the sub–GeV range the QE processes dominate, and apart from the recoil nucleons they do not have any other hadrons in the final state. As the

energy increases RS and DIS processes start dominating and at a few GeVs DIS becomes the most prominent process. Resonance events typically contain a single pion in the final state, though in a small fraction of events there are multiple pions. DIS events produce multiple hadrons. In the neutral–current (NC) interactions, the final state consists of a neutrino and hadrons. The secondary neutrino would hardly interact with the target, and thus the hadronic parts are the only observables for those events. For the atmospheric neutrinos passing through the Earth's core, maximum matter effects would be experienced by the neutrinos in the energy range $4 - 6$ GeV, which would have prominent fractions of RS and DIS interactions. Thus it is crucial to obtain information on all the final state particles to improve the sensitivity of ICAL in reaching its physics goals.

2.4 ICAL FOR NEUTRINO OSCILLATION STUDY

The ICAL detector would be optimized to be most sensitive to the atmospheric muon neutrinos in the energy range $1 - 10$ GeV. The modular structure of the detector, with the horizontal layers of the iron plates and the RPC detectors allows it to have an wide coverage to the direction of the incoming neutrinos, except the ones producing muons traveling almost horizontally. While the atmospheric neutrino flux provides a wide spectrum in the neutrino energy (E_ν), the detector structure enables it to be sensitive to a broad range of the path length (L) for the neutrinos penetrating through the Earth.

The ICAL would be sensitive to both the energy and direction of the muons produced in the CC interactions of the atmospheric muon neutrinos and the antineutrinos with the iron absorber plates. The upward–going and downward–going muon events can also be identified using the fast response time of the RPCs, which is of the order of nanoseconds. This distinction would allow the separation of the neutrinos with short path lengths from those with longer ones. This would be very useful to study neutrino oscillations, as the oscillation probability strongly depends on the

path length L.

In addition, ICAL, being a magnetized detector, would be able to differentiate between muons and antimuons, which makes it capable of separating events induced by muon neutrinos and muon antineutrinos. Since the neutrinos and the antineutrinos experience different matter effects while propagating through the Earth, the ability to discriminate between neutrinos and antineutrinos makes the detector sensitive to the neutrino mass hierarchy, which is the main goal of the ICAL experiment. The presence of the magnetic field also improves the momentum resolution of the muons by measuring the extent of bending of the muon track in the local magnetic field.

As have been mentioned above, the structure and good tracking ability of ICAL makes it suitable to explore the neutrino oscillations in the atmospheric muon neutrino interactions. The ICAL is also sensitive to the energy deposited by the hadrons in the multi–GeV range. It is very crucial to estimate the capability of ICAL in reconstructing various particles, which in turn would provide the expected sensitivity of the detector in reaching its physics goals. Hence a simulation of the ICAL detector has been performed using the GEANT4 simulation package in the CERN–library [8]. The simulation framework and the response of the detector to various particles like muons and hadrons, and the physics reach of ICAL using those information has been described in the following chapters.

Chapter 3

THE ICAL DETECTOR SIMULATION AND MUON RESPONSE

The ICAL would detect the interactions due to the atmospheric ν_μs, arising from $\nu_\mu \to \nu_\mu$ and $\nu_e \to \nu_\mu$ oscillation channels. The accurate determination of the energy and direction of the final state particles, i.e., the muons and the hadrons, in those interaction events are crucial to achieve the physics goals of the ICAL. The ν_μ and $\bar{\nu}_\mu$ would experience separate matter effects for either of the possible mass ordering, while propagating through the Earth. Thus by observing the individual event rates for ν_μ and $\bar{\nu}_\mu$ through the distinction of the final state μ^+ and μ^- in the CC events, the mass ordering may be determined. Additional informations on the final state hadrons would provide enhancement in the physics sensitivity of the detector. Thus, the ICAL detector should be correctly calibrated to reconstruct the energy and direction of the muon and hadrons, as well as the identification of the charge of the muons.

A detector simulation framework to calibrate the ICAL response to the muon and hadrons has been developed using the GEANT4 simulation package. This frame-

---

The sections on the muon response of ICAL are based on JINST **9**, P07001 (2014) [9], and have been included for the sake of completeness.

work has been described in the following section. The muon reconstruction algorithm is then described in section. 3.2 along with the efficiencies of muon reconstruction and charge identification, and the energy and direction resolutions.

3.1 THE DETECTOR SIMULATION

The ICAL detector consisting of three modules has been simulated using GEANT4, a detector description and simulation package provided by the CERN–library [8]. The detector details, as described in Chapter 2, have been incorporated in the simulated detector geometry. The input parameters for the simulation, like, the conducting coating, gas mixture, efficiency, etc., have been taken from the results of a 12–layered stack of glass RPC detectors (without the Iron absorber plates) that is being run under stable conditions at TIFR for several years [7, 120] . The readout strip width is taken to be 1.96 cm. The actual strip width is planned to be 2.8 cm. The dead space due to the insertion of the copper coils for magnetization, alterations due to the support structures etc., are also taken into account.

A detailed simulation of the magnetic field for the proposed coil structure has been performed and has been incorporated in the simulation code. Fig. 3.1 shows the magnetic field map in the central plane of the central module ($z = 0$) which has been obtained using the MAGNET6.26 software [122]. The arrows denote the direction of the magnetic field, while the length of the arrows indicate the field magnitude. The magnetic field has been taken to be zero in the air gap between the iron plates and in the steel support structures (non–magnetic).

The detector simulation framework is then used to study the propagation of the final state particles in a neutrino event generated using the NUANCE generator[13]. The output of the GEANT4 code is stored as ROOT–tree [16] and analyzed. In Fig. 3.2 the illustration of the simulation framework has been shown.

When a charged particle propagates through the ICAL detector, hits in the X and Y strips of the RPC layers are recorded. The layer number provides the z–
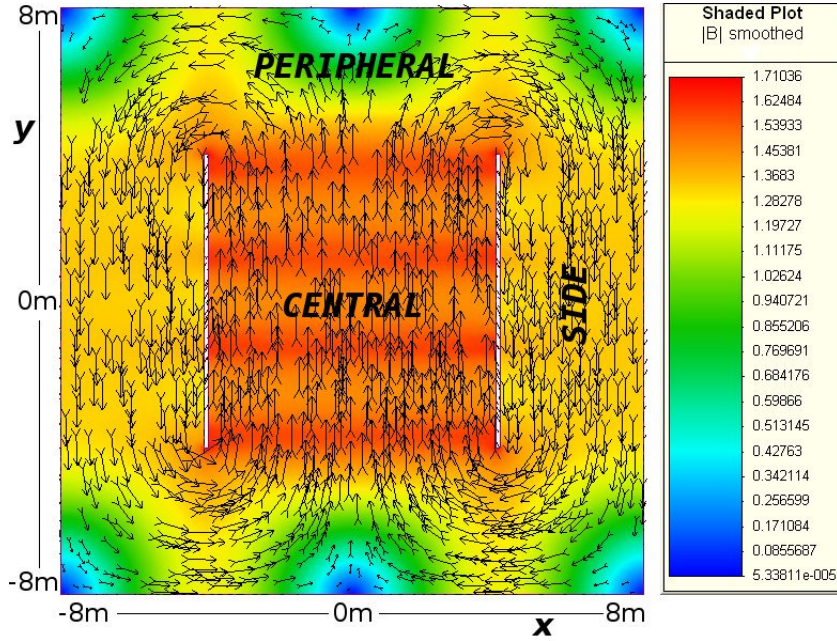
Figure 3.1: The magnetic field map in the central plane of the central module of the ICAL, where z is zero, generated using MAGNET6.26 package [122]. The length and direction of the arrow in the plot represent the magnitude and direction of the field respectively. The field magnitude is also indicated by the colour coding. [9]

coordinate. Thus the full information on the position coordinates is available, within a precision of 1.96 cm $\times 1.96$ cm in the xy – plane and 2 mm in the z direction. The secondary particles produced by the passage of the primary particle in the detector can also be tracked. In the case of a minimum ionizing particle like muon, only a few secondary particles would be generated. However, in the case of hadrons, a number of secondary particles would be produced via strong interaction. The digitization of a hit is done by determining its $(x,\ y,\ z)$ coordinates and time (t) with respect to the trigger, and they are stored as the simulation code output for further analysis.

A muon usually leaves a track with an average layer multiplicity of 1.4 [120], and so the hits from both X and Y strips can easily be combined to obtain the number of hits and their position coordinates $(x,\ y)$ in a given layer. In Sec. 3.2, the algorithm, which has been developed to reconstruct the muon momentum, is described. This code includes steps for finding the track and fitting it to a Kalman–filter [123] based algorithm to distinguish between μ^- and μ^+ and to calculate their momentum.
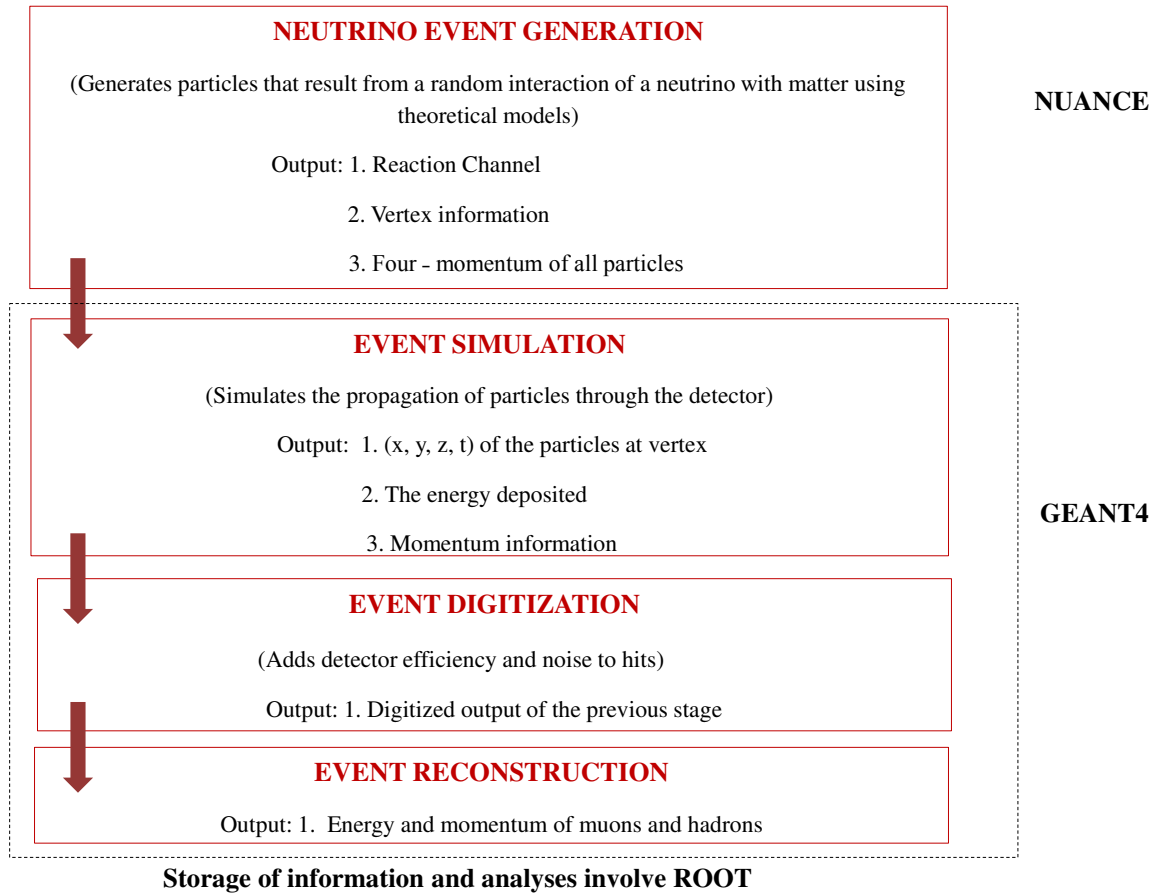
Figure 3.2: The framework for ICAL detector simulation.

However in the case of hadrons, there will be multiple hits per layer and a shower like feature will be formed. In the next chapter, the study of the hadron hit pattern, its use to obtain the hadron energy resolution of ICAL and to calibration the hadron shower energy would be discussed in detail. A typical neutrino interaction event (simulated) in the ICAL, with the muon track and the hadron shower, has been shown in Fig 3.3. It is a DIS interaction event, with significant fraction of the incident neutrino energy going the hadrons.
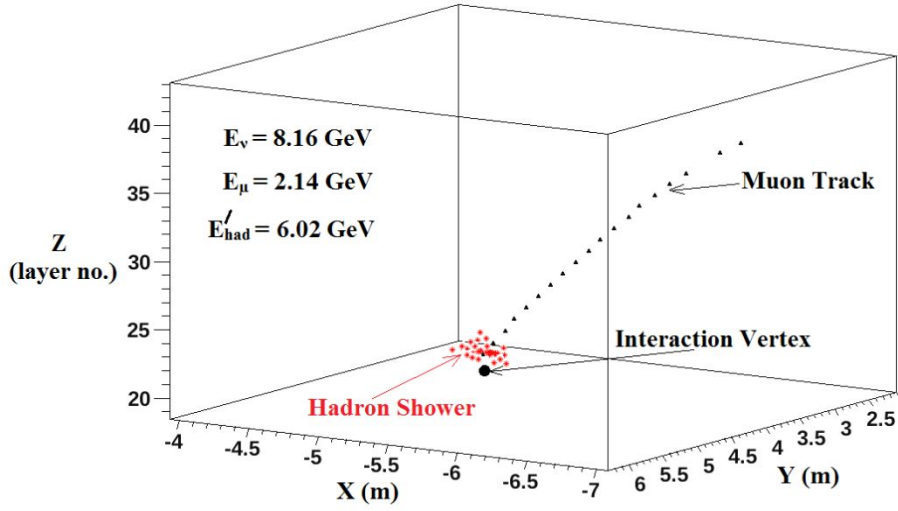
Figure 3.3: A typical DIS interaction event in the simulated ICAl.The black filled triangles represent the muon track, while the red stars show the shower created by the hadrons. [10]

3.2   THE MUON RECONSTRUCTION IN ICAL

The muon momentum reconstruction in ICAL has been done through an algorithm, which involves steps to finding the track and fitting it with a Kalman–filter based technique to distinguish between μ^- and μ^+ and to calculate their momentum. The various steps of this reconstruction algorithm has been described in the following.

3.2.1   TRACK FINDING

The hits in the RPC layers are assigned the (x, y) coordinates from their respective pick–up strip information. The z–coordinate is provided by the certain layer information. The time count for each hit is also recorded with respect to the trigger for that event. The possible pairs of adjacent hits in a plane are combined to form a *cluster*. The track finder algorithm then looks for the clusters in successive RPC layers. A set of clusters formed in adjacent layers are then combined through a curve fitting algorithm in order to obtain a *tracklet*. Tracklets close to each other are then

picked to form a track, and the longest possible track in an event is obtained through the iteration of this process [124]. The time information coming from all the x and y strip hits in a layer are averaged, and this value determines the direction of the track (upward or downward). This algorithm also distinguishes between muon–like and shower–like tracks. A criteria of at least 5 hits in a muon–like track is imposed to minimize the misidentification of a hadron shower or noise hits as a muon track. In the muon–like tracks satisfying this criteria, the clusters in each layer are averaged to one hit per layer, and the corresponding coordinate and timing information are passed to the track fitting algorithm.

3.2.2 TRACK FITTING

The tracks picked by the track finder are then fitted with a Kalman–filter based algorithm. This algorithm takes care of the energy loss of the propagating particle and its bent path in the local magnetic field. Each of the tracks are assigned with an initial state vector

$$X_0 = (x, y, dx/dy, dy/dz, q/p), \tag{3.1}$$

where $(x,\ y,\ z)$ are the position coordinates of the earliest hit as determined by the track fitter. The ratio q/p is the charge-weighted inverse of the momentum, which is initialized as zero. The first two layers are used to determine the direction of the track and the initial state vector is extrapolated and updated using the Kalman–filter technique. The estimated state vector after l layers is given by

$$X_l = F_{l-1}X_l + U_{l-1}, \tag{3.2}$$

where F is the propagation matrix that transports the state vector from a plane to the next. The propagation matrix contains information on the local magnetic field, and is calculated for all adjacent pairs of layers in ICAL. A 5×5 covariance matrix C stores the expected error in the state vector. The process noise U stores the informa-

tion on the multiple scattering and energy loss by the propagating particle [125, 81]. The track fitting is done to obtain the accurate estimation of the state vector at each plane and eventually to obtain a best fit to the track.

The interaction vertex is reconstructed by extrapolating back the track at its beginning by half a layer of iron, since the neutrino interactions are most likely to happen in the iron layers. The best fit values of the momentum at the vertex are assigned to be the incident momentum of the muon. The parameters q/p in the state vector provides the magnitude of the muon momentum as well as the muon charge. The direction θ and ϕ of the muon are obtained from the parameters dx/dz and dy/dz. The fits for which the goodness–of–fit is better than χ^2/ndf <10 are used in the study. The ICAL response to muon, obtained using this algorithm, for fixed energy muons generated using GEANT4 Monte Carlo are described in Sec. 3.3.

3.3   THE MUON RESPONSE OF ICAL

The ICAL capability of reconstructing muon momentum has been studied using muons generated in the GEANT4 Monte Carlo at various energies and zenith angle. A volume of 8 m ×8 m ×10 m in the central region of the central module of the detector has been used to randomly generate the interaction vertex, and 10000 muons at each energy and zenith angle combination are propagated. In all such sets, the azimuthal angle is smeared uniformly between 0 to 2π. The track reconstruction efficiency, charge identification efficiency, muon momentum resolution and zenith angle resolution are studied and quantified. The important results of this analysis are mentioned below.

3.3.1   MUON MOMENTUM RESOLUTION

The distribution of the reconstructed muon momentum at low energies ($P_{in} < 2\,\text{GeV}$) show an asymmetric tail as shown in Fig. 3.4a. These distributions are fitted to a convolution of Landau and Gaussian probability distribution functions (PDF). The his-

tograms at higher energies show no asymmetric tails (as shown in Fig. 3.4b) and are fitted to the Gaussian PDF. In order to keep a consistency in calculating the widths of the distributions, the width for the Landau–Gauss convoluted fit is defined as

$$\sigma \equiv \text{FWHM}/2.35, \qquad (3.3)$$

where FWHM stands for the Full Width at Half Maximum.

The muon momentum resolution R (with its error δR) is defined as

$$R \equiv \sigma/P_{in}, \quad \delta R/R = \delta\sigma/\sigma. \qquad (3.4)$$

(a)　　　　　　　　　　　　　(b)
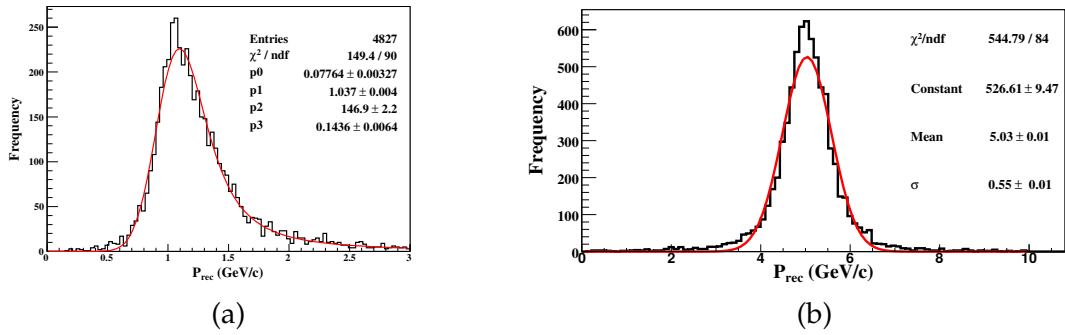
Figure 3.4: (a) The distribution of the reconstructed muon momentum at 1GeV. This distribution shows a asymmetric tail and has been fitted to Landau convoluted with a Gaussian. (b) The distribution of the reconstructed muon momentum at 5 GeV. This distribution is asymmetric and has been fitted to a Gaussian. [9]

The muon momentum resolution as a function of the input momentum for different $\cos\theta$ is shown in Fig. 3.5. It can be seen from the figure that the resolution improves initially with increase in momentum (upto about 6 GeV). At such small momenta, the number of RPC layers crossed by the muon and the number of hits increase with increasing energy, and also, the magnetic field causes significant bending. These enhance the accuracy of the momentum reconstruction. However, with further increase in the incident momentum, the particle starts to exit the detector so that only a partial track is confined in the detector. The radius of curvature of bending increases too, and the track becomes relatively straighter. These factors results

in a poorer fit to the track, and hence the resolution worsens.
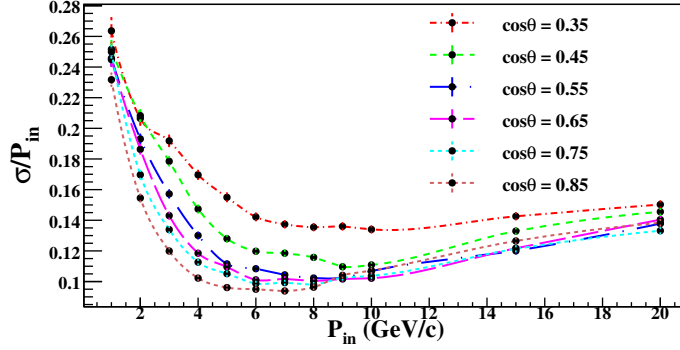
Figure 3.5: The muon momentum resolution as a function of the input momentum for different $\cos\theta$. [9]

3.3.2   MUON ZENITH ANGLE RESOLUTION

The zenith angle resolution is defined as the width of the reconstructed θ distributions, fitted to the Gaussian pdf. A sample at $P_{in} = 5\,\text{GeV/c}$ and $\cos\theta = 0.65$ is shown in Fig. 3.7. The narrow distributions indicate a good angular resolution.
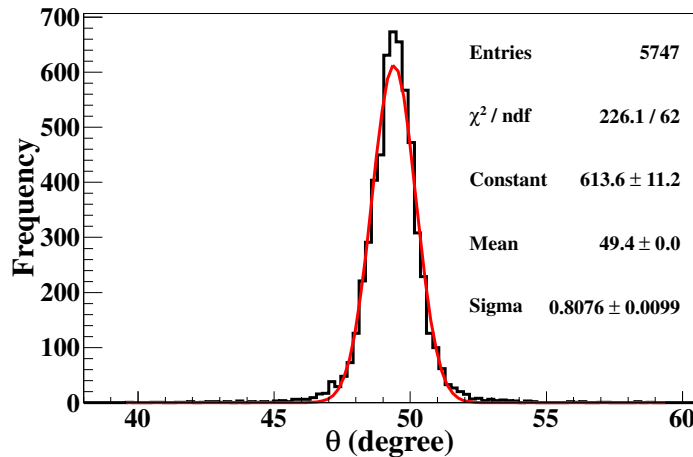
Figure 3.6: The distribution of the reconstructed muon direction at $P_{in} = 5$ GeV/c and $\cos\theta = 0.65$. The narrow distributions indicate a good angular resolution of the muons. The distribution is fitted to a Gaussian. [9]

In Fig. 3.7 the θ resolution as a function of the incident momentum at different zenith angles is shown. For all input angles and $P_{in} >4$ GeV/c, the resolution is better than a degree. At 10 GeV/c and beyond, the resolution curves approximately

coincide.
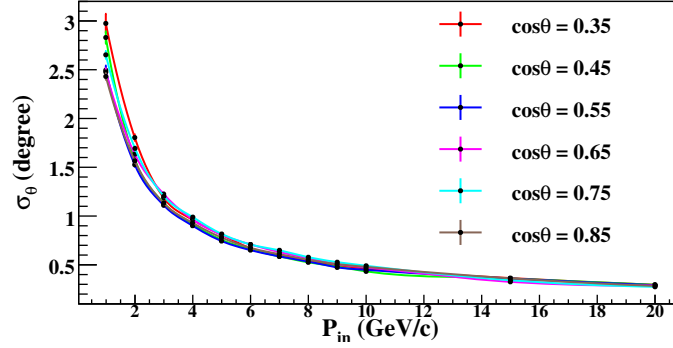
Figure 3.7: The θ resolution as a function of the incident momentum at different zenith angles. [9]

3.3.3 RECONSTRUCTION EFFICIENCY

The reconstruction efficiency (ϵ_{rec}) is defined as

$$\epsilon_{rec} = \frac{N_{rec}}{N_{total}}, \text{with error } \delta\epsilon_{rec} = \sqrt{\epsilon_{rec}(1-\epsilon_{rec})/N_{total}}, \tag{3.5}$$

where N_{rec} is the number of the reconstructed events irrespective of the charge, and N_{total} is the total events.
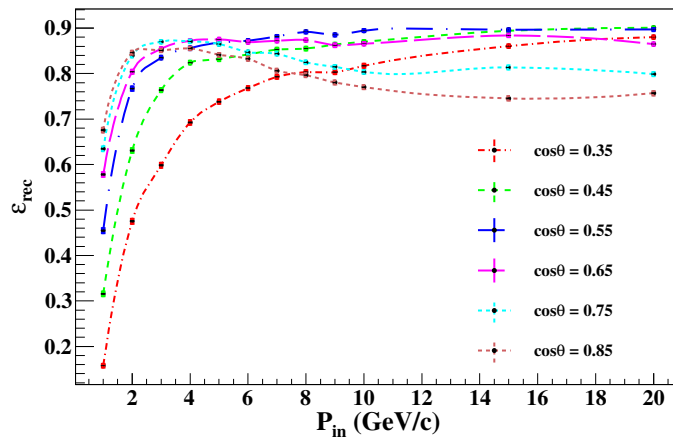
Figure 3.8: The muon momentum reconstruction efficiency, as a function of the input momentum and at certain $\cos\theta$ bins. [9]

The muon momentum reconstruction efficiency, as a function of the input momentum and at certain $\cos\theta$ bins, is shown in Fig. 3.8. The momentum resolution

efficiency is marginally smaller than the track reconstruction efficiency, particularly at smaller angles. This efficiency depends on the factors like the incident energy and direction, the magnetic field strength.

As can be seen from Fig. 3.8, for momentum values $< 4\,\text{GeV/c}$, the reconstruction efficiency increases with increasing incident momentum at all incident angles. This is due to the increase in the number of hits with increase in incident momentum, as the particle traverses more number of layers. This effect is the most for the particles propagating in a near vertical direction. As the zenith angle increases, the number of layers crossed by the particle becomes smaller. However, at higher energies, the particle at any incident angle crosses sufficient number of layers, and the reconstruction efficiency becomes almost constant. A drop is observed in the reconstruction efficiency of the vertical muons, which is due to the track being partially confined in the detector and the requirement of a single reconstructed track to pick the events to be analyzed.

3.3.4 RELATIVE CHARGE IDENTIFICATION EFFICIENCY

The charge identification of muons, provided by the direction of curvature of a track in magnetic field, is very important to determine the neutrino mass ordering, as it separates the neutrino and antineutrino interaction events. The relative charge identification efficiency (ϵ) is defined as

$$\epsilon_{cid} = \frac{N_{cid}}{N_{rec}}, \text{with error } \delta\epsilon_{cid} = \sqrt{\epsilon_{cid}(1-\epsilon_{cid})/N_{rec}}, \tag{3.6}$$

where N_{cid} is the number of events with correct charge identification and N_{rec} is the total number of reconstructed events.

The relative charge identification efficiency is shown in Fig. 3.9 as a function of the incident muon momentum at different $\cos\theta$. The muon undergoes multiple scattering while propagating through the detector, and this may lead to an incorrectly reconstructed direction of bending at smaller incident momentum, since the number
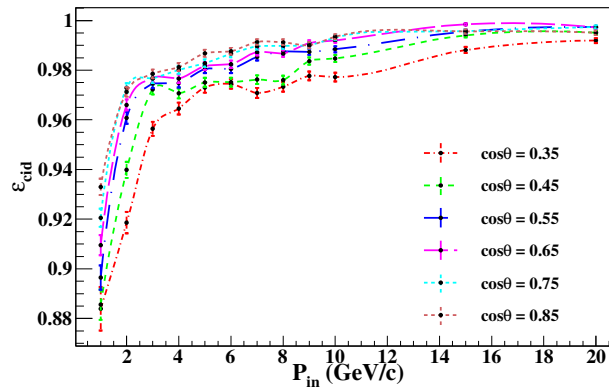
Figure 3.9: The muon charge identification efficiency, as a function of the input momentum and at certain $\cos\theta$ bins. [9]

of layers crossed is small. This effect can be seen in Fig. 3.9 as the efficiency at lower energies is relatively poorer. With increase in energy, the track length increases and the reconstruction of the direction of the curvature becomes more accurate.

3.4 REMARKS

The reconstructed parameters of muons in ICAL have then been used to estimate the potential of the ICAL detector in fulfilling its physics goals. However, in the CC DIS and RS events, apart from the muon the hadrons too take away a significant fraction of the neutrino energy. In NC events, only hadrons are detectable. In the next chapter, the study of the hadron hit distributions and the calibration of the hadron energy has been discussed in detail. Thus, the ICAL physics sensitivity would increase with the addition of the information on hadrons. For this, the capability of ICAL in reconstruction hadron energy is crucial. The observable in the case of hadrons in an event is a shower like feature formed by the hits, close to the interaction vertex and spread in a few layers with multiple hits per each layer. In the next chapter, the study of the hadron shower hit distributions, and the method of calibration of the hadron energy will be discussed in detail.

Chapter 4

THE HADRON ENERGY RESOLUTION OF ICAL

In the case of CC–DIS and CC–RS interaction events, a significant fraction of the incident neutrino energy is carried by the hadrons. The hadrons produce a shower of hits via strong interactions, where the hits are confined to a few layers with a much higher strip multiplicity as compared to the muons. Thus it is not possible to obtain the energy of the hadrons from their tracks. However, the hadron energy can be estimated using the shower hit information. In the case of CC events, the initial neutrino energy can be reconstructed using the reconstructed energies of the final state muon and hadrons. On the other hand, in the case of NC interaction events the hadrons are the only observables in the detector, and the estimation of their energy would be very important to study such interactions. In this chapter, the study of the hadron hit pattern in ICAL, its use to obtain the hadron energy resolution of ICAL and the calibration of the shower hits for the hadron energy are presented.

This chapter is based on JINST **8**, P11003 (2013) [10].

4.1   THE HADRON HIT PATTERN IN ICAL

Unlike the long passage of the muons, the hadrons pass through a few layers near the interaction vertex, leaving multiple hits per layer to form a shower [126, 127, 128, 129]. Due to this multiplicity, combining the X and Y strip hits would leads to some false count of hits (ghost hits). To avoid the ghost hit counts, the energy calibration may be done with counts from either X or Y strips. In the simulation code output, variables x–hits and y–hits store the number of hits in the X and Y strips of the RPC, respectively. The maximum of x–hits or y–hits in an event is stored as the variable "orig–hits". In Fig. 4.1 the comparisons of these three types of hit variables for $\pi^{\pm}$ of energy 3 GeV are shown. As is clear from Fig. 4.1 any of the variables x–hits, y–hits or orig-hits can be used. In the analysis that follows, the variable orig-hits has been chosen as the unbiased parameter. It may also be observed from Fig. 4.1 that the detector response to the positively and negatively charged pions is identical. Thus they have not been differentiated to study the detector response. In this study the additional hits due to the edge effects and noise have been neglected, and these will be incorporated once the data from the prototype detector becomes available in future.
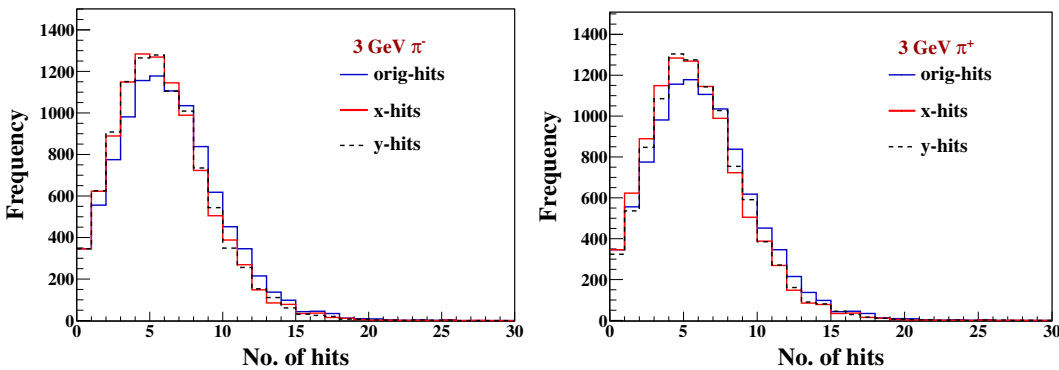
Figure 4.1: The comparison of the simulation outputs variables x–hits, y–hits and orig–hits. The left panel shows the comparison for π^- at 3 GeV, while the right panel shows the corresponding comparison for π^+ events. The events are propagated randomly through a 200 cm $\times 200$ cm $\times 200$ cm volume in the central part of the detector. Also, from the two panels it is clear that the response of ICAl to π^- and π^+ are identical. [10]

In Fig. 4.2 the hit distributions in the detector for pions, kaons, and protons at a few representative energies in the range of $1 - 15$ GeV are shown. It is observed that for all these hadrons the hit patterns are similar. Though the peak position and spread vary depending on the particle, this variation is insufficient to make the detector capable of distinguishing among the hadrons which have generated the shower. The large variation in the number of hits for the same incident particle energy is partly due to angle smearing and more dominantly due to the strong interaction processes with which hadrons interact with the detector elements. The exception is π^0, which immediately decays into an $e^+ e^-$ pair; the fewer number of hits and the narrower hit distribution in this case reflects the nature of electromagnetic interactions of this pair with the iron target.
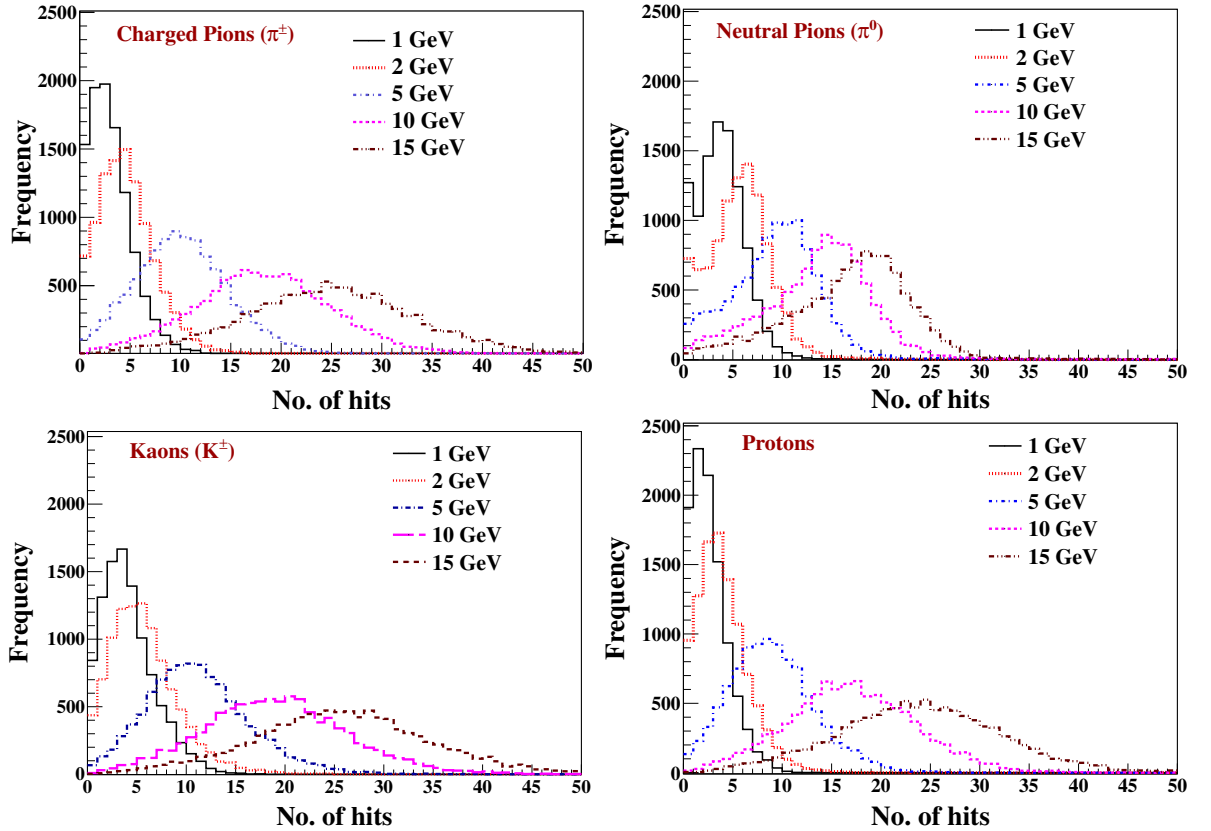
Figure 4.2: The hit distributions at various energies (angle-averaged) for $\pi^\pm$, π^0, $K^\pm$ and protons propagated from vertices smeared over a 200 cm $\times$ 200 cm $\times$ 200 cm volume in the central part of the detector. [10]

We see that, the hit distributions are asymmetric with a long tail, and the Gaussian distribution would not provide a good approximation particularly at low energies. Thus a suitable fit function that correctly reproduces the mean and variance at all energies is required. In the following section, the trials and results of finding a suitable PDF has been described.

4.2   A SUITABLE PROBABILITY DISTRIBUTION FUNCTION

From Fig. 4.2 it is clear that the hit distribution approaches the Gaussian pdf would approximate the hit distributions only at energies greater than about 5 GeV. Since most of the atmospheric neutrino events to be detected in ICAL would be concentrated in the energy range $\leq$ 10 GeV, it becomes important to find a suitable PDF for the hit distribution. The PDF should approximate the Gaussian at high energies.

Here the hit distributions are analyzed using three fitting functions. As we have seen, the hit distribution is asymmetric, particularly at lower energies. The following functional forms are compared: (i) Gaussian, (ii) Landau convoluted with a Gaussian, and (iii) Vavilov. The energy loss of a particle passing through moderately thick absorbers is commonly modeled using the above three distributions depending on the energy of interest.

In Fig. 4.3 the sample hit distributions are shown for 10000 pions $(\pi^{\pm})$ propagated through the detector from randomized vertex points in a 200 cm $\times 200$ cm $\times 200$ cm volume in the central region, at sample energies of 3 GeV and 8 GeV, fitted to the three functional forms. A comparison of the fit parameters is shown in Table 4.1, where we also indicate the P–values obtained from the Kolmogorov–Smirnov (KS) test. It is clear that the best fit is obtained with the Vavilov PDF [14, 15]. A sweep of all other energies shows that the Vavilov PDF consistently gives a better fit than the other distributions. This PDF will be used in the analysis presented in this chapter.
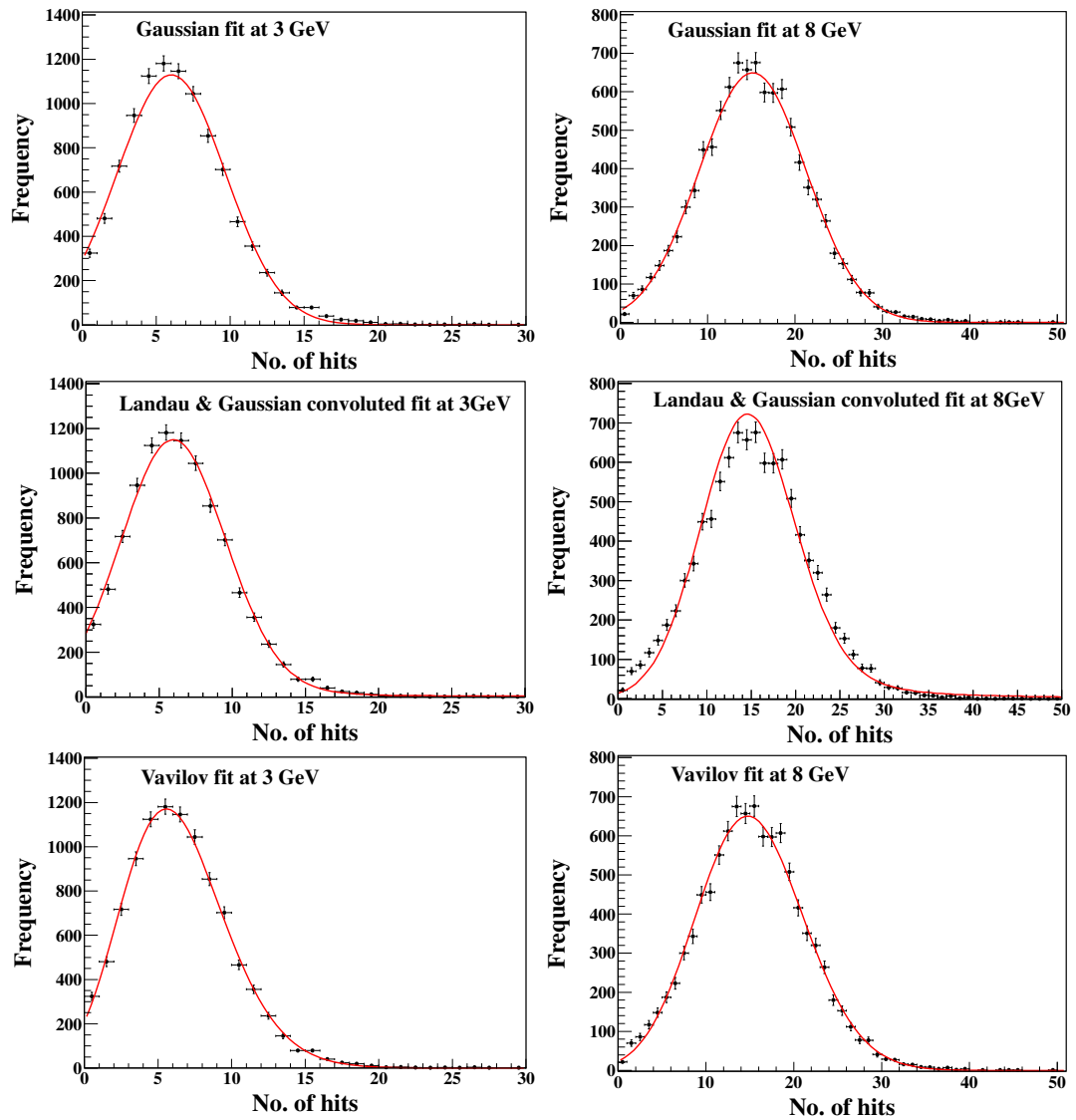
Figure 4.3: The hit distributions at sample energies 3 GeV and 8 GeV, shown with statistical errors and fitted with (top) Gaussian, (middle) Landau convoluted with Gaussian, and (bottom) Vavilov distributions. The resulting fit parameters and quality of fits are shown in Table .

Table 4.1: Comparison of the three different pdf fits for 3 GeV and 8 GeV pions. The χ^2 values as well as the Kolmogorov–Smirnov (KS) statistics quantify the substantial differences in the quality of fits with different pdfs. Note that the mean and sigma are less sensitive to the choice of PDF. For comparison the mean and rms obtained directly from the hit distribution are also shown in the third column.

E_π	Parameters	Histogram	Gaussian	Landau	Vavilov
3 GeV	χ^2/ndf		4.6	4.2	1.7
	P (KS test)		8.1×10^{-6}	7.6×10^{-6}	0.95
	$\bar{n}$	6.019	6.022 ± 0.043	6.021 ± 0.043	6.018 ± 0.044
	σ	3.484	3.671 ± 0.042	3.601 ± 0.048	3.431 ± 0.052
8 GeV	χ^2/ndf		2.204	2.01	1.607
	P (KS test)		2.6×10^{-4}	1.2×10^{-4}	0.92
	$\bar{n}$	14.813	15.151 ± 0.061	15.062 ± 0.063	14.781 ± 0.063
	σ	6.114	6.138 ± 0.051	6.129 ± 0.053	6.124 ± 0.068

4.2.1   THE VAVILOV PROBABILITY DISTRIBUTION FUNCTION

As has been observed from Fig. 4.3, and Table 4.1, the Vavilov probability distribution function is indeed be a suitable one to represent the hit distributions.

The Vavilov PDF in the standard form is defined by [15]

$$P(x; \kappa, \beta^2) = \frac{1}{2\pi i} \int_{c-i\infty}^{c+i\infty} \phi(s)e^{xs}ds \, , \tag{4.1}$$

where

$$\phi(s) = e^C e^{\psi(s)}, \quad C = \kappa(1 + \beta^2\gamma) \, , \tag{4.2}$$

and

$$\psi(s) = s \ln \kappa + (s + \beta^2\kappa) \cdot \left[\int_0^1 \frac{1 - e^{-st/\kappa}}{t} dt \; - \; \gamma \right] - \kappa \, e^{-s/\kappa} \, , \tag{4.3}$$

where $\gamma = 0.577\ldots$ is the Euler's constant. The parameters *mean* and *variance* (σ^2) of the distribution in Eq. (4.1) are given by

$$mean = \gamma - 1 - \ln \kappa - \beta^2; \quad \sigma^2 = \frac{2 - \beta^2}{2\kappa}. \tag{4.4}$$

For $\kappa \leq 0.05$ the Vavilov distribution may be approximated by the Landau distribution, while for $\kappa \geq 10$ it may be approximated by the Gaussian approximation, with the corresponding mean and variance.

To fit the hit distributions the Vavilov distribution function $P(x; \kappa, \beta^2)$, which is built into the ROOT package, has been modified to the form

$$(P_4/P_3) \; P((x - P_2)/P_3; \; P_0, \; P_1). \tag{4.5}$$

This has been done to account for the x–scaling (P_3), normalization (P_4) and the shift of the peak to a non-zero value (P_2). Clearly $P_0 = \kappa$ and $P_1 = \beta^2$. The modified mean and variance are then

$$Mean_{\text{Vavilov}} = (\gamma \; - \; 1 \; - \; \ln P_0 - P_1) \, P_3 + P_2 \, , \quad \sigma^2_{\text{Vavilov}} = \frac{(2 - P_1)}{2P_0} P_3^2 \, . \tag{4.6}$$

4.3   THE PION ENERGY RESOLUTION IN ICAL

Charged pions constitute the most prominent part of the hadrons produced in neutrino interactions. In this section the energy resolution of the ICAL for charged pions ($\pi^\pm$) is discussed. Pions at fixed energies, generated using the GEANT4 Monte Carlo, are propagated through a volume of 200 cm $\times 200$ cm $\times 200$ cm in the central region of the ICAL. In addition, since there is very little impact of the magnetic field on the showers produced by hadrons, the hadron direction is uniformly smeared over zenith angle $0 \leq \theta \leq \pi$ and azimuth of $0 \leq \phi \leq 2\pi$. The angles are denoted with respect to a reference frame shown in Fig. 2.1 where the origin is taken to be the center of the detector, the z–axis points vertically up, while the plates are horizontal in the xy plane. This serves to smear out any angle–dependent bias in the energy resolution of the detector by virtue of its geometry which makes it the least (most) sensitive to particles propagating in the horizontal (vertical) direction. The modified Vavilov PDF as given in Eq. (4.5) has been used to fit the hit distributions.
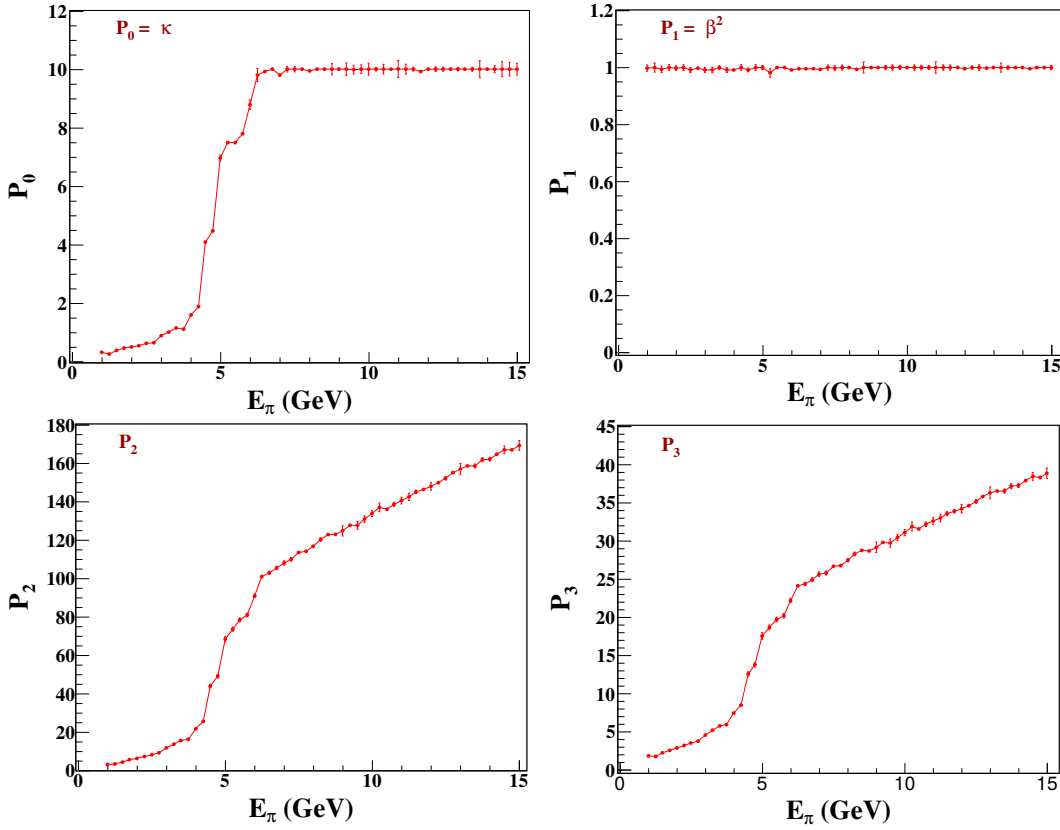
Figure 4.4: The parameters P_0, P_1, P_2 and P_3 of the Vavilov fit to the hit multiplicity, as functions of pion energy, for fixed-energy charged pions. [10]

4.3.1   ANALYSIS OF THE PION HIT PATTERN

The energy resolution of pions can be parameterized using the Vavilov fit, which has four parameters, P_0, P_1, P_2 and P_3. In Fig. 4.4 the variation of the Vavilov parameters P_0, P_1, P_2, P_3 with pion energy are shown. The *mean* and σ are obtained from these parameters via Eq. (4.6). The main features of the Vavilov distribution may be captured by the two parameters mean and sigma. However the remaining information in the Vavilov parameters enables a good fit even in the regions of low hit multiplicity and the tail of high hit multiplicity. These parameters can be used to reconstruct the hit distributions at any given energy.

Note that for $P_0 \gtrsim 10$, Vavilov distribution reduces to a Gaussian pdf with the corresponding *mean* and σ. In this analysis this happens for energies greater than $\sim$ 6 GeV. The actual power of Vavilov distribution is therefore apparent in the en-

ergy range $1 - 6$ GeV, which is the main region of interest for hadrons in ICAL.

The mean $\bar{n}(E)$ of the number of hits from the Vavilov fit at different energies is shown in the left panel of Fig. 4.5. It increases with increasing pion energy, and saturates at higher energies. It may be approximated by

$$\bar{n}(E) = n_0[1 - \exp(-E/E_0)] \, , \tag{4.7}$$

where n_0 and E_0 are constants. This fit has to be interpreted with some care, since n_0 and E_0 are sensitive to the energy ranges of the fit. The value of E_0 is found to be ~ 30 GeV when a fit to the energy range $1 - 15 \, GeV$ is performed. Since the energies of interest for atmospheric neutrinos are much less than E_0, Eq. (4.7) may be used in its approximate linear form $\bar{n}(E) = n_0 E/E_0$. A fit to this linear form is also shown in Fig. 4.5. Since in the linear regime ($E \ll E_0$)

$$\frac{\bar{n}(E)}{n_0} = \frac{E}{E_0} \, , \tag{4.8}$$

the energy resolution may be written as

$$\frac{\sigma}{E} = \frac{\Delta n(E)}{\bar{n}(E)} \, , \tag{4.9}$$

where $(\Delta n)^2$ is the variance of the distribution. In the rest of this thesis, the notation σ/E will be used for energy resolution, and Eq. (4.9) will be assumed to be valid.

The energy resolution of pions may be parameterized by

$$\frac{\sigma}{E} = \sqrt{\frac{a^2}{E} + b^2} \, , \tag{4.10}$$

where a and b are constants. The energy resolutions for charged pions as functions of pion energy are shown in the right panel of Fig. 4.5. The parameters a and b, extracted by a fit to Eq. (4.10) over the pion energy range $1 - 15$ GeV, are also shown in that figure.
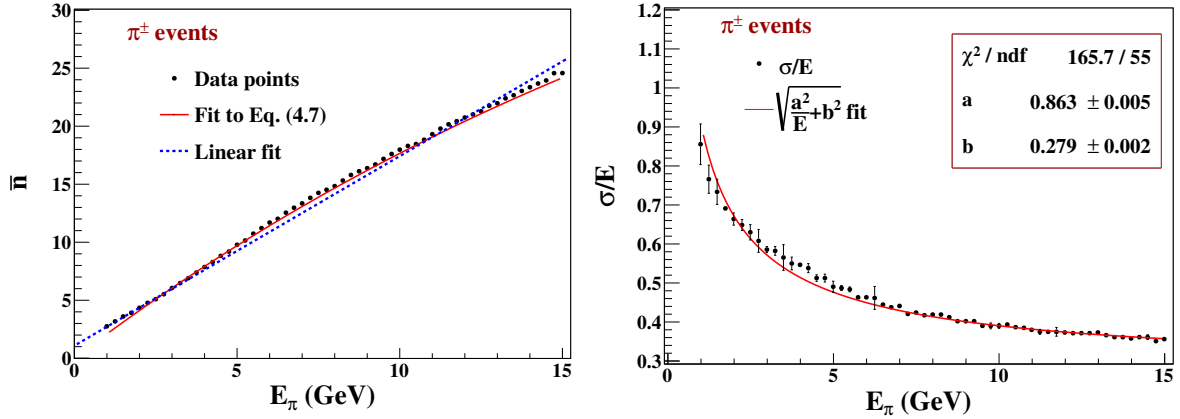
Figure 4.5: (Left) The mean number of $\pi^{\pm}$ hits from the Vavilov fit as a function of the pion energy. A linear fit and a fit to the Eq. (4.7) are also shown. (Right) The pion energy resolution as a function of pion energy. A fit to Eq. (4.10) is also shown. [10])

4.4   HADRON ENERGY RESPONSE IN ATMOSPHERIC NEUTRINO EVENTS

In section 4.3 the analysis of the energy resolution with single pion events has been described. But in reality there are multiple hadrons produced in the atmospheric neutrino interactions. In this section the analysis with hadrons produced in ν_μ interactions in the detector via quasi-elastic (QE), resonance, and deep inelastic scattering (DIS) processes is given. The QE process dominates at $E_\nu \sim 1$ GeV, and contains no hadron in the final state except for the recoil nucleon. Resonance events at a few GeV contain an additional hadron, typically a pion. As the energy increases, the DIS events that contain multiple hadrons in the final state dominate. The energy resolution has been obtained for both CC and NC processes.

Both atmospheric neutrino (ν_μ) and anti-neutrino ($\bar{\nu}_\mu$) events in ICAL, without incorporating the effects of neutrino oscillations, are generated using the neutrino event generator NUANCE (v3.5). The hadrons produced in these interactions are mostly pions, but there about 10% events with kaons and a small fraction of other hadrons as well. It is not possible to distinguish one hadron from the other using the hit pattern of the hadron shower. However, since the hit distribution of vari-

ous hadrons are similar to each other (see Fig. 4.2) and the NUANCE generator is expected to produce a correct mixture of different hadrons at all energies, it is sufficient to determine the hadron energy resolution at ICAL through an average of NUANCE events, without having to identify the hadrons separately. A total of 1000 kt-yr of events (which is equivalent to 20 years of exposure with the 50 kt ICAL), both CC and NC, were generated with NUANCE for this purpose.

For the CC interaction $\nu_\mu N \to \mu X$, the incident neutrino energy is given by

$$E_\nu = E_\mu + E_{\text{hadrons}} - E_N, \tag{4.11}$$

where E_N is the energy of the initial nucleon which is taken to be at rest, neglecting its small Fermi momentum. It can be seen from Eq. (4.11) that any uncertainty in measuring the hadron energy will directly affect the determination of incoming neutrino energy. The visible hadron energy depends on factors like the shower energy fluctuation, leakage of energy, and invisible energy loss mechanisms, which in turn affect the energy resolution of hadrons .

The parameter E'_{had}, defined as

$$E'_{\text{had}} = E_\nu - E_\mu , \tag{4.12}$$

is used to calibrate the detector response for the CC events. This parameter can directly be used to reconstruct the neutrino energy.

The CC events were binned into the various E'_{had} energy bins and the hit distributions (averaged over all angles) in these bins are fitted to the Vavilov distribution function. The energy dependence of the Vavilov fit parameters is shown in Fig. 4.6. This information has been used directly to simulate the hadron energy response of the detector for a χ^2 analysis to study the ICAL physics potential, which is described in Chapter 7.
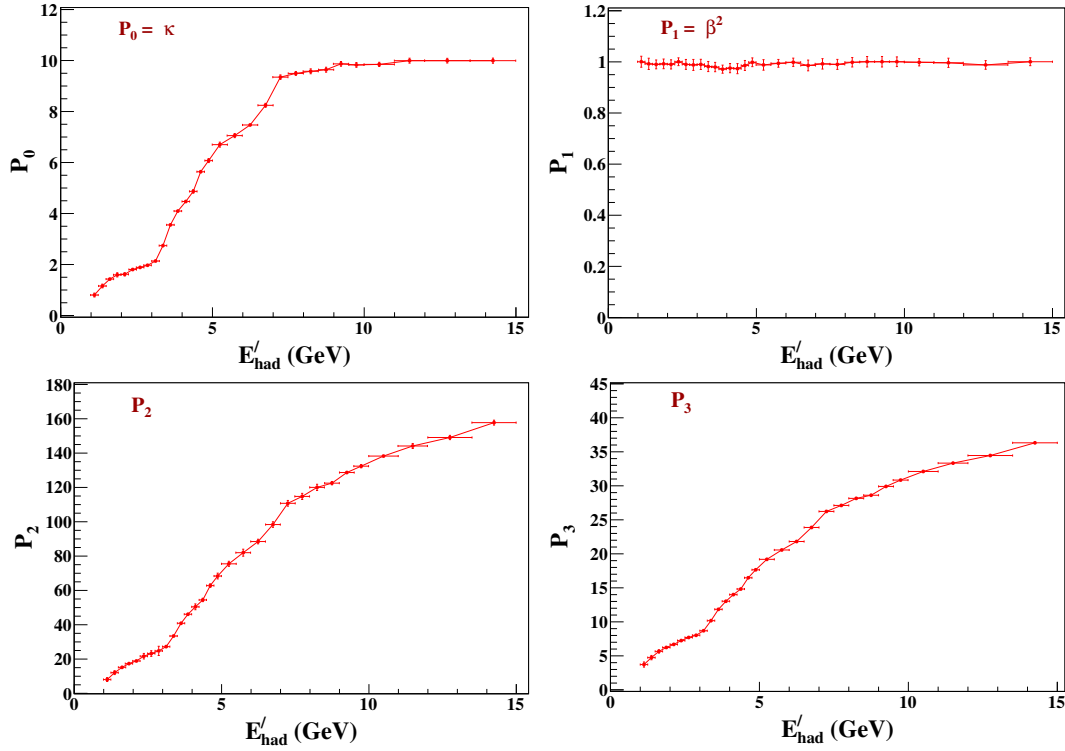
Figure 4.6: The Vavilov fit parameters P_0, P_1, P_2 and P_3 of the hit multiplicity, as functions of E'_{had}, from NUANCE data. These parameters can be directly used to reconstruct the hit distribution pattern. The bin widths are indicated by horizontal error bars. [10]

The mean value ($\bar{n}$) of the hit distributions, from the Vavilov fit, are shown in the left panel of Fig. 4.7 as a function of E'_{had} . As expected, these are similar to the mean values obtained earlier with fixed energy pions. Since the mean hits grow approximately linearly with energy, the same linearized approximation used in section 4.3.1 can be used to obtain the energy resolution $\sigma/E = \Delta n/\bar{n}$. The energy resolution as a function of E'_{had} is shown in the right panel of Fig. 4.7. The energy resolution ranges from 85% (at 1 GeV) to 36% (at 15 GeV).

In the case of NC events the above definition of E'_{had} is not valid. Thus the analysis has been performed using the total energy of the final state hadrons E_{h}, which is given by

$$E_{\text{h}} = (E_\nu + E_{\text{N}})_{\text{initial state}} - (E_\nu)_{\text{final state}}. \tag{4.13}$$

Fig. 4.8 shows the energy resolution of the hadrons produced in NC ν_μ interactions. This can be used to obtain the visible energy in the NC interactions.
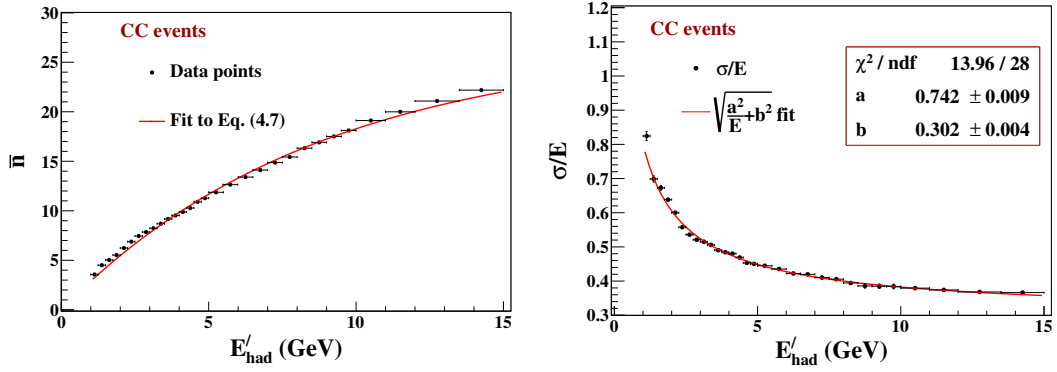
Figure 4.7: The mean hit distribution (left) and the energy resolution (right) for hadrons produced in CC events generated by NUANCE, as a function of E'_{had}. The right panel also shows a fit to Eq. (4.10). The bin widths are indicated by horizontal error bars. [10]
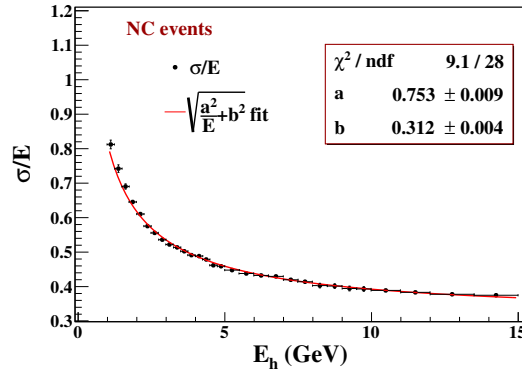
Figure 4.8: The energy resolution (right) for hadrons produced in NC events generated by NUANCE, as a function of the total hadron energy E_h. It also shows a fit to Eq. (4.10).

The effective energy response obtained from the NUANCE-generated data is an average over the mixture of many hadrons that contribute to hadron shower at all energies. The fractional weights of different kinds of hadrons produced in neutrino interactions may, in principle, depend upon neutrino oscillations. In addition, the relative weights of events with different energy that contribute in a single energy bin changes because neutrino oscillations are energy dependent. Events with oscillations using the best–fit values of standard oscillation parameters (mixing angles and mass–squared differences) were also generated. The resolutions obtained without and with oscillations are very close to each other. Thus, the hadron energy resolution can be taken to be insensitive to oscillations.

4.4.1 DEPENDENCE OF THE HADRON ENERGY RESOLUTION ON THE AVERAGE DIRECTION OF THE SHOWER

The number of layers traversed by the hadrons in a shower, and the net hits would depend on the direction of the hadrons. Thus, energy resolution for hadrons is expected to depend on their directions. Since it is not experimentally possible to identify the individual hadrons in an event in ICAL, the average zenith angle (θ_{had}) of the hadrons has been used as the parameter to check the angular dependence of the energy resolution. The average direction (true) of a set of hadrons are obtained by calculating the average momentum from their individual incident momenta obtained from NUANCE. The feasibility of the measurement of this parameter will be discussed in Chapter 5.

The events are divided into eight $\cos\theta_{had}$ bins, and the energy resolution is compared. The hadron energy resolution as a function of $\cos\theta_{had}$, at a few representative E'_{had} values, is shown in Fig. 4.9. The energy resolutions marginally vary with $\cos\theta_{had}$, the worse value being in the $\cos\theta_{had}$ range [-0.2 to 0.2]. Note that, the direction of the individual hadrons in an event may vary significantly from the average direction, and those would affect the net number of hits deposited as well as the number of layers crossed in that event.
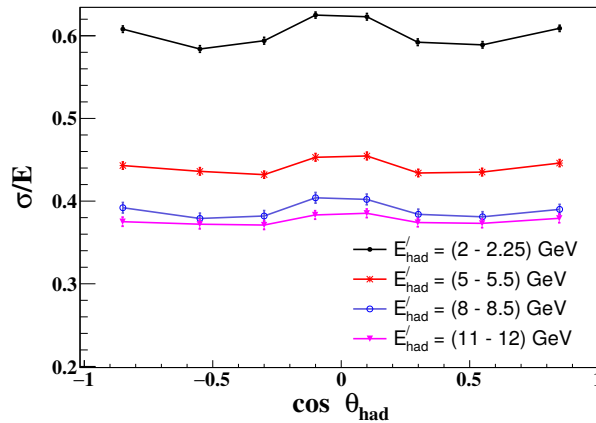
Figure 4.9: The hadron energy resolution (σ/E) as a function of $\cos\theta_{had}$ at a few representative energies.

4.5 HADRON ENERGY CALIBRATION

When the actual ICAL detector starts collecting the data, the only available observable for the hadrons are the hits. Therefore, a calibration of the hit multiplicity with the hadron energy in the simulation level is essential. In order to obtain the calibration, the hadron energy from simulated NUANCE CC event data were divided into $hit\_$n bins, where $hit\_$n corresponds to n number of hadron hits. Sample energy distributions at $n = 10, 25$ are shown in Fig. 4.10.
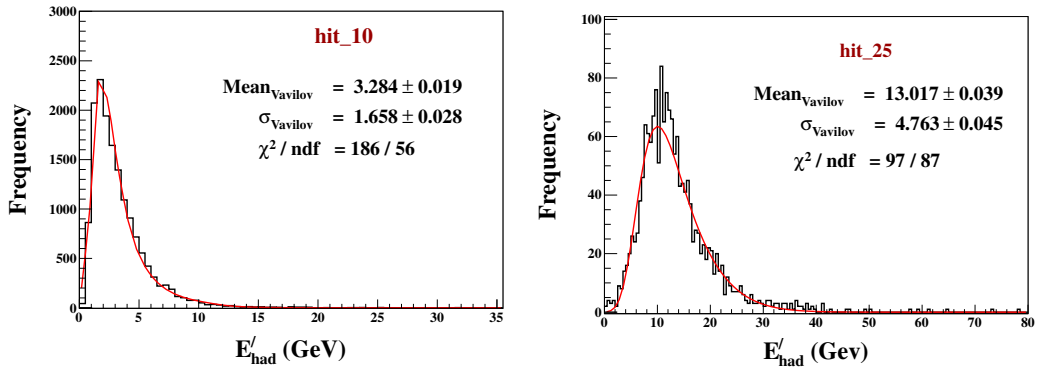
Figure 4.10: The hadron energy distributions for hit multiplicities 10 (left) and 25 (right). They are fitted to the Vavilov PDF. [10]

Even here, a good fit is obtained with the Vavilov distribution function at all hit multiplicities. The variation of the Vavilov parameters with hit multiplicity is shown in Fig. 4.11 using which the hadron energy can be reconstructed. The value of P_0 is of the order of 0.1–1 at all hit multiplicities, which indicates that a Gaussian distribution does not give a good fit. The $mean_{\text{Vavilov}}$ and σ_{Vavilov} obtained from the fit are used to produce the calibration plot presented in Fig. 4.12. From the hit multiplicity of the hadron shower in any event in ICAL, the hadron energy can be estimated using this information. This can then further be used to reconstruct the energy and direction of the incident neutrinos.
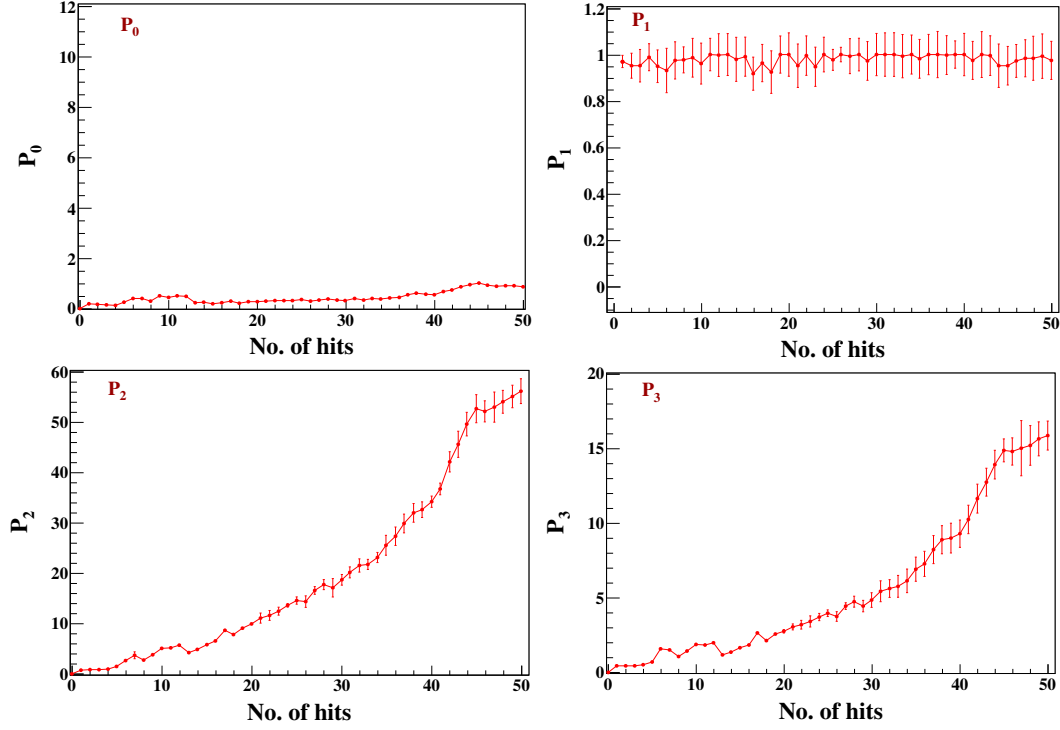
Figure 4.11: The parameters P_0, P_1, P_2 and P_3 of the Vavilov fit to the E'_{had} distributions, as functions of the number of hadron hits, from NUANCE data. These parameters can be directly used to reconstruct E'_{had} for an event when the number of hadron hits are known.
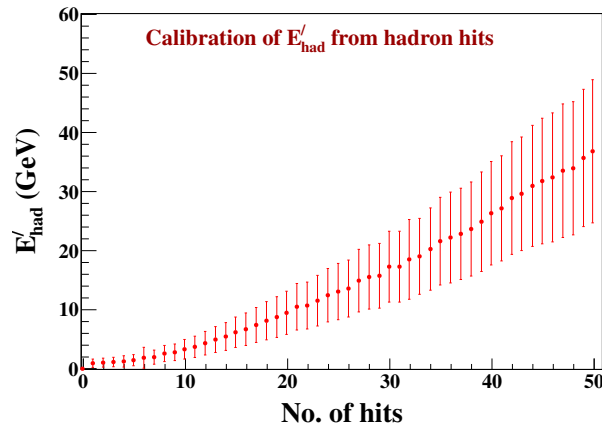
Figure 4.12: Calibration plot for E'_{had}, where *mean* and σ from the Vavilov fits are represented by the red filled circles and error bars, respectively. [10]

4.6 REMARKS

The ICAL detector, primarily optimized to be a good tracking detector for the muons produced in CC atmospheric ν_μ events, is also sensitive to the final state hadrons. The inclusion of the hadron information is expected to improve the detector's sensitivity. Reconstructing the hadron energy and directions is also the only way to investigate the NC events, which can provide information on the tau neutrinos, as well as, on phenomena like active – sterile oscillations.

In this chapter, the methodology and results of a GEANT4–based simulation of the ICAL detector, employed to obtain the energy calibration of hadrons from the hadron hit pattern and to obtain their energy resolutions, has been shown.

The hadron events in the ICAL detector primarily consist of charged pions, with a small fraction of other hadrons. The ICAL would not be able to separate different hadrons in the detector. The parameter $E'_{\mathrm{had}}(= E_\nu - E_\mu)$, is used to parametrize the net hadron energy in an event. The hit patterns can be fitted to the Vavilov distribution. A resolution in the range $85\% - 36\%$ is obtainable for hadrons produced in CC neutrino interactions, at $1 - 15$ GeV. The calibration for the energy of the hadron shower as a function of the hit multiplicity has also been obtained. The Vavilov fit parameters are used for simulating the hadron energy response of the detector to perform the physics analyses studies, as described in Chapter 7. These results can also be used to reconstruct the total visible energy in NC events. In the case of the CC events, the total neutrino energy can be reconstructed using the information on muon and hadrons, which is discussed in Chapter 6.

ICAL will be among the largest neutrino detectors sensitive to the hadrons, and thus it is essential to fully explore its potential to the hadrons. Further information on the hadron shower may be obtained from the shower shape and spread, which would provide information on the average direction of the shower. In Chapter 5, the reconstruction of the shower direction from the shower shape will be discussed.

Chapter 5

THE HADRON SHOWER DIRECTION RESOLUTION OF ICAL

The upward going neutrinos passing through the Earth's core and experiencing significant matter effects and MSW resonances would be very crucial for the physics sensitivity of the ICAL. Thus it is required to be able to distinguish between the up-going and down-going neutrinos at ICAL. The incident neutrino direction may be retraced from the final state particles using four–momentum conservations, if the momenta of those final state particles are reconstructed. The muon momentum is reconstructed using a Kalman–Filter based algorithm. As has been shown in section 3.3.2, the muon direction can be reconstructed with a good precision ($< 1°$) [9]. In the case of the hadrons, since ICAL is not capable of distinguishing between individual hadrons on the basis of the hits recorded, it is not possible to reconstruct the direction of each hadron. However, an estimation of the average direction of the hadrons can be done using the shape of the hadron shower. Two methods namely the centroid technique and the orientation matrix technique have been taken up for this purpose. Both of the techniques use the position vectors of the shower hits with respect to the neutrino interaction vertex. The vertex can be reconstructed in the CC

This chapter is based on [12], which is in preparation.

events using the muon track reconstruction algorithm.

In addition, since the RS interaction events typically contain a single pion and the DIS events contain multiple hadrons, the shower shape for this two interactions are expected to be different to some extent. Thus shower shape can also be used to differentiate between these two interaction processes.

In this chapter the two approaches towards the shower direction reconstruction are discussed. The resolution of the shower direction has also been quantified here. The separation of the DIS and RS events on the basis of the shower shape has also been reported.

5.1 THE RECONSTRUCTION METHODOLOGY

The average direction of a shower like feature would depend on its shape and extent. For the hadron showers in ICAL, the position vectors of the hits in an event with respect to the interaction vertex, have been used to extract the relevant information. Two different techniques are tested for the shower direction reconstruction.

5.1.1 CENTROID TECHNIQUE

For each simulated event, the vertex position and the positions of hits forming the shower are obtained. Each event is required to have at least one hit for analysis. At $E'_{\text{had}} = 1$ GeV, 10% of the events fail to meet this constraint. However as energy increases, the fraction of the useful events increases and at 5 GeV, only 0.5% events are rejected. The direction of the centroid of the shower is found by summing over the position vectors of each hit in that event [17]. For a shower constituting of N hits with position coordinates $(x_i, y_i, z_i; i = 1, ..., N)$, if the vertex is (x_0, y_0, z_0), the direction of the centroid of the shower can be expressed as the vector $P(X, Y, Z)$

with

$$X = \sum_{i=1}^{N}(x_i - x_0),$$

$$Y = \sum_{i=1}^{N}(y_i - y_0), \tag{5.1}$$

$$Z = \sum_{i=1}^{N}(z_i - z_0).$$

The position vectors along the Z–axis are normalized to one layer to avoid overestimation due to hits by the same particle in multiple layers. The direction of the vector P is taken to be the reconstructed shower direction from the centroid technique.

5.1.2 ORIENTATION MATRIX TECHNIQUE

Additional information on the shower spread can be included by take into account the higher order moments through the orientation matrix technique [17].

For a collection of unit vectors $(x_i,\ y_i,\ z_i)$, $i =\ 1,\ ...,\ N$, the symmetric orientation matrix T is defined as

$$T = \begin{pmatrix} \sum_{i=1}^{N} x_i^2 & \sum_{i=1}^{N} x_i y_i & \sum_{i=1}^{N} x_i z_i \\ \sum_{i=1}^{N} x_i y_i & \sum_{i=1}^{N} y_i^2 & \sum_{i=1}^{N} y_i z_i \\ \sum_{i=1}^{N} x_i z_i & \sum_{i=1}^{N} y_i z_i & \sum_{i=1}^{N} z_i^2 \end{pmatrix}. \tag{5.2}$$

The eigenanalysis of this symmetric matrix gives an idea of the shape of the underlying distribution.

If a unit mass is assumed to be placed at each point, then the moment of inertia of the N points about any arbitrary axis $(x_{\mathrm{arb}}, y_{\mathrm{arb}}, z_{\mathrm{arb}})$ is

$$N - \begin{pmatrix} x_{\mathrm{arb}} & y_{\mathrm{arb}} & z_{\mathrm{arb}} \end{pmatrix} T \begin{pmatrix} x_{\mathrm{arb}} \\ y_{\mathrm{arb}} \\ z_{\mathrm{arb}} \end{pmatrix} \tag{5.3}$$

As the choice of axis varies, the variation of this moment of inertia gives information about the scatter of the points around that axis. The axis about which the moment is least, is the principal axis and it is defined to be the shower direction. The MIGRAD and SIMPLEX minimizer algorithms, inbuilt in the TMinuit class in ROOT, are used for this calculation [16] .

5.2   THE RESULTS

The results of the hadron shower reconstruction using the two methods described in section 5.1 for CC ν_μ events propagating through a 200 cm $\times 200$ cm $\times 200$ cm volume in the central region of the detector are presented here. The resolution of two reconstructed quantities, the average shower direction vector (α_{had}) and the average zenith angle (θ_{had}) has been obtained.

5.2.1   THE α_{had} RESOLUTION

The parameter α_{had} is defined as the angle between the reconstructed shower direction and the true shower direction. The true shower direction is obtained from the net momentum of the hadrons constituting the shower, as available from the NU-ANCE generator. Fig. 5.1a shows the comparison of the α_{had} distributions obtained from both the centroid and the orientation matrix methods, at $E'_{\mathrm{had}} = 4.5 - 5$ GeV and $\cos\theta^{true}_{had} = [1, \, 0.8]$. Clearly, the latter method gives a marginally better result.
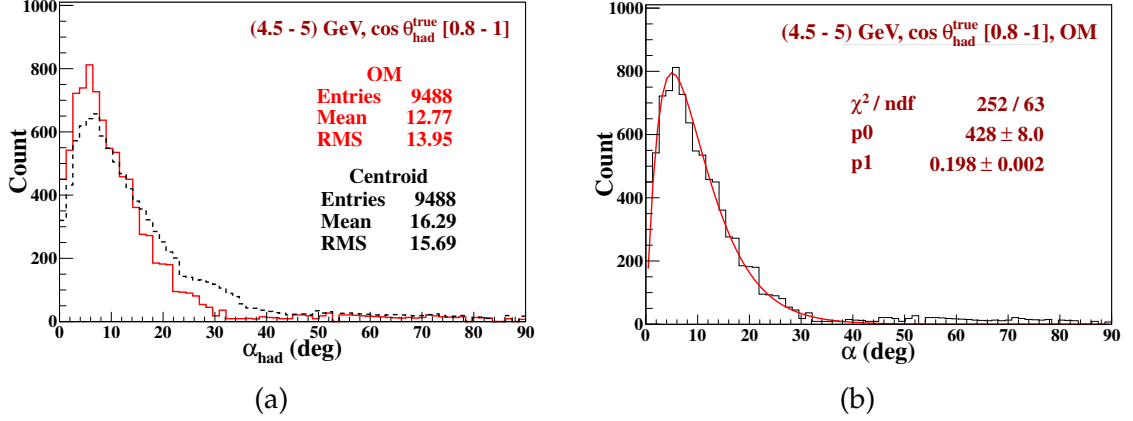
Figure 5.1: (a) The α_{had} distributions from the centroid and orientation matrix methods, at $E'_{\mathrm{had}} = 4.5 - 5 \ GeV$ and $\cos\theta_{had}^{true} = [1, 0.8]$. (b) The α_{had} distribution from the orientation matrix technique, fitted to Eqn. (5.4). Here, the parameters $p0 = A$, and $p1 = B$.

In Fig. 5.1b the α_{had} distribution from the orientation matrix technique is fitted with the function

$$f(\alpha_{had}) = A \cdot \alpha_{had} \cdot \exp(-B \cdot \alpha_{had}), \tag{5.4}$$

where A and B are the two parameters using which the mean and the standard deviation of the distribution can be calculated. Note that, the fraction of events within 1σ, 2σ and 3σ confidence level of the actual α_{had} value are roughly 82%, 94% and 98% respectively. It is different from the typical significance levels in the case of normal distributions. The direction resolution $\sigma_{\alpha_{had}}$ is defined as

$$\sigma_{\alpha_{had}} = \sqrt{\langle(\alpha_{had})^2\rangle - \langle\alpha_{had}\rangle^2}, \tag{5.5}$$

where $\langle\alpha_{had}\rangle$ and $\langle(\alpha_{had})^2\rangle$ are calculated using the fit parameters A and B. In terms of the fit parameters,

$$\sigma_{\alpha_{had}} = \frac{\sqrt{2}}{B}. \tag{5.6}$$
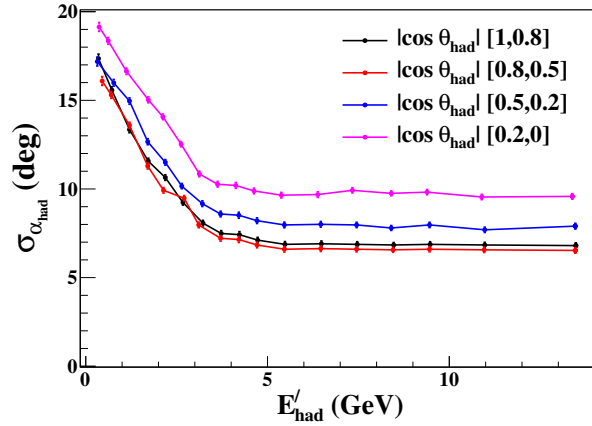
Figure 5.2: The direction resolution $\sigma_{\alpha_{had}}$ as a function of the E'_{had}, in the $|\cos\theta_{had}|$ bins $[1, \ 0.8]$, $[0.8, \ 0.5]$, $[0.5, \ 0.2]$, and $[0.2, \ 0]$.

In Fig. 5.2 the direction resolution $\sigma_{\alpha_{had}}$ is shown as a function of the E'_{had}, in the $|\cos\theta_{had}|$ bins $[1, \ 0.8]$, $[0.8, \ 0.5]$, $[0.5, \ 0.2]$, and $[0.2, \ 0]$. In the $|\cos\theta_{had}|$ bin $[0.2, \ 0]$, the direction resolution is worse. It is due to the geometry, since the thickness of the iron plate traversed increases with increasing zenith angle, and it affects the number of hits recorded.

5.2.2   THE θ_{had} RESOLUTION

The quantity $\Delta\theta_{had}$ is defined as

$$\Delta\theta_{had} = \theta_{had}^{rec} - \theta_{had}^{true}. \tag{5.7}$$

The distributions of $\Delta\theta_{had}$, obtained from the two methods, are shown in Fig. 5.3a. As expected, the orientation matrix gives a improved estimation of θ_{had}. In Fig. 5.3b the $\Delta\theta_{had}$ distribution from orientation matrix technique, is fitted to the Breit–Wigner distribution. The functional form of the Breit–Wigner distribution is given by

$$L(x) = \frac{1}{\pi}\frac{\frac{\Gamma}{2}}{(x - x_0)^2 + \frac{\Gamma}{2}^2}, \tag{5.8}$$

where Γ is the FWHM, i.e., the full width at half maximum and x_0 is the mean. The

resolution of θ_{had} is defined as

$$\sigma_{\theta_{had}} = \frac{\Gamma}{2.35}. \tag{5.9}$$

(a)   (b)
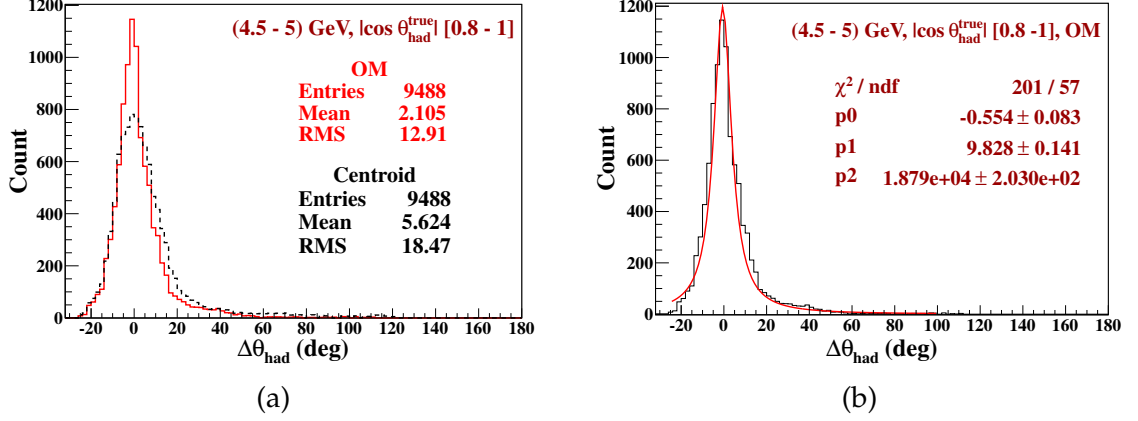
Figure 5.3: (a) The $\Delta\theta_{had}$ distributions from the centroid and orientation matrix methods, at $E'_{\text{had}} = 4.5 - 5$ GeV and $\cos\theta^{true}_{had} = [1, 0.8]$. (b) The $\Delta\theta_{had}$ distribution from the orientation matrix technique, fitted to Eqn. (5.4). Here, the parameters p0 = x_0, and p1 = Γ.
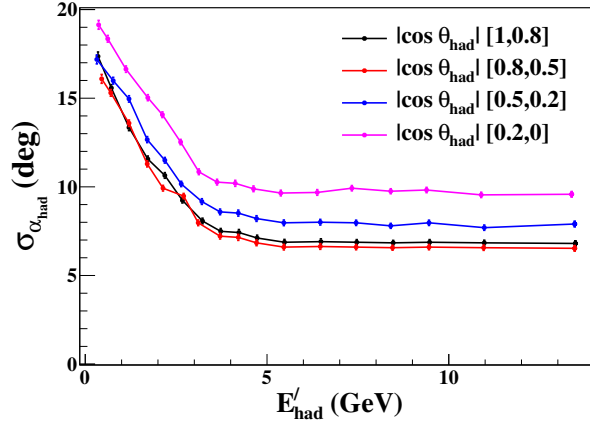
Figure 5.4: The direction resolution $\sigma_{\alpha_{had}}$ as a function of the E'_{had}, in the $|\cos\theta_{had}|$ bins [1, 0.8], [0.8, 0.5], [0.5, 0.2], and [0.2, 0].

In Fig. 5.4 the direction resolution θ_{had} is shown as a function of the E'_{had} in the $|\cos\theta_{had}|$ bins [1, 0.8], [0.8, 0.5], [0.5, 0.2], and [0.2, 0]. A lookup table in terms of the fit parameters and resolutions as a function of energy can further be used to include θ_{had} in a statistical analysis of the ICAL sensitivity. The shape of the shower can also be used to separate the RS and DIS events, which is discussed in section 5.3.

5.3 SEPARATION OF RS AND DIS EVENTS

The hadron showers produced in the resonance scattering (RS) and the deep in-elastic scattering (DIS) interactions of ν_μ are expected to differ in shape. The RS processes usually produce a single pion, whereas the DIS processes produce multi-ple hadrons. Thus the shower spreads in the case of the DIS events are expected to be larger than those in the RS events.

A quantity P_t has been defined to study the transverse extent of the hits in a shower. For a shower with N hits, it is given by

$$P_t = \sum_{i=1}^{N} p_i, \qquad (5.10)$$

where p_i is the perpendicular distance of the ith hit on the average direction vector of the shower.

(a)   (b)
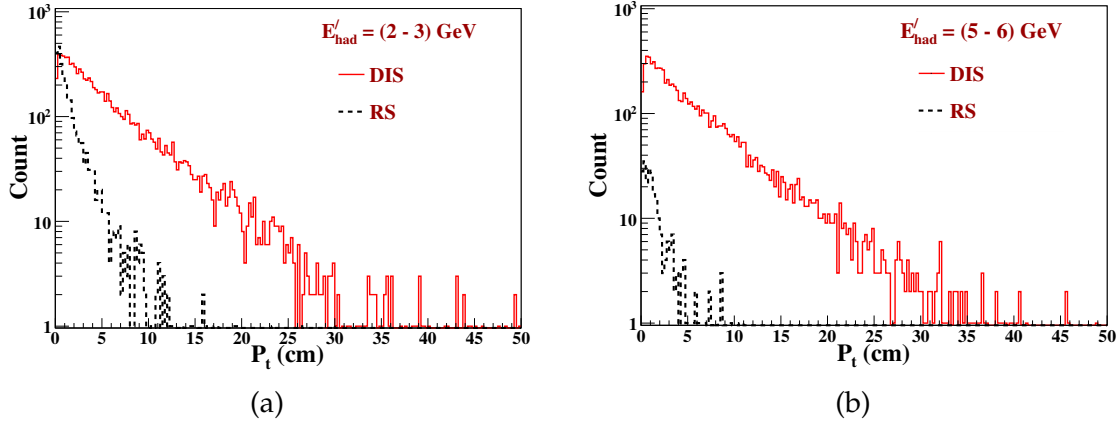
Figure 5.5: The comparison of the distribution of the transverse spread P_t for the RS and DIS interaction events at (a) $E'_{\text{had}} = (2-3)$ GeV and (b) $E'_{\text{had}} = (5-6)$ GeV.

In Fig. 5.5 the distributions of the transverse spread P_t for the RS and DIS inter-action events are compared at $E'_{\text{had}} = (2-3)$ GeV and $E'_{\text{had}} = (5-6)$ GeV. As expected, the spread in the RS events is much narrower than that in the DIS events. Thus the quantity P_t is a useful tool to separate out the two different interaction processes.

5.4 REMARKS

In this chapter the methodology and results of the reconstruction of the mean direction of the hadron shower are discussed. It is difficult to reconstruct the average direction of the hadron showers as accurately as that of muons, however even an approximate estimation is also useful to obtain additional information on the hadron showers. The hadron information of the hadron hits, in terms of their position vectors with respect to the interaction vertex, are used. In the first approach, the direction of the centroid of the hadron shower is obtained. The accuracy of reconstruction is slightly increased in the second approach, by taking into account the higher order moments by the use of an orientation matrix. A resolution in the range $20° - 7°$ is obtained for the average direction vector of the hadron shower. Similar resolutions are also obtained for the mean zenith angle of the hadrons. These results may be used to have the hadron direction as an observable for the ICAL physics studies.

The shower shape can also be used to differentiate between different types of interactions. The RS events produce a single pion, and the shower is expected to be narrower. While, the DIS events produce multiple hadrons, and the showers are broader. The net transverse extent of the hits with respect to the shower direction vector is a useful quantity, and can be used to separate these interactions.

The reconstructed hadron energy is then used to reconstruct the neutrino direction. This will be described in Chapter 6.

Chapter 6

THE RECONSTRUCTION OF NEUTRINO ENERGY AND ANGLE

The reconstruction techniques and the resolutions of the muon momentum and its direction, and those of the hadron energy and the average direction of the hadron shower, have been discussed in Chapters 3, 4 and 5 respectively. These reconstructed parameters are then used to reconstruct the energy and direction of the incident neutrino in the CC interaction events.

To reconstruct CC ν_μ events, events with a reconstructed muon momentum are considered. Note that this analysis is done with the events fully contained (FC) in the ICAL detector. It is assumed that, the muon track and the hadron shower can be separated with 100% efficiency. Applying the energy and momentum conservation, the energy and direction of the incident neutrino have been reconstructed. The efficiency of reconstruction of the neutrino events and their leptonic charge identification, the neutrino energy and direction resolution in ICAL are discussed and quantified in this chapter.

This chapter is based on [12], which is in preparation.

6.1 THE RECONSTRUCTION EFFICIENCY

The reconstruction efficiency (ϵ_{rec}^{ν}) of the ν_μ events is defined as

$$\epsilon_{rec}^{\nu} = \frac{N_{rec}}{N_{total}}, \text{ with error } \delta\epsilon_{rec}^{\nu} = \sqrt{\epsilon_{rec}^{\nu}(1 - \epsilon_{rec}^{\nu})/N_{total}}, \tag{6.1}$$

where N_{rec} is the number of events with reconstructed muon momentum irrespective of the charge, and N_{total} is the total events. Here the criteria on the muon track fitting has been taken as $\chi^2/ndf < 10$.
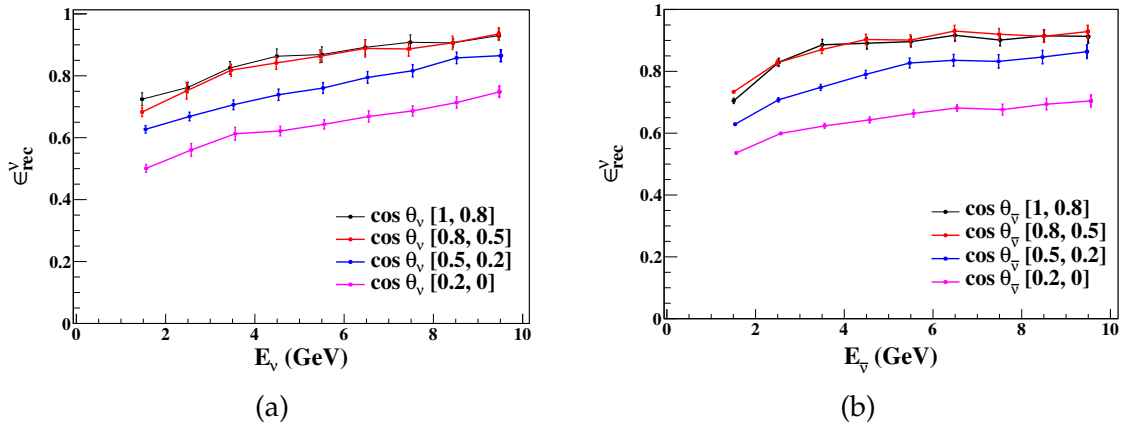
Figure 6.1: The reconstruction efficiency of the (a) CC ν_μ events, and, (b) CC $\bar{\nu}_\mu$ events in ICAL, as a function of the neutrino energy for the $|\cos\theta_\nu|$ bins, $1-0.8$, $0.8-0.5$, $0.5-0.2$ and $0.2-0$.

The neutrino event reconstruction efficiency, as a function of the input neutrino energy (E_ν) and at certain $\cos\theta_\nu$ bins, is shown in Fig. 6.2. It ranges between 40% to 90% in various (E_ν, $\cos\theta_\nu$) bins.

6.2 THE CHARGE IDENTIFICATION EFFICIENCY

The neutrinos and antineutrinos are differentiated by the separation of the muon and antimuon tracks by virtue of their direction of bending in the magnetic field in the ICAL. The (leptonic) charge reconstruction efficiency (ϵ_{cid}^{ν}) of the CC neutrino

events is defined as

$$\epsilon_{cid}^{\nu} = \frac{N_{tc}}{N_{rec}}, \text{ with error, } \delta\epsilon_{cid}^{\nu} = \sqrt{\epsilon_{cid}^{\nu}(1 - \epsilon_{cid}^{\nu})/N_{rec}}, \tag{6.2}$$

where N_{rec} is the number of events with reconstructed muon momentum irrespective of the charge, and N_{tc} is the number events with correct charge identification. The charge identification efficiency of the neutrinos, as a function of the input neutrino energy (E_{ν}) and at certain $\cos\theta_{\nu}$ bins, is shown in Fig. 6.2. It varies between 65% to 90% in various ($E_{\nu}, \cos\theta_{\nu}$) bins.
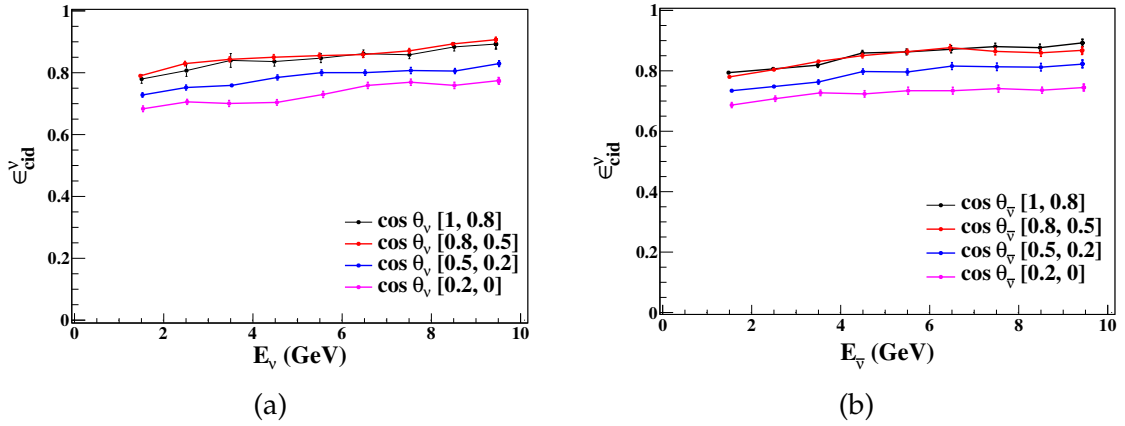
Figure 6.2: The charge identification efficiency of the (a) CC ν_{μ} events, and, (b) CC $\bar{\nu}_{\mu}$ events in ICAL, as a function of the neutrino energy for the $|\cos\theta_{\nu}|$ bins, $1 - 0.8$, $0.8 - 0.5$, $0.5 - 0.2$ and $0.2 - 0$.

6.3 THE NEUTRINO ENERGY RESOLUTION

The muon energy (E_{μ}) is reconstructed using a Kalman filter based algorithm, as discussed in section 3.2. The hadron energy parameterized by E'_{had} is estimated using the calibration of E'_{had} against hadron hits (as stated in section 4.5). The neutrino energy is reconstructed as

$$E_{\nu}^{\text{rec}} = E_{\nu}^{\text{rec}} + E'_{\text{had}}. \tag{6.3}$$

Fig 6.3 shows a typical distribution of ($E_{\nu}^{\text{rec}} - E_{\nu}^{\text{true}}$). Those distributions at various ($E_{\nu}, \cos\theta_{\nu}$) bins are fitted to the Vavilov distribution function. The relative neutrino

energy resolution, defined to be $\sigma_{\text{Vavilov}}/E_\nu$, at those bins are shown in Fig. 6.4. The energy resolution is found to be flat in the E_ν range $1 - 10$ GeV, in the range (22 $- 26)\%$. The reason is, though both the muon and the hadron energy resolution show sharper variation with energy, the neutrinos in any of the bins are composed of muons and hadrons in a wider energy range.
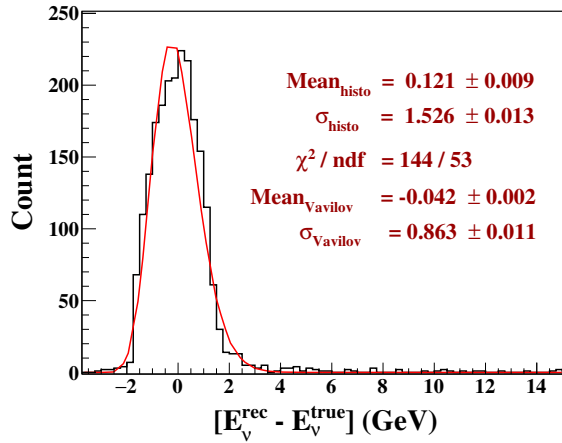
Figure 6.3: The distribution of $(E_\nu^{\text{rec}} - E_\nu^{\text{true}})$ for $E_\nu = 3.5 - 4$ GeV, and $|\cos \theta_\nu| = [0.8, 1]$.
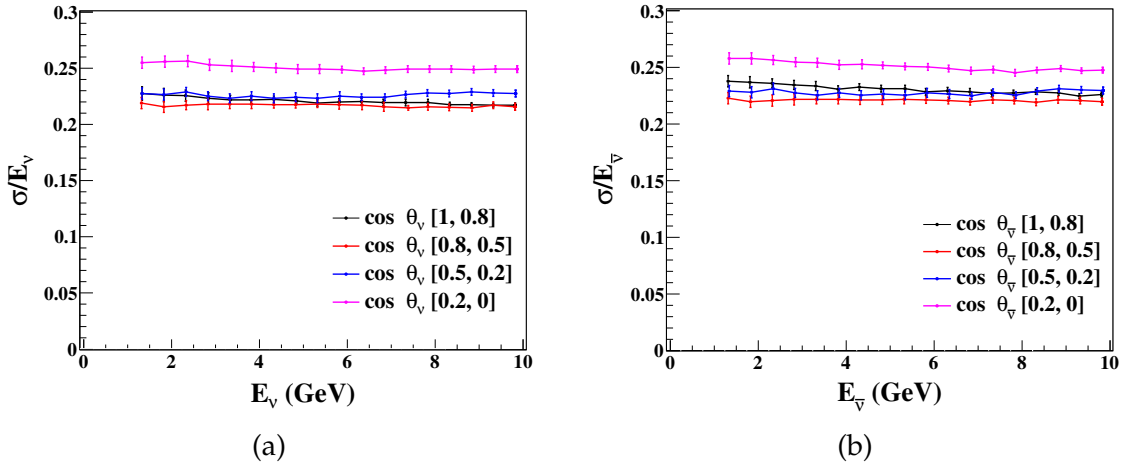
Figure 6.4: The energy resolutions of (a) ν_μ and (b) $\bar{\nu}_\mu$ in ICAL, as a function of the neutrino energy for the $|\cos \theta_\nu|$ bins, $1 - 0.8$, $0.8 - 0.5$, $0.5 - 0.2$ and $0.2 - 0$.

6.4 THE NEUTRINO DIRECTION RESOLUTION

The direction of the incident neutrino can be calculated via the four–momentum conservation of the neutrino interaction. The reconstructed parameters (energy and

momentum, direction) of the muon and the hadrons are used here. The resolution obtained through this method might be slightly coarser as it includes the uncertainties in the measurements of the parameters of both the muon and the hadrons. An alternative approach is the indirect estimation of the neutrino direction from the scatter angle between the incident neutrino and the muon, which does not include the the hadron reconstruction. Both of the methods are discussed in the following subsections.

6.4.1 THE θ_ν RESOLUTION USING HADRONS

The (X, Y, Z) projections of the neutrino momentum, in terms of the muon and hadrons, are given by

$$P_{\nu X} = P_\mu \cdot \sin\,\theta_\mu \cdot \cos\,\phi_\mu + P_{\text{had}} \cdot \sin\,\theta_{\text{had}} \cdot \cos\,\phi_{\text{had}}, \tag{6.4a}$$

$$P_{\nu Y} = P_\mu \cdot \sin\,\theta_\mu \cdot \sin\,\phi_\mu + P_{\text{had}} \cdot \sin\,\theta_{\text{had}} \cdot \sin\,\phi_{\text{had}}, \tag{6.4b}$$

$$P_{\nu Z} = P_\mu \cdot \cos\,\theta_\mu + P_{\text{had}} \cdot \cos\,\theta_{\text{had}}. \tag{6.4c}$$

The neutrino zenith angle θ_ν can then be calculated as

$$\tan\,\theta_\nu = \frac{\sqrt{P_{\nu X}^2 + P_{\nu Y}^2}}{P_{\nu Z}}. \tag{6.5}$$

The reconstructed P_μ, θ_μ, and ϕ_μ are obtained from the Kalman track fit algorithm. P_{had} is reconstructed using the calibration of $P_{\text{had}}^{\text{true}}$ against the hadron hit number, where $P_{\text{had}}^{\text{true}}$ is the sum of the momentum of all the hadrons in an event. The angles θ_{had} and ϕ_{had} are reconstructed from the hadron hit information using orientation matrix technique.

Fig. 6.5 shows a sample distribution of the difference between $\theta_{\nu_{\text{true}}}$ and $\theta_{\nu_{\text{rec}}}$. These distributions are fitted to the Breit–Wigner distribution function. The func-

tional form of the Breit–Wigner distribution is

$$L(x) = \frac{1}{\pi} \frac{\frac{\Gamma}{2}}{(x - x_0)^2 + \frac{\Gamma}{2}^2}.$$ (6.6)

The Lorentzian fit is parameterized with the mean (x_0) and the FWHM (Γ). The HWHM ($\Gamma/2$) is defined as the direction resolution which is shown in Fig. 6.6. It is in the range $19° - 7.5°$ depending on the neutrino energy and $\cos\theta_\nu$.
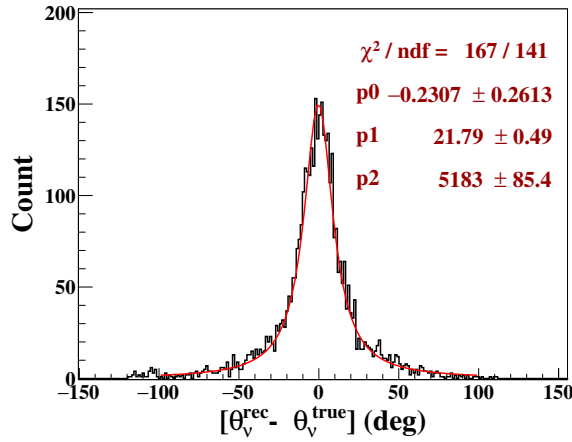
Figure 6.5: The distribution of $(\theta_{\nu_{\text{true}}} - \theta_{\nu_{\text{rec}}})$ for $E_\nu = 4$ - 5 GeV, and $|\cos\theta_\nu| = [0.8, 1]$.
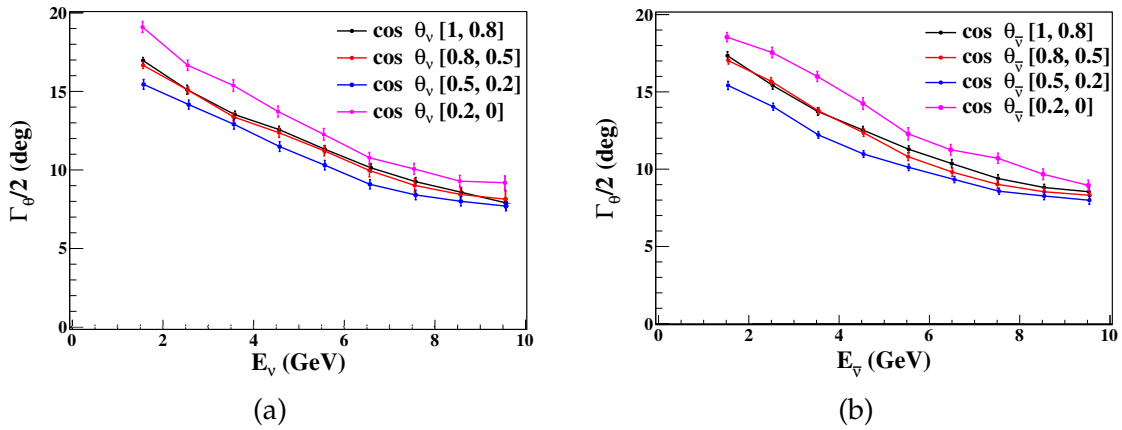
Figure 6.6: The zenith angle resolutions of (a) ν_μ, and (b) $\bar{\nu}_\mu$.

6.4.2 THE SCATTER ANGLE BETWEEN NEUTRINO AND MUON

The angle between the direction of the incident neutrino and the direction of the secondary muon, α_ν, also gives a naive estimation of the neutrino direction, when the muon direction is reconstructed. Since the muon direction reconstruction is quite precise in ICAL, this scatter angle would also provide information on the direction of the incident neutrino. However, note that, α_ν would provide an indirect hint of the neutrino direction.
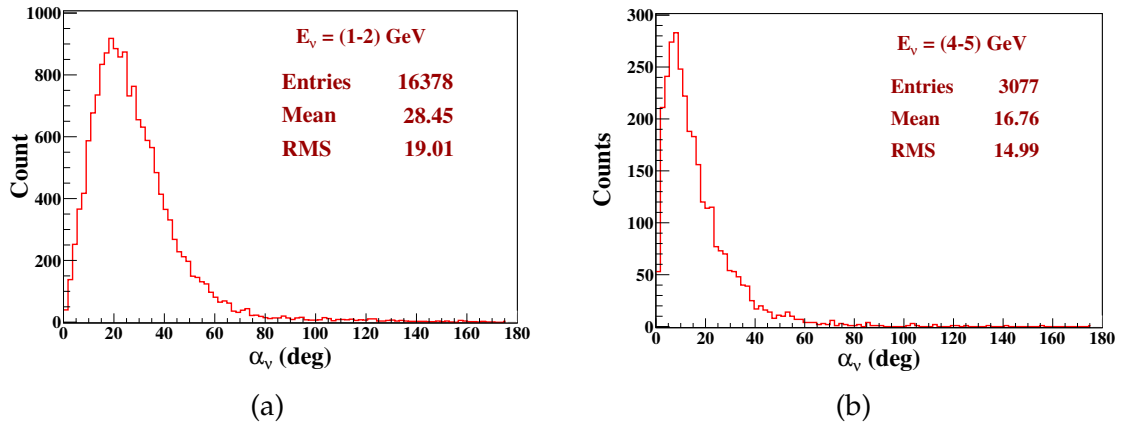
Figure 6.7: The α_ν distributions at (a) $E_\nu = 1 - 2$ GeV, and (b) $E_\nu = 4 - 5$ GeV.

Fig. 6.7 shows two sample α_ν distributions at $E_\nu = 1 - 2$ GeV, and, $E_\nu = 4 - 5$ GeV. The mean α_ν, as a function of the neutrino energy is shown in Fig. 6.8. This information, combined with other reconstructed parameters, can be used to extract the true direction of the incident neutrino.
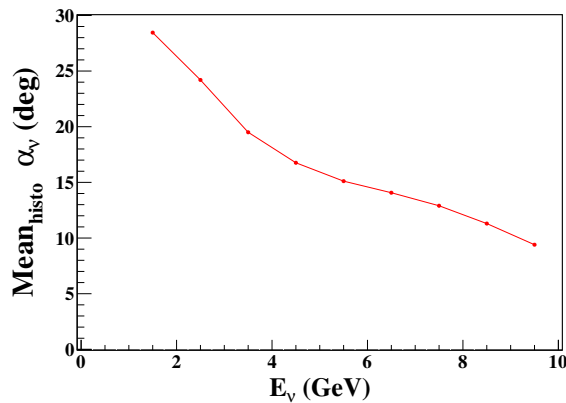
Figure 6.8: The distribution of ($\theta_{\nu_{\text{true}}} - \theta_{\nu_{\text{rec}}}$) for $E_\nu = 4$ - 5 GeV and $|\cos \theta_\nu| = [0.8, 1]$.

6.5 REMARKS

In this chapter, the reconstructions of the neutrino energy and direction are discussed. The energy and direction of the incident neutrino have been estimated from the reconstructed momentum of the final state particles through the application of the 4–momentum conservation. The neutrino energy is reconstructed by adding up the reconstructed energies of the muon and the hadrons in each event. For the events fully confined in ICAL, the energy resolution of neutrinos in the ICAL is in the range $(22 - 26)\%$. The muon and hadron momentum information is used to calculate the X, Y and Z projections of the neutrino momenta and eventually the neutrino direction. The resolution of the neutrino zenith angle at the ICAL is in the range ($19°$ – $7.5°$). In an alternative approach, the neutrino direction has also been estimated from the average scatter angle between the incident neutrino and the reconstructed final state muon.

The coarse neutrino energy and direction resolution, mentioned in this chapter, are still preliminary and would not be able to produce an improved physics sensitivity. It is due to the fact that, the naive addition of the reconstructed parameters of the muons and the hadrons dilute the advantage of the precise reconstruction of the muon momentum. Instead of this the use of the muon and the hadron resolutions separately, boosts the ICAL sensitivity towards its physics goals. This will be discussed in Chapter 7.

Chapter 7

ENHANCING THE ICAL PHYSICS REACH WITH HADRONS

The ICAL experiment would primarily aim to identify the neutrino mass hierarchy from the observations of atmospheric muon neutrinos. It would also improve the precision on the atmospheric neutrino mixing parameters as well as fulfill a number of other goals, which have been mentioned in Chapter 2. The design of ICAL is primarily optimized to measure the muon momentum. Further, the ICAL, being a magnetized detector, would also be able to separate the ν_μ and $\bar{\nu}_\mu$ events, through the distinction of the muon and antimuon tracks in the magnetic field. In addition, it is also capable of measuring the hadron energy in each event. Although the hadron energy is measured with relatively poorer resolution, it nevertheless contains crucial information on the event, which may be utilized when taken concomitant with the muon data. The capability of the ICAL, in reconstructing the muon and the hadron information, has been studied using a simulation framework, as described in Chapter 3 and Chapter 4, respectively.

The physics potential of ICAL, in fulfilling its prominent physics goals, can be studied from the event rates expected in the detector. The initial analysis of the

This chapter is based on JHEP **1410**, 189 (2014) [20].

physics reach was carried out using the muon momentum (E_μ, $\cos\theta_\mu$) only [18, 19]. In this section, the ICAL sensitivity, after adding the hadron energy information to the muon energy and muon direction in each event, has been discussed. It is observed that, the hadron energy, when added to the analysis by treating E_μ and E'_{had} as two separate variables in each event, improve the results significantly. In this approach, the correlation between these two quantities in each event is taken care of. The enhancement of the ICAL physics potential, for determining the neutrino mass hierarchy, the atmospheric mass squared difference and the mixing angle θ_{23}, and its octant, obtained using the values E_μ, $\cos\theta_\mu$ and E'_{had} from each event as independent variables has been presented in this chapter.

This chapter is started with a discussion on the Earth matter effects on the neutrino oscillation probabilities, which is the motivation behind the physics study with the ICAL detector. The exploration of the hadronic contribution in the neutrino events of interest in ICAL, the numerical analysis procedure and the enhanced results are then discussed in the subsequent sections.

7.1 THE EARTH MATTER EFFECT ON NEUTRINO OSCILLATION PROBABILITIES

The atmospheric muon neutrinos and antineutrinos are produces via the two channels, the survival channel $\nu_\mu \to \nu_\mu$ ($\bar{\nu}_\mu \to \bar{\nu}_\mu$), and the oscillation channel $\nu_e \to \nu_\mu$ ($\bar{\nu}_e \to \bar{\nu}_\mu$). For the sake of simplicity, if it is approximated that $|\Delta m^2_{21}| \ll |\Delta m^2_{31}|$ (or, $|\Delta m^2_{21}| \ll |\Delta m^2_{32}|$), then assuming a constant mater density, these two probabilities can be written as

$$P^m_{e\mu} = \sin^2\theta_{23} \sin^2 2\theta^m_{13} \sin^2\left[1.27(\Delta m^2_{31})^m \frac{L(\text{km})}{E(\text{GeV})}\right],\qquad(7.1)$$

and

$$P_{\mu\mu}^m = 1 - \cos^2\theta_{13}^m \sin^2 2\theta_{23} \sin^2\left[1.27\left(\Delta m_{31}^2 + A + (\Delta m_{31}^2)^m\right)\frac{L(\text{km})}{E(\text{GeV})}\right]$$
$$- \sin^2\theta_{23}^m \sin^2 2\theta_{23} sin^2\left[1.27\left(\Delta m_{31}^2 + A - (\Delta m_{31}^2)^m\right)\frac{L(\text{km})}{E(\text{GeV})}\right] \quad (7.2)$$
$$- \sin^4\theta_{23} \sin^2\theta_{13}^m \sin^2\left[1.27(\Delta m_{31}^2)^m\frac{L(\text{km})}{E(\text{GeV})}\right],$$

where the mass–squared difference $(\Delta m_{31}^2)^m$ and the mixing angle θ_{13}^m can be expressed in terms of their values in vacuum, as

$$(\Delta m_{31}^2)^m = \sqrt{(\Delta m_{31}^2\cos 2\theta_{13} - A)^2 + (\Delta m_{31}^2\cos 2\theta_{13})^2}, \quad (7.3)$$

and

$$\sin 2\theta_{13}^m = \frac{\Delta m_{31}^2 \sin 2\theta_{13}}{\sqrt{(\Delta m_{31}^2\cos 2\theta_{13} - A)^2 + (\Delta m_{31}^2\cos 2\theta_{13})^2}}. \quad (7.4)$$

Here $A = 2\sqrt{2}G_F n_e E$ is the MSW matter potential which depends on the Fermi coupling constant (G_F), the number density of the electrons (n_e) and the energy of the neutrinos (E). The corresponding probabilities for antineutrinos can be written by replacing A by $-A$ in the above probability expressions.

From the approximate probability expressions above, it can be seen that, for a non–zero θ_{13}, the values of $P_{e\mu}^m$ and $P_{\mu\mu}^m$ would be different for the normal hierarchy $(\Delta m_{31}^2 > 0)$ and the inverted hierarchy $(\Delta m_{31}^2 < 0)$. Also, the probability is different for neutrinos and antineutrinos. Fig. 7.1 illustrates this difference in the two probabilities, for a fixed $L = 7000$ km, and in the energy range $(0.5 - 20)$ GeV. Note that, the probability values plotted in this figure have been generated numerically, using the 24–layer PREM [130] profile of the Earth matter density and without neglecting the value of Δm_{21}^2. The set of oscillation parameters used to generate this figure has been mentioned in the figure caption. This distinction, through the detected event rates in ICAL, can be used to determine the true hierarchy. Since the ratio of atmospheric ν_μ to ν_e is nearly 2 in the sub–GeV energy range and the ratio increases at
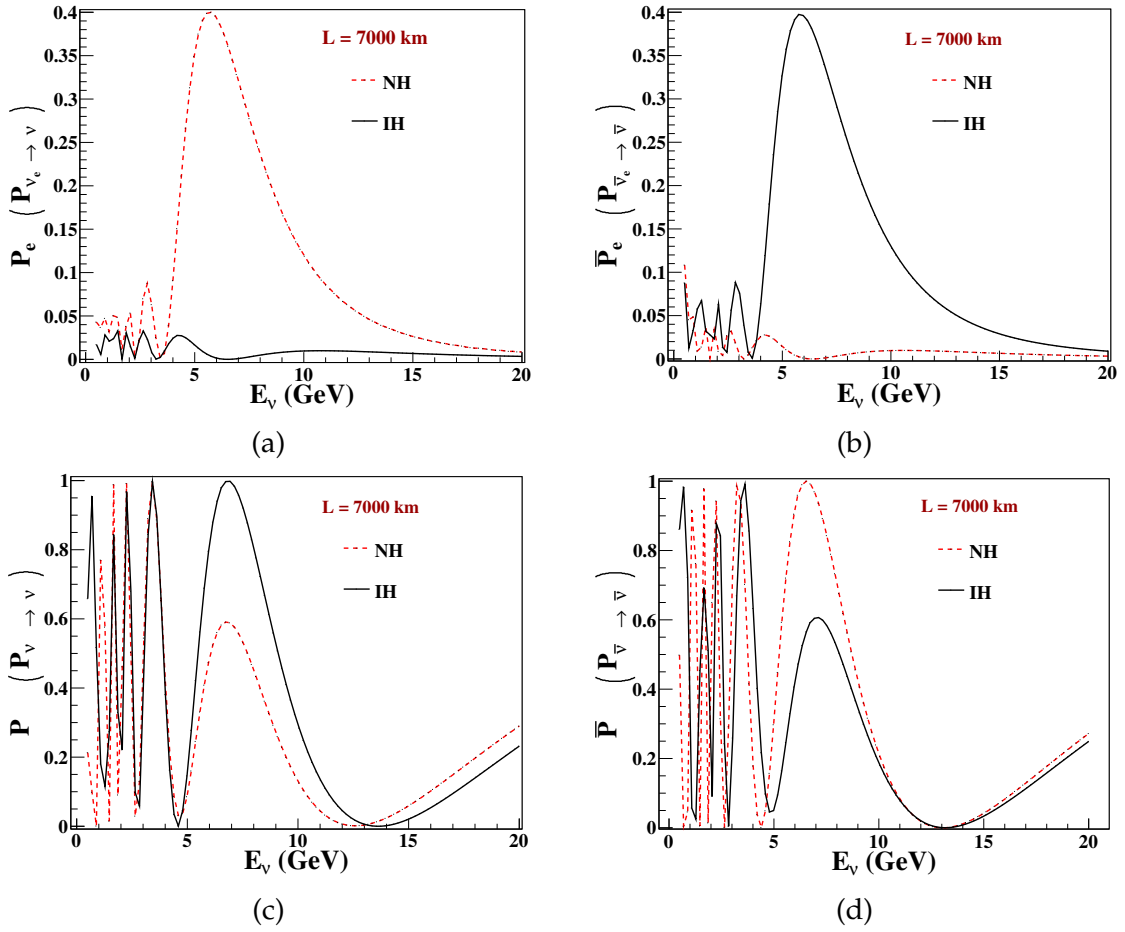
Figure 7.1: (a) The probabilities $P_{e\mu}^m$, (b) $\bar{P}_{e\mu}^m$, (c) $P_{\mu\mu}^m$ and (d) $\bar{P}_{\mu\mu}^m$, as a function of the neutrino (antineutrino) energy in the range $0.5 - 20$ GeV, at fixed $L = 7000$ km. Note that, the 24 layer PREM [130] profile of the Earth matter density has been used in the calculation of these probability values. The oscillation parameters used are, $\sin^2 2\theta_{13}$ = 0.1, $\sin^2 \theta_{23} = 0.5$, $\sin^2 2\theta_{12} = 0.84$, $\Delta m_{21}^2 = 7.5 \times 10^{-5}$ eV^2, $|\Delta m_{32}^2| = 2.4 \times 10^{-3}$ eV^2, $\delta_{CP} = 0$ deg.

higher energies, it is clear from Fig. 7.1 that the events in the detector would dominantly come from the survival channel of ν_μs.

The recent discovery of a non–zero θ_{13} at the reactor $\bar{\nu}_e$ disappearance experiments [99, 100, 101, 102, 103, 104] and at the accelerator $\nu_e/\bar{\nu}_e$ appearance experiments [108, 105, 106, 107], has does been a very good news for the experiments looking for the detection of the true mass hierarchy. The moderately large value of θ_{13} opens the gateway to probe the sub–leading three–flavor effects in current and future neutrino oscillation experiments. Thee mass hierarchy (MH), can be probed through the measurement of the matter effects on neutrinos as they pass through the
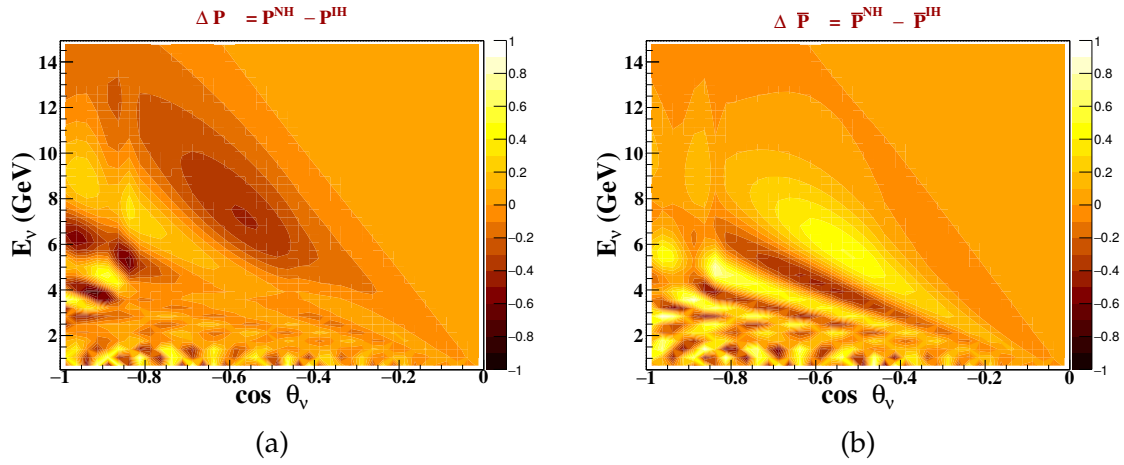
Figure 7.2: Oscillograms showing the value of the parameter $\Delta P_{\mu\mu}$ in the $E_\nu - \theta_\nu$ plane for (a) ν_μ and (b) $\bar{\nu}_\mu$. Note that, the 24 layer PREM [130] profile of the Earth matter density has been used in the calculation of the probability values. The oscillation parameters used are, $\sin^2 2\theta_{13} = 0.1$, $\sin^2 \theta_{23} = 0.5$, $\sin^2 2\theta_{12} = 0.84$, $\Delta m_{21}^2 = 7.5 \times 10^{-5}$ eV^2, $|\Delta m_{32}^2| = 2.4 \times 10^{-3}$ eV^2, $\delta_{CP} = 0$ deg.

Earth over long distances [109, 110, 111, 112, 113]. The differences in the oscillations probabilities of the neutrino and antineutrino, arising due to the matter effects, are crucial to determine the MH [114, 115] and have been illustrated in the following paragraph.

The baseline L in the case of the atmospheric neutrinos traveling through earth (i.e., the neutrinos reaching the ICAL detector from below) may vary from a few km to approximately $13,000$ km depending on its incident direction on the detector. The probabilities, being functions of L and E_ν, would thus vary in the $E_\nu - \theta_\nu$ plane. The parameter

$$\Delta P_{\mu\mu} = P_{\mu\mu}^{\text{NH}} - P_{\mu\mu}^{\text{IH}}, \tag{7.5}$$

would provide information on the potential of determining the mass hierarchy through the Earth matter effects. Fig. 7.2 shows the variation of $\Delta P_{\mu\mu}$ in the $E_\nu - \cos\theta_\nu$ plane for the neutrinos as well as the antineutrinos. It can be observed from the figure that the magnitude and sign of $\Delta P_{\mu\mu}$ fluctuates, which indicate the regions in the $E_\nu - \cos\theta_\nu$ plane which would contribute significantly to the mass hierarchy determination. A detector with good energy and zenith angle resolution would be

able to explore the regions with strong matter effects. Also, since the matter effects in neutrinos and the antineutrinos are complementary to each other, separate observation of these two would improve the scope of mass hierarchy identification, particularly for the experiments which would expect relatively low statistics.

7.2 THE HADRON CONTRIBUTION IN CC ν_μ EVENTS

As has been discussed in Chapter 2, the three main processes namely the quasi–elastic (QE), resonance scattering (RS) and deep inelastic scattering (DIS) contribute to the CC ν_μ interactions in the ICAL detector. The QE process, with no hadrons produced in the final state, dominates in the sub–GeV range. With an increase in the incident neutrino energy to multi–GeV range, the Hadronic showers start appearing in resonance (RS) and deep-inelastic scattering (DIS) processes. The final hadronic state in the RS process mostly consists of a single pion, though multiple pions may contribute in a small fraction of events.

(a)   (b)
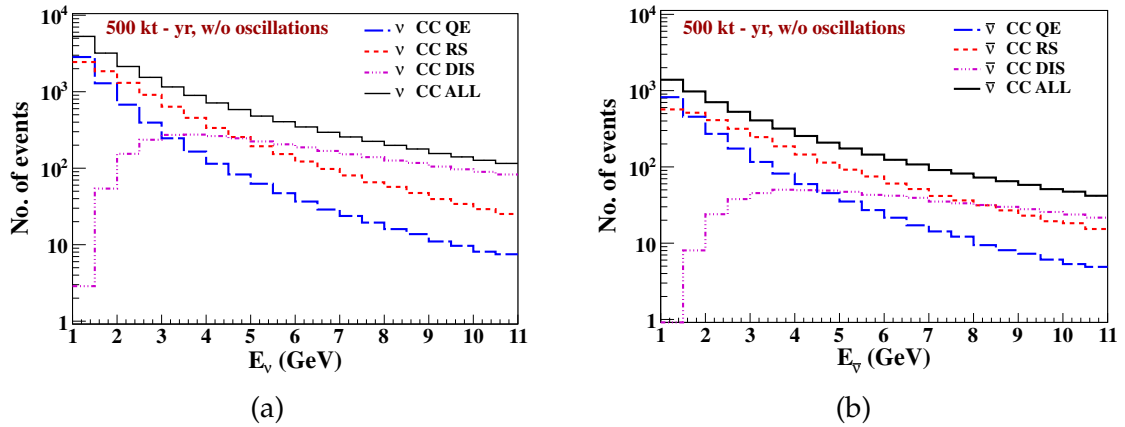
Figure 7.3: The number of (a) neutrino and (b) antineutrino events in ICAL, produced with QE, RS and DIS processes as functions of neutrino energy, with an exposure of 500 kt-yr, in the absence of oscillations. The total number of events is also shown. Note that this figure has been plotted with the event information at the generator level, without the detector response. [20]

In the DIS process, multiple hadrons are produced in the final state, which carry a large fraction of the incoming neutrino energy. Fig. 7.3 shows the relative contributions of these three processes to the total number of events in the absence of

oscillations, obtained using the event generator NUANCE, which have been used in the analysis presented in this chapter. In the neutrino energy range $5 - 10$ GeV, which is expected to have significant matter effects that will enhance the mass hierarchy identification, the contribution of DIS events is significant. Therefore, the information on hadrons produced in these DIS events is crucial.

(a)   (b)
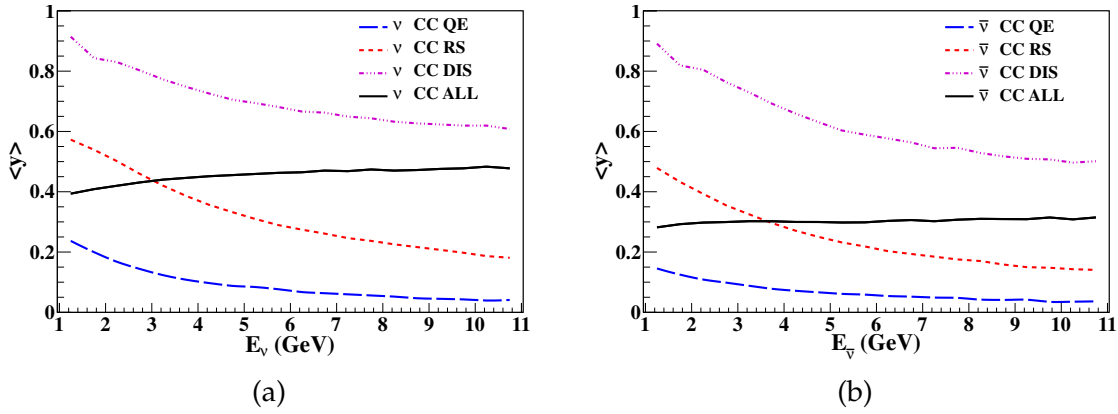
Figure 7.4: The average inelasticities $\langle y \rangle$, for (a) neutrinos and (b) antineutrinos, in QE, RS, DIS processes as a function of neutrino or antineutrino energies. The black line indicates the $\langle y \rangle$ for all processes combined. [20]

(a)   (b)
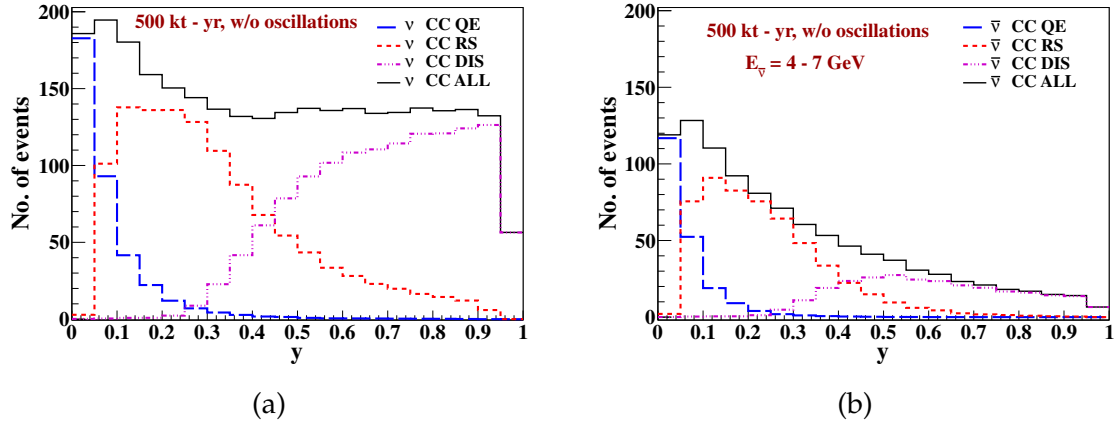
Figure 7.5: The distribution of inelasticity y in QE, RS and DIS events, for (a) neutrinos and (b) antineutrinos, with neutrino energies in the range $4 - 7$ GeV, with an exposure of 500 kt-yr, in the absence of oscillations. The distribution of y for all events combined is shown by the black histogram. [20]

The fraction of the neutrino energy that is carried by hadrons in an event can be indicated by the inelasticity, defined as $y \equiv (E_\nu - E_\mu)/E_\nu = E'_{\text{had}}/E_\nu$. In Fig. 7.4 the average inelasticities $\langle y \rangle$ in the three interaction processes are shown, separately for the neutrinos and the antineutrinos, as a function of the incident energy of the

neutrino/antineutrino. The significant $\langle y \rangle$ of the DIS events imply that a large fraction of the energy of the incoming neutrino goes to the hadrons in the energy range of interest for MH determination. Though the average inelasticity in this energy range does not fluctuate much, the inelasticities in individual events have a wide distribution as shown in Fig. 7.5 for a sample E_ν range ($4 - 7$ GeV). This implies the importance to treat the y values in individual events separately. Therefore, in this analysis the energies of hadrons and muons obtained in each event are treated separately, so that the correlation between them is not lost. A similar analysis has been done in [131], which shows significant enhancement. The procedure of the numerical analysis has been discussed in the next section.

7.3 THE ANALYSIS PROCEDURE

In this work, the oscillation analysis is carried out with the muon energy (E_μ), muon direction ($\cos\theta_\mu$), and the hadron energy ($E'_{\text{had}} = E_\nu - E_\mu$), in a neutrino interaction event as separate observables. Only the CC interaction events are used. It is assumed that the the reconstruction of the hadrons is 100% in an event where the muon is reconstructed. Thus the reconstruction and charge identification efficiency of the neutrino event are determined by the muon reconstruction. Also the muon and hadron hits are assumed to be separable with 100% efficiency. The lookup tables for the muon and hadron responses of the ICAL as given by the INO collaboration has been used. The background hits coming from other sources such as the NC events, CC ν_e events, cosmic muons, and the noise, have not been taken into account, ans assumed to be of marginal effect. Note that, at a magnetized iron neutrino detector (MIND) which is similar to ICAL, these background can be reduced to the level of about a per cent by using the cuts on track quality and kinematics [132].

The analysis procedure consists of various steps, like, the neutrino event generation, inclusion of the oscillation effects, incorporation of the detector response and the statistical analysis. These steps are described in the following subsections.

7.3.1 EVENT GENERATION AND THE INCLUSION OF OSCILLA-TIONS

Using the NUANCE event generator, ν_μ and $\bar{\nu}_\mu$ interaction events are generated, with the ICAL detector specifications given as input. The atmospheric neutrino fluxes were provided by HONDA et al [133]. for the Superkamiokande location. The differential cross sections for all the possible processes for both the charged-current (CC) and the neutral-current interactions, for all the nuclear constituents of the materials of ICAL is incorporated in NUANCE. The event rates for all scattering processes and possible target nuclei are calculated by multiplying the neutrino fluxes with the interaction cross sections. Event kinematics are generated based on the differential cross-sections. The total number of ν_μ events comes from the channels $\nu_\mu \to \nu_\mu$, and $\nu_e \to \nu_\mu$. For each event, the NUANCE output consists of the 4-momentum of the initial, intermediate and final state particles.

To reduce the Monte Carlo (MC) fluctuations in the event sample, interactions for an exposure of 1000 year $\times$ 50 kt are generated and scaled down to the various required exposures. Generation of such a large event-set for each set of oscillation parameters is very much time consuming and would have been practically impossible within a reasonable time frame. Therefore, we have generated one set of events for no oscillations and the oscillation effects are imposed by applying a re-weighting algorithm. In order to calculate the oscillation probability, the path traveled between the production point and the detector, for a given $\cos\theta_\nu$, is given by

$$L = \sqrt{(R + L_0)^2 - (R\sin\theta_\nu)^2} - R\cos\theta_\nu, \tag{7.6}$$

where R is the radius of the Earth (6378 km) and L_0 is the average height of the atmospheric neutrino production (~ 15 km). The re-weighting is then done by generating a random number between $0 - 1$ for each event and comparing it to the relevant oscillation probability [18].

7.3.2 INCORPORATION OF THE DETECTOR RESPONSE

The detector response (reconstruction and charge identification efficiencies and resolutions) are then incorporated upon the raw binned data one by one. First, the μ^- events (N_{μ^-}) after applying the reconstruction efficiency in a given (E'_{had}, E_μ, $\cos\theta_\mu$) bin is obtained by multiplying the true number of events with the corresponding reconstruction efficiency

$$N_{\mu^-}(E_\mu, \cos\theta_\mu, E'_{\text{had}}) = \epsilon_{R^-}(E_\mu, \cos\theta_\mu) \times N_{\mu^-}^{true}(E_\mu, \cos\theta_\mu, E'_{\text{had}}). \qquad (7.7)$$

Then the charge identification efficiency is applied as in the following.

$$N_{\mu^-}^C(E_\mu, \cos\theta_\mu, E'_{\text{had}}) = \epsilon_{C^-} \times N_{\mu^-}(E'_{had}, E_\mu, \cos\theta_\mu) + (1 - \epsilon_{C^+}) \times N_{\mu^+}(E_\mu, \cos\theta_\mu, E'_{\text{had}}),$$
$$(7.8)$$

where ϵ_{C^-} and ϵ_{C^+} are the CID efficiencies for μ^- and μ^+ respectively, and are functions of E_μ and $\cos\theta_\mu$.

Finally the muon energy and direction resolutions and the hadron energy resolution are applied as

$$(N_{\mu^-}^D)_{ijk} = \sum_l \sum_m \sum_n N_{\mu^-}^C(E_\mu^l, \cos\theta_\mu^m, E''^n_{\text{had}}) \; K_i^l(E_\mu^l) \; M_j^m(\cos\theta_\mu^m) \; N_k^n(E''^n_{\text{had}}), \quad (7.9)$$

where $(N_{\mu^-}^D)_{ijk}$ denotes the number of muon events in the ith E_μ – bin, the jth $\cos\theta_\mu$ – bin and k^{th} E'_{had} – bin, after applying the energy and angle resolutions. Here E_μ, $\cos\theta_\mu$ and E'_{had} are the measured muon energy, muon zenith angle and hadron energy respectively. The summation is over the true E_μ bin l, the true $\cos\theta_\mu$ bin m and true E'_{had} bin n, with E_μ^l, $\cos\theta_\mu^m$ and E''^n_{had} being the respective central values of the lth true E_μ bin, m^{th} true $\cos\theta_\mu$ bin and n^{th} true E'_{had} bin. The quantities K_i^l, M_j^m and N_k^n are the integrals of the detector resolution functions over the bins of the

measured values of E_μ, $\cos\theta$ and E'_{had}. They are calculated as

$$K_i^l(E_\mu^l) = \int_{E_{\mu L_i}}^{E_{\mu H_i}} dE_\mu \frac{1}{\sqrt{2\pi}\sigma_{E_\mu^l}} \exp\left(-\frac{(E_\mu^m - E)^2}{2\sigma_{E_\mu^m}^2}\right), \tag{7.10}$$

and

$$M_j^m(\cos\theta_\mu^m) = \int_{\cos\theta_{\mu L_j}}^{\cos\theta_{\mu H_j}} d\cos\theta_\mu \frac{1}{\sqrt{2\pi}\sigma_{\cos\theta_\mu^m}} \exp\left(-\frac{(\cos\theta_\mu^m - \cos\theta)^2}{2\sigma_{\cos\theta_\mu^m}^2}\right) \tag{7.11}$$

$$N_k^n(E'^n_{\text{had}}) = \int_{E'_{\text{had} L_k}}^{E'_{\text{had} H_k}} dE'_{\text{had}} \, P_{\text{Vavilov}}\left(P_0, P_1, P_2, P_3\right), \tag{7.12}$$

where $\sigma_{E_\mu^m}$ and $\sigma_{\cos\theta_\mu^n}$ are the resolutions of muon energy and zenith angle, respectively, in these bins. The P_{Vavilov} is the modified Vavilov probability distribution function, as defined in section 4.2.1, with the P_i ($i = 0, 1, 2, 3$) being the parameters which describe the reconstructed E'_{had} distributions. The integrations have been performed between the lower and upper boundaries of the measured values of the observables.

7.3.3 THE χ^2 ANALYSIS

The Poissonian definition of χ_-^2 for μ^- events as given below is used

$$\chi_-^2 = \min_{\xi_l} \sum_{i=1}^{N_{E'_{\text{had}}}} \sum_{j=1}^{N_{E_\mu}} \sum_{k=1}^{N_{\cos\theta_\mu}} \left[2(N_{ijk}^{\text{theory}} - N_{ijk}^{\text{data}}) - 2N_{ijk}^{\text{data}} \ln\left(\frac{N_{ijk}^{\text{theory}}}{N_{ijk}^{\text{data}}}\right)\right] + \sum_{l=1}^{5} \xi_l^2, \tag{7.13}$$

where

$$N_{ijk}^{\text{theory}} = N_{ijk}^0 \left(1 + \sum_{l=1}^{5} \pi_{ijk}^l \xi_l\right). \tag{7.14}$$

Here N_{ijk}^{theory} and N_{ijk}^{data} are the expected and observed number of μ^- events in a given $(E_\mu, \cos\theta_\mu, E'_{\text{had}})$ bin. N_{ijk}^0 are the number of events without systematic errors. Here N_{E_μ}, $N_{\cos\theta_\mu}$, and $N_{E'_{\text{had}}}$ are the number of bins in E_μ, $\cos\theta_\mu$ and E'_{had} respectively. To simulate N_{ijk}^{data}, the oscillation parameters as given in Table 7.1 are used as the *true*

values. These are benchmark values used in our analysis, and are consistent with those allowed by the global fit. The effective mass-squared difference is related to the Δm_{31}^2 and Δm_{21}^2 mass-squared differences through the expression [134, 135]

$$\Delta m_{eff}^2 = \Delta m_{31}^2 - \Delta m_{21}^2 (\cos^2 \theta_{12} - \cos \Delta_{cp} \sin \theta_{13} \sin 2\theta_{12} \tan \theta_{23}) . \qquad (7.15)$$

The following five systematic errors (ξ_l) are included in the analysis using the method of pulls: (i) Flux normalization error (20%), (ii) cross-section error (10%), (iii) tilt error (5%), (iv) zenith angle error (5%), and (v) overall systematics (5%). Here, π_{ijk}^l is the change in the number of events in the $(ijk)^{th}$ bin caused by varying the value of l th pull variable ξ_l by σ_l [26].

The χ_+^2 for μ^+ events is also obtained by using an identical procedure. The total χ^2 is obtained by adding the individual contributions from μ^- and μ^+ events. A prior of 8% (at 1σ) on $\sin^2 2\theta_{13}$ is added, since this quantity is currently known to this accuracy. No prior is added on θ_{23} or Δm_{32}^2 since these parameters will directly be measured at the ICAL detector. Thus

$$\chi_{ICAL}^2 = \chi_-^2 + \chi_+^2 + \chi_{prior}^2 , \qquad (7.16)$$

where

$$\chi_{prior}^2 \equiv \left(\frac{\sin^2 2\theta_{13} - \sin^2 2\theta_{13}(true)}{\sigma(\sin^2 2\theta_{13})} \right)^2 , \qquad (7.17)$$

and

$$\sigma(\sin^2 2\theta_{13}) = 0.08 \times \sin^2 2\theta_{13}(true). \qquad (7.18)$$

In the minimization procedure, χ_{ICAL}^2 is first minimized with respect to the pull variables ξ_l, and then marginalized over the ranges of oscillation parameters $\sin^2 \theta_{23}$, Δm_{eff}^2 and $\sin^2 2\theta_{13}$ as given in Table 7.1, wherever appropriate. We do not marginalize over δ_{CP}, Δm_{21}^2 and θ_{12} since they have negligible effects on the relevant oscillation probabilities at ICAL [136]. The best-fit values of Δm_{21}^2 and θ_{12} from the global

fit references [23, 24, 25] are used, while δ_{CP} is taken to be zero.

Table 7.1: Benchmark oscillation parameters used in this analysis. The true values of the oscillation parameters, are used to simulate the *observed* data set. The range, corresponding to the 3σ allowed values of the parameter in the global fit [23, 24, 25], over which the parameter values are varied while minimizing the χ^2 are also listed. Note that, while performing the analysis for precision measurements in Sec. 7.5, Δm_{eff}^2 or $\sin^2\theta_{23}$ are not marginalized, and $|\Delta m_{32}^2(\text{true})|$ is taken as 2.4×10^{-3} eV^2.

Parameter	True value	Marginalization range
$\sin^2 2\theta_{13}$	0.09, 0.1, 0.11	[0.07, 0.11]
$\sin^2 \theta_{23}$	0.4, 0.5, 0.6	[0.36, 0.66]
$\Delta m_{eff}^2/\text{eV}^2$	$\pm 2.4 \times 10^{-3}$	$[2.1, 2.6] \times 10^{-3}$ (NH)
		$-[2.6, 2.1] \times 10^{-3}$ (IH)
$\sin^2 2\theta_{12}$	0.84	Not marginalized
$\Delta m_{21}^2/\text{eV}^2$	7.5×10^{-5}	Not marginalized
Δ_{cp}	$0°$	Not marginalized

7.3.4 THE BINNING SCHEME IN $(E_\mu - \cos\theta_\mu - E'_{\mathrm{had}})$ SPACE

For an exposure of $500\,\mathrm{kt-yr}$ in ICAL, about 6200 events with a μ^- and 2800 events with a μ^+ are expected, after incorporating the reconstruction efficiencies and resolutions for muons and hadrons, in the absence of oscillations. With oscillations, these numbers would decrease further. For the analysis using the information on the muons only, i.e., in the $(E_\mu - \cos\theta_\mu)$ space, the excellent energy and angular resolutions of muon in ICAL [9, 19] make it possible to use a fine binning scheme. For example, the analysis presented in [18], 20 uniform E_μ bins in the range 1 to 11 GeV and 80 uniform $\cos\theta_\mu$ bins in the range $[-1, +1]$ were used for each polarity of muon. However, in such a fine scheme, a number of bins are left without a significant statistics. Including E'_{had} as an additional observable for binning would increase the total number of bins further, which would reduce the statistical strength of each bin significantly. In order to avoid such a situation, a coarser binning scheme that is suitable for the three observables E_μ, $\cos\theta_\mu$, and E'_{had} has been used in this

analysis. This scheme ensures that most of the bins have sufficient number of events, without affecting the results much.

An optimized binning scheme would depend on the parameters to be measured. In particular, it could be different for the mass hierarchy identification and precision measurements of atmospheric neutrino mixing parameters. For this analysis, the regions in the 3-dimensional parameter space ($E_\mu - \cos\theta_\mu - E'_{\text{had}}$) that are sensitive to the mass hierarchy has been identified, and finer bins of the three observables in those regions are used. These regions roughly span in E_μ = 4 to 7 GeV, $\cos\theta_\mu$ = -1 to -0.4, and E'_{had} = 0 to 4 GeV. In the rest of the observable space, a coarser binning has been used. The atmospheric neutrino flux follows a steep power law, resulting in a smaller number of events at higher muon and hadron energies. Therefore, in general, finer bins at low energies and wider bins at higher energies, for both muons and hadrons have been considered to ensure sufficient statistics in each bin. This is also consistent with larger uncertainties in energy measurement at higher energies. The binning scheme used is given in Table 7.2. For each polarity of muons, 10 bins for E_μ, 21 bins for $\cos\theta_\mu$, and 4 bins for E'_{had} are used, resulting into a total of ($4 \times 10 \times 21$) = 840 bins per polarity.

Table 7.2: The binning scheme for the reconstructed observables E_μ, $\cos\theta_\mu$, and E'_{had} for each muon polarity.

Observable	Range	Bin width	Total bins	
E_μ (GeV)	$[1, 4]$	0.5	6	
	$[4, 7]$	1	3	10
	$[7, 11]$	4	1	
$\cos\theta_\mu$	$[-1.0, -0.4]$	0.05	12	
	$[-0.4, 0.0]$	0.1	4	21
	$[0.0, 1.0]$	0.2	5	
E'_{had} (GeV)	$[0, 2]$	1	2	
	$[2, 4]$	2	1	4
	$[4, 15]$	11	1	

7.4   THE NEUTRINO MASS HIERARCHY IDENTIFI-CATION

In this section, the sensitivity of the ICAL detector in identifying the neutrino mass hierarchy (MH), as obtained from the analysis with the muons and the hadrons are presented. The statistical significance to rule out the wrong hierarchy is quantified by

$$\Delta\chi^2_{\text{ICAL}-\text{MH}} = \chi^2_{\text{ICAL}}(\text{false MH}) - \chi^2_{\text{ICAL}}(\text{true MH}). \qquad (7.19)$$

Here χ^2_{ICAL} (true MH) and χ^2_{ICAL} (false MH) are obtained by performing a fit to the *observed* data assuming true and false mass hierarchy, respectively. Here, with the statistical fluctuations suppressed, $\chi^2_{\text{ICAL}}(\text{true MH}) \approx 0$. The statistical significance is also represented in terms of $n\sigma$, where $n \equiv \sqrt{\chi^2_{\text{ICAL}-\text{MH}}}$. This represents the median sensitivity in the frequentist approach of hypothesis testing [137].

The inclusion of the hadron energy information in the analysis enhance the results significantly. In section 7.4.1, the extent to which the capability of the ICAL is improved with hadrons has been explored by studying the $\Delta\chi^2$, in the individual bins. The MH sensitivity results are then shown in section 7.4.2.

7.4.1   THE ENHANCEMENT IN THE BIN–BY–BIN χ^2 WITH HADRONS

In Fig. 7.6 the distribution of $\Delta\chi^2_{\pm} \equiv \chi^2_{\pm}(\text{IH}) - \chi^2_{\pm}(\text{NH})$ in the reconstructed $E_\mu - \cos\theta_\mu$ plane are shown. The left panels show the results for the analysis that does not use the hadron energy information. The right panels show the analysis where events are further divided into four sub-bins of E'_{had} and for each $E_\mu - \cos\theta_\mu$ bin, the $\Delta\chi^2_{\pm}$ has been summed over the hadron energy bins. Note that, the constant contribution in χ^2 coming from the term involving the five pull parameters ξ^2_l in Eq. (7.13) has not been considered. Also, the marginalization over the oscillation parameters in the fit has not been performed here. The final MH results shown in the coming section, the

full pull contributions and marginalizations have been taken care of.
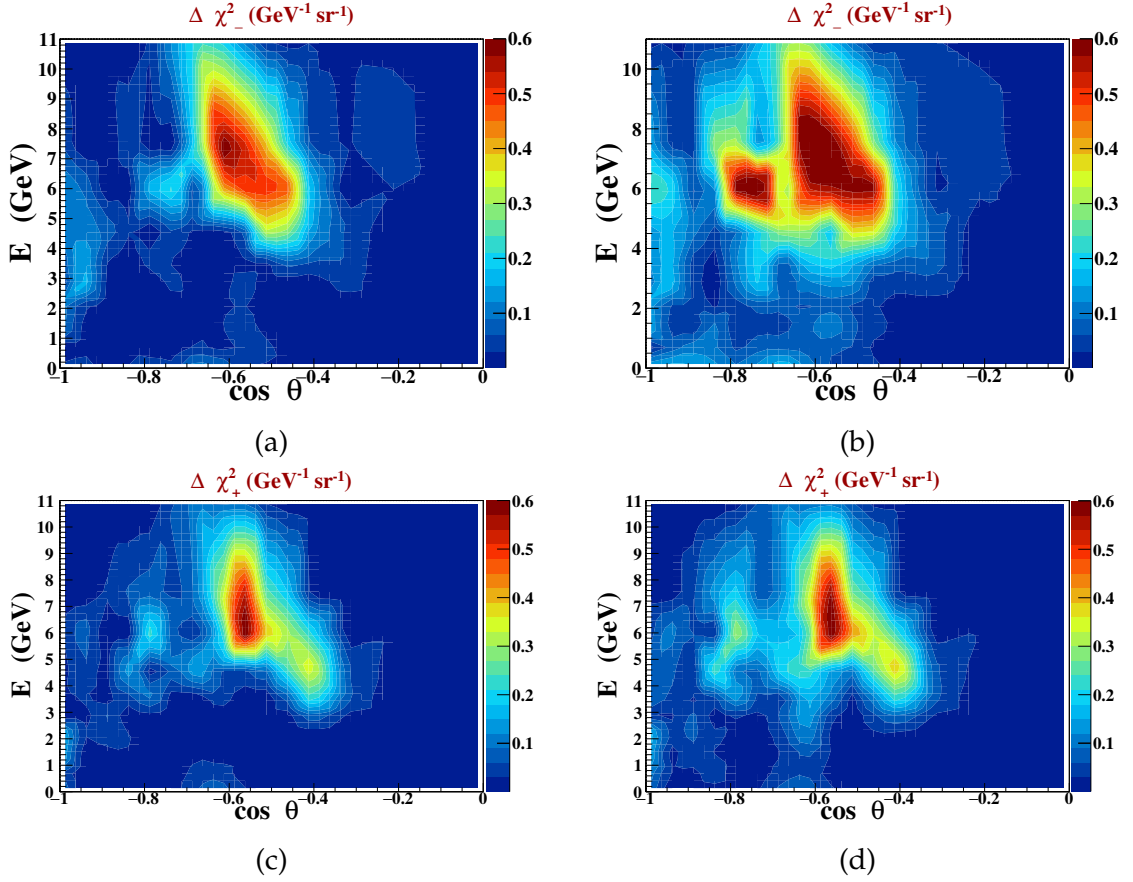
Figure 7.6: (Top) The distribution of $\Delta\chi^2_-$ per unit area, in the $(E_\mu - \cos\theta_\mu)$ plane, (a) without and (b) with hadron information. (Bottom) $\Delta\chi^2_+$ per unit area, (c) without and (d) with hadron information. Here, the NH is assumed to be the true hierarchy, and 500 kt-yr of ICAL exposure is used. [20]

The upper (lower) panels in Fig. 7.6 present the distribution of $\Delta\chi^2_-$ ($\Delta\chi^2_+$) arising from μ^- (μ^+) events. It can be observed that with the addition of the hadron energy information, the area in the $E_\mu - \cos\theta_\mu$ plane that contributes significantly to $\Delta\chi^2_\pm$ increases, which in turn improves the net $\Delta\chi^2_\pm$. This increase in $\chi^2_\pm$ is contributed by not only the information contained in the hadron energy measurement, but also the correlation between the hadron energy and muon momentum.

Another important fact to be noted is that the increase in the sensitivity is not simply due to the events with low E'_{had}, where the muon energy E_μ could be expected to closely match the original neutrino energy E_ν. This may be illustrated by Table 7.3, where, the total $\Delta\chi^2$ contributions from μ^- (μ^+) events for the four

individual hadron bins are shown.

Table 7.3: The contributions of various E'_{had}-bins to the net $\Delta\chi^2$. The events in the last row without E'_{had} information have true hadron energies up to 100 GeV.

E'_{had} (GeV)	events	$\Delta\chi^2$	$\Delta\chi^2$/events
0 - 1	3995	5.8	0.0014
1 - 2	1152	1.9	0.0017
2 - 4	742	1.7	0.0023
4 -15	677	1.2	0.0018
0 - 15 (with E'_{had} information)	6566	10.7	0.0016
without E'_{had} information	6775	6.3	0.0009

As can be seen from Table 7.3, while the $\Delta\chi^2$ contribution from the lowest E'_{had} bin is more than half the total $\Delta\chi^2$, this bin also has a large statistics. Indeed, the normalized $\Delta\chi^2$ per event is slightly higher for larger E'_{had} bins. This indicates that the hadron energy information from even the higher E'_{had} bins would be significant for identifying the true hierarchy.

7.4.2 THE MASS HIERARCHY SENSITIVITY OF ICAL

The sensitivity of 50 kt ICAL for identifying the neutrino mass hierarchy are shown in Fig. 7.7 as a function of the run–time of the experiment. It can be seen that after including the hadron energy information, 10 years of running can rule out the wrong hierarchy with $\chi^2_{\text{ICAL}-\text{MH}} \approx 9.7$ (for true NH), and $\chi^2_{\text{ICAL}-\text{MH}} \approx 9.1$ (for true IH). Thus, the sensitivity to discard the wrong hierarchy is about 3σ for either hierarchy. This figure also shows that for the same run-time the value of $\chi^2_{\text{ICAL}-\text{MH}}$ increases by about 40% when the correlated hadron energy information is added. Note that for comparison purpose, the same binning scheme in $(E_\mu, \cos\theta_\mu)$ has been used for both analyses, as shown in Table 7.2. As compared to the finer binning scheme in the muon–only analysis, as presented in [18], the improvement is about 35%.
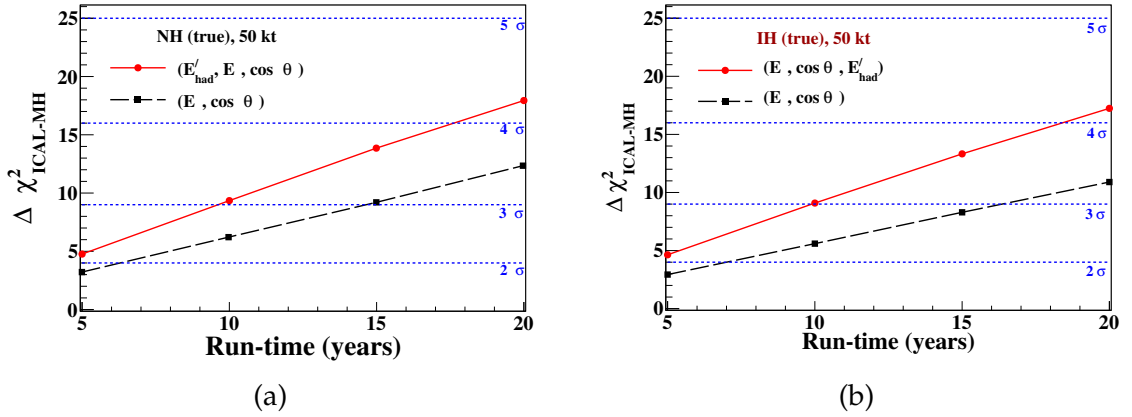
Figure 7.7: The $\chi^2_{\text{ICAL}-\text{MH}}$ as a function of the run-time assuming (a) NH and (b) IH as true hierarchy. The results obtained using hadron energy information is compared to the results from the analysis that is done without hadron information. Here, $\sin^2 2\theta_{13}(\text{true}) = 0.1$ and $\sin^2 \theta_{23}(\text{true}) = 0.5$. [20]
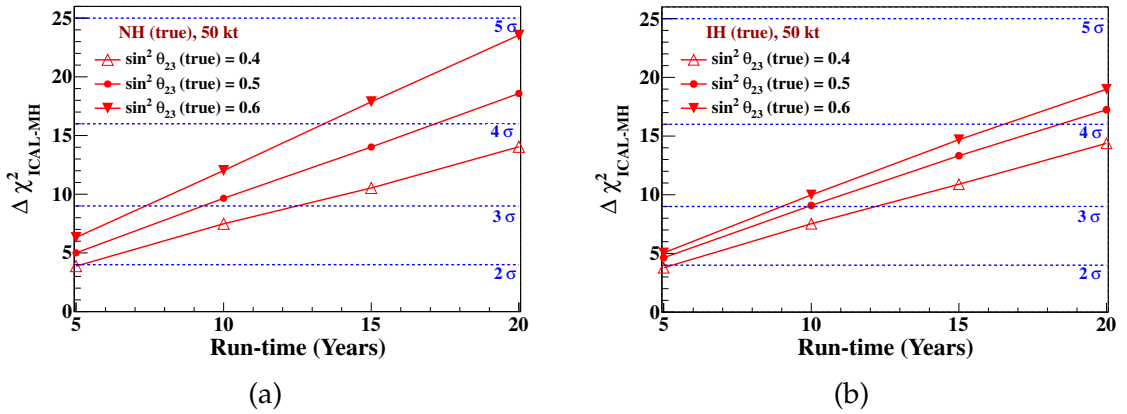
Figure 7.8: The variation of $\chi^2_{\text{ICAL}-\text{MH}}$ for different true values of $\sin^2 \theta_{23}$ assuming (a) NH and (b) IH as the true hierarchy. The value of $\sin^2 2\theta_{13}(\text{true})$ is taken to be 0.1.[20]

Fig. 7.8 and Fig. 7.9 show the variation of the MH identification sensitivity for three benchmark values of $\sin^2 \theta_{23}$ and $\sin^2 2\theta_{13}$, respectively, in the allowed ranges of these parameters. The higher values of these two parameters increase the matter effects in neutrino oscillations and thus, better hierarchy sensitivity is obtained. This is expected since the leading matter effect terms in the probability expressions of $P_{\mu\mu}$ and $P_{e\mu}$ are proportional to these parameters as shown in Eq. 7.1 and Eq. 7.2. Depending on the range of the true values of these parameters and the true choice of MH, the ICAL detector can identify the MH with a $\chi^2_{\text{ICAL}-\text{MH}}$ in the range of 7 – 12 for 10 years of running of the 50 kt ICAL.

(a) (b)
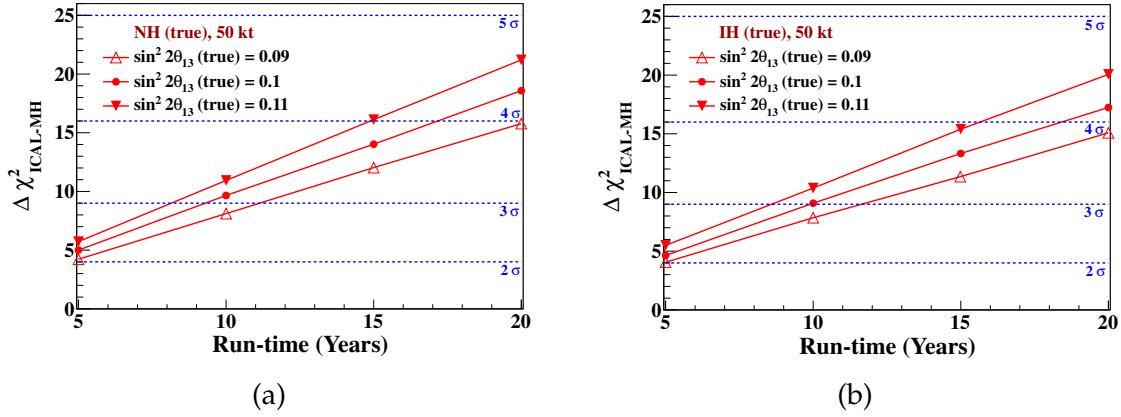
Figure 7.9: The variation of $\chi^2_{\mathrm{ICAL-MH}}$ for different true values of $\sin^2 2\theta_{13}$ assuming (a) NH and (b) IH as the true hierarchy. The value of $\sin^2 \theta_{23}(\mathrm{true})$ is 0.5. [20]

(a) (b)
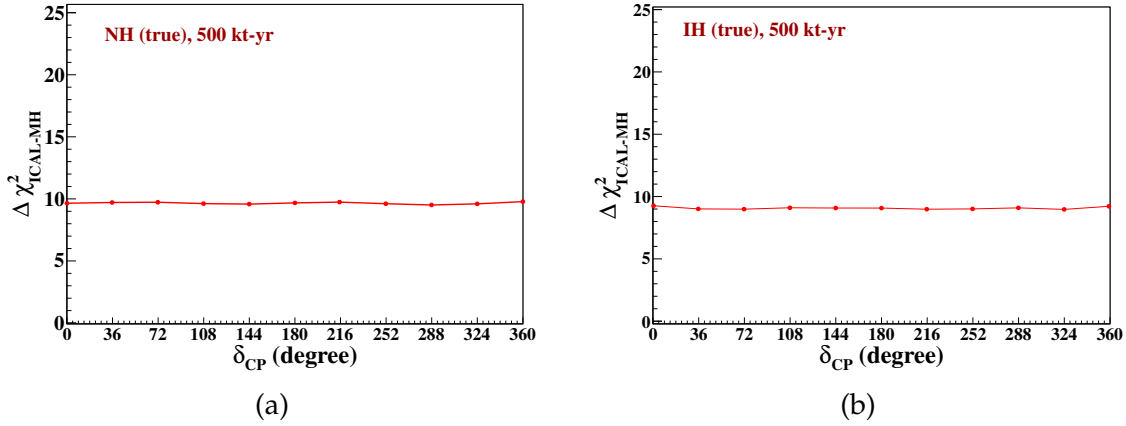
Figure 7.10: The variation of $\chi^2_{\mathrm{ICAL-MH}}$ with respect to δ_{CP}, assuming (a) NH and (b) IH as the true hierarchy, for an exposure of 500 kt–year at ICAL. Here, $\sin^2 \theta_{23}(\mathrm{true})$ is taken to be 0.5, and $\sin^2 2\theta_{13}(\mathrm{true})$ is taken to be 0.1.

Fig. 7.10 show the variation of $\chi^2_{\mathrm{ICAL-MH}}$ with respect to δ_{CP}. It can be seen that, the projected ICAL atmospheric data is not sensitive to δ_{CP}. This may be explained by the fact that in the full expression of $P_{\mu\mu}$, the δ_{CP} dependent term is suppressed by a factor of $\alpha \equiv \Delta m^2_{21}/\Delta m^2_{31}$ [136].

7.5 PRECISION MEASUREMENT OF THE ATMOSPHERIC PARAMETERS

The precision in the measurements of a parameter λ (where λ may be either $\sin^2 \theta_{23}$

or $|\Delta m_{32}^2|$) can be quantified in terms of the following.

$$\Delta\chi^2_{\mathrm{ICAL-PM}}(\lambda) = \chi^2_{\mathrm{ICAL-PM}}(\lambda) - \chi^2_0 , \tag{7.20}$$

where χ^2_0 is the minimum value of $\chi^2_{\mathrm{ICAL-PM}}$ in its allowed parameter range. Here, with the statistical fluctuations suppressed, $\chi^2_0 \approx 0$. The significance may be denoted by $n\sigma$ where $n \equiv \sqrt{\Delta\chi^2_{\mathrm{ICAL-PM}}}$. In terms of these quantities, the relative precision achieved on the parameter λ at 1σ is given by [138]

$$p(\lambda) = \frac{\lambda(\mathrm{max}) - \lambda(\mathrm{min})}{4\,\lambda(\mathrm{true})}, \tag{7.21}$$

where $\lambda(\mathrm{max})$ and $\lambda(\mathrm{min})$ are the maximum and minimum allowed values of λ at 2σ respectively, and $\lambda(\mathrm{true})$ is its true choice.
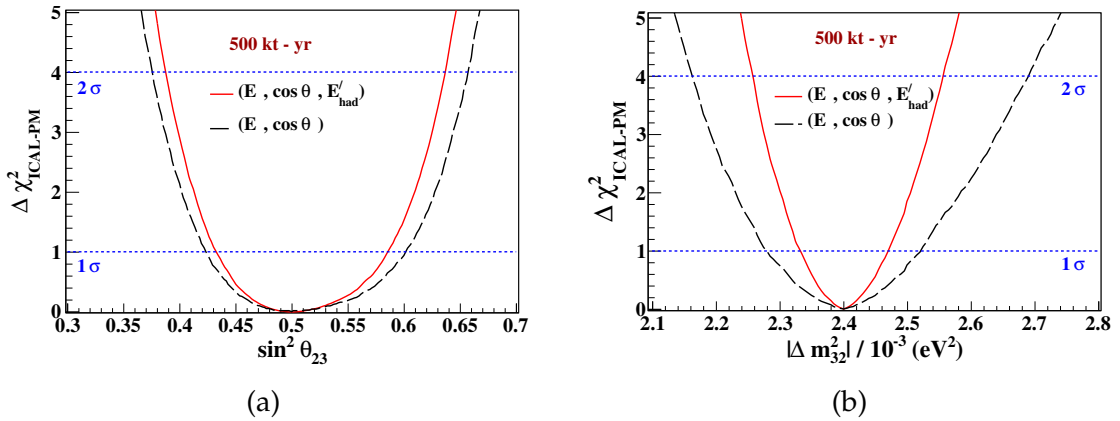
Figure 7.11: (a) The $\Delta\chi^2_{\mathrm{ICAL-PM}}(\sin^2\theta_{23})$ and (b) $\Delta\chi^2_{\mathrm{ICAL-PM}}(|\Delta m_{32}^2|)$, assuming NH as true hierarchy. The results obtained using hadron energy information is compared to the results from the analysis that is done without hadron information. [20]

In Fig. 7.11a and Fig. 7.11b the sensitivity of ICAL to the two parameters $\sin^2\theta_{23}$ and $|\Delta m_{32}^2|$ are shown separately, where the other parameter has been marginalized over. The parameter θ_{13} and the two possible choices of mass hierarchies have also been marginalized over. The figures show the results assuming NH to be the true hierarchy. It has been checked that, the results with true IH are almost identical. It may be observed from the figures that the inclusion of hadron energy information would make it possible to measure $\sin^2\theta_{23}$ to a relative 1σ precision of 12% and

$|\Delta m_{32}^2|$ to 2.9%, for 10 years of running of the ICAL. The muon-only analysis with the same binning scheme in E_μ and $\cos\theta_\mu$), the same relative precisions are obtained to be 13.7% and 5.4%, respectively. Note that, the muon-only analysis with finer binning (20 E_μ bins and 80 $\cos\theta_\mu$ bins) would yield the relative precisions in $\sin^2\theta_{23}$ and $|\Delta m_{32}^2|$ as, 13.5% and 4.2%, respectively,

The precision in $\sin^2\theta_{23}$ is governed mainly by the statistics available from the experiment. The addition of the hadron energy information does not change the statistics, and therefore makes only a small difference in the two analyses. However, the independent measurements of E_μ and E'_{had} corresponds to a better estimation of E_ν, which appears in the oscillation expression as $\sin^2(\Delta m^2 L/E_\nu)$. A better measurement of E_ν thus leads to a better measurement of Δm^2, resulting in the significant improvement in the precision on $|\Delta m_{32}^2|$.
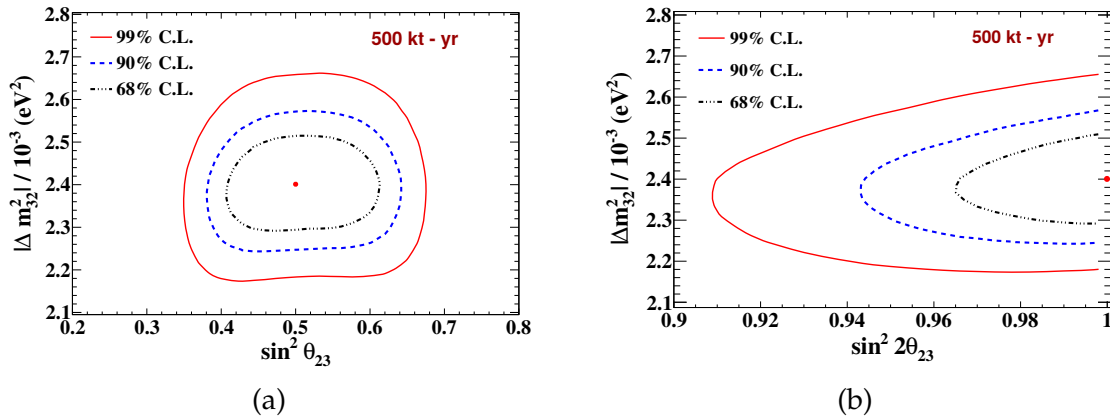
Figure 7.12: The $\Delta\chi^2_{\text{ICAL-PM}}$ contours at 68%, 90%, and 99% confidence levels (2 dof) in (a) $\sin^2\theta_{23} - |\Delta m_{32}^2|$ plane and (b) $\sin^2 2\theta_{23} - |\Delta m_{32}^2|$ plane , after including the hadron energy information. Here, NH is assumed as the true hierarchy. The true choices of the parameters have been marked with a dot. [20]

Fig. 7.12a and Fig. 7.12b show the $\Delta\chi^2_{\text{ICAL-PM}}$ contours at 68%, 90%, and 99% confidence levels in the $\sin^2\theta_{23} - |\Delta m_{32}^2|$ plane and in the $\sin^2 2\theta_{23} - |\Delta m_{32}^2|$ plane, respectively, with the inclusion of the hadron energy information. Here, the true value of θ_{23} has been taken to be maximal, so the contours in the left panel are almost symmetric in $\sin^2\theta_{23}$. The comparison of the projected 90% C.L. precision reach of ICAL (500 kt–yr exposure) in the $\sin^2\theta_{23} - |\Delta m_{32}^2|$ plane with other experiments is shown in
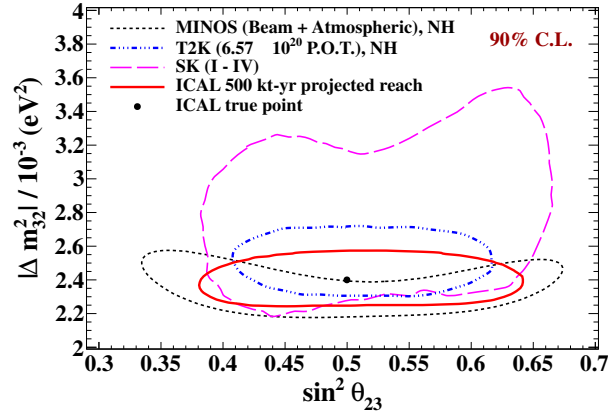
Figure 7.13: The comparison of the projected 90% C.L. precision reach of ICAL (500 kt-yr exposure) in the $\sin^2\theta_{23} - |\Delta m^2_{32}|$ plane with the results from SK [27], T2K [29] and MINOS [28] experiments. [20]

Fig. 7.13. Using hadron energy information, the ICAL will be able to achieve a precision in $\sin^2\theta_{23}$ which is comparable to the current precision for Super-Kamiokande [27] or T2K [29], and the $|\Delta m^2_{32}|$ precision comparable to the MINOS reach [28]. Note that, some of these experiments would have collected much more statistics by the time ICAL would have an exposure of 500 kt-yr. The ICAL will therefore not be competing with these experiments for the precision measurements of these mixing parameters, however the ICAL measurements will serve as complementary information for the global fit of world neutrino data. As compared to the atmospheric neutrino analysis at Super-Kamiokande, the ICAL precision on $|\Delta m^2_{32}|$ is far superior. This is a consequence of the better precision in the reconstruction of the muon momentum and direction at ICAL.

The 68%, 90%, and 99% C.L. contours in the $\sin^2\theta_{23} - |\Delta m^2_{32}|$ plane, for two non-maximal choices of the mixing angle θ_{23} ($= 0.37, 0.63$) are presented in Fig. 7.14. It can be seen that the precisions obtained are similar, though the shapes of the contours are more complicated. For θ_{23} in the lower octant, the maximal mixing can be ruled out with 99% C.L. with 500 kt-yr of ICAL data. However, if θ_{23} is closer to the maximal mixing value, or in the higher octant, then the ICAL sensitivity to exclude maximal mixing would be much smaller. These contours also motivate the attempt to resolve the θ_{23} octant degeneracy, which is discussed in the next section.
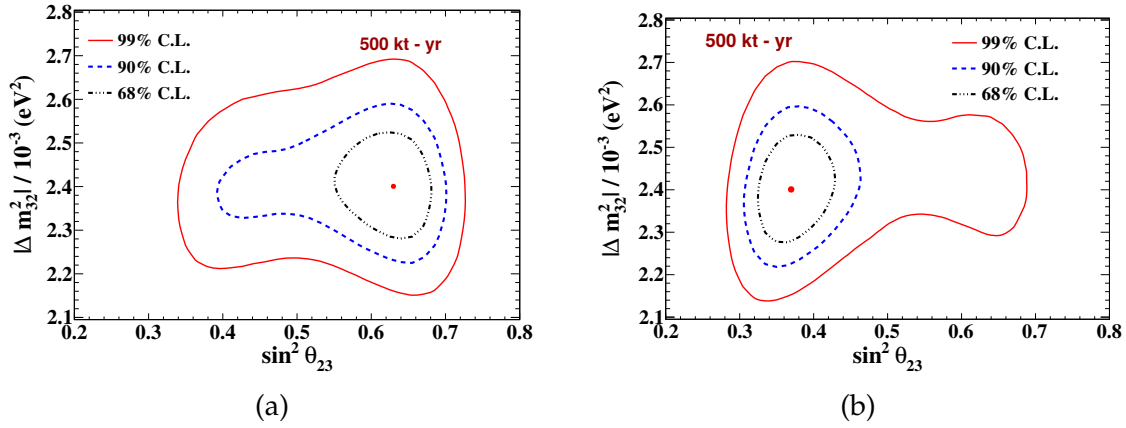
Figure 7.14: The $\Delta\chi^2_{\text{ICAL}-\text{PM}}$ contours at 68%, 90%, and 99% confidence levels (2 dof) in $\sin^2\theta_{23} - |\Delta m^2_{32}|$ plane, for (a) $\sin^2\theta_{23}$(true) = 0.37 and (b) $\sin^2\theta_{23}$(true)= 0.63, after including the hadron energy information. Here, NH is assumed to be the true hierarchy. The true choices of the parameters have been marked with a dot. [20]

7.6   OCTANT OF θ_{23}

The Earth matter effects in the $P_{\mu\mu}$ channel may be used to resolve the octant ambiguity of θ_{23} [139]. In analogy with the mass hierarchy discovery sensitivity of ICAL, the statistical significance of the analysis to rule out the wrong octant is quantified by

$$\Delta\chi^2_{\text{ICAL}-\text{OS}} = \chi^2_{\text{ICAL}}(\text{false octant}) - \chi^2_{\text{ICAL}}(\text{true octant}). \qquad (7.22)$$

Where χ^2_{ICAL}(true octant) and χ^2_{ICAL}(false octant) are obtained by performing a fit to the *observed* data assuming the true octant and wrong octant, respectively. Here with the statistical fluctuations suppressed, χ^2_{ICAL} (true octant) ≈ 0. For each given value of θ_{23}(true), θ_{23} has been marginalized over all the allowed values in the opposite octant, including the maximal mixing value. $\Delta\chi^2_{\text{ICAL}-\text{OS}}$ has also been marginalized over the true choices of mass hierarchy. The statistical significance for ruling out the wrong octant is represented in terms of $n\sigma$, where $n \equiv \sqrt{\Delta\chi^2_{\text{ICAL}-\text{OS}}}$.

Figure 7.15 shows the sensitivity of ICAL to the identification of the θ_{23} octant, with and without including the hadron energy information. This figure indicates the possibility of a 2σ identification of the octant with the 500 kt–yr ICAL data alone for NH as the true hierarchy and the lower octant to be the true octant. In this case,

without using the hadron energy information one can get a 2σ identification only when $\sin^2\theta_{23}$ (true) <0.375, which is almost close to the present 3σ bound. With the addition of hadron energy information, this task is possible as long as $\sin^2\theta_{23}$ (true) <0.395. If the higher octant is the true one, or the true mass hierarchy is inverted, then the discrimination of θ_{23} octant with the ICAL data alone becomes rather difficult. In case of NH (IH), neutrino (antineutrino) events are mostly affected by the Earth's matter effect and give crucial information about the octant of θ_{23}. Since the statistical strength of atmospheric neutrino events is higher compared to antineutrino events, the octant sensitivity is better for NH compared to IH. These observations are not much sensitive to the true value of θ_{13}. A variation of $\sin^2 2\theta_{13}$ (true) in the range $0.09 - 0.11$ changes the values of $\Delta\chi^2_{\text{ICAL-OS}}$ quite marginally. Clearly, the octant discrimination becomes more and more difficult as the true value of $\sin^2\theta_{23}$ moves close to the maximal mixing. Combining of the atmospheric and long–baseline experiments is, however, an effective approach, in which the ICAL contribution would also be significant [140, 141, 142].

(a)   (b)
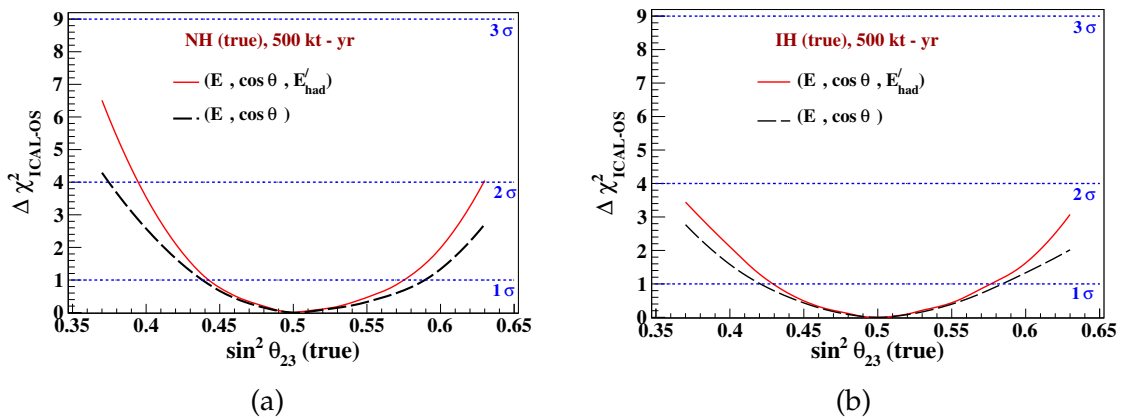
Figure 7.15: The $\Delta\chi^2_{\text{ICAL-OS}}$ for octant discovery potential as a function of true θ_{23} for (a) NH and (b) IH as true hierarchy, for the ICAL exposure of 500 kt–yr. The results obtained using hadron energy information is compared to the results from the analysis that is done without hadron information. [20]

7.7 REMARKS

In this chapter we have discussed the methodology and results of a statistical analysis which is used to assess the ICAL physics potentials with the inclusion of the hadron energy. Though ICAL is primarily optimized for muon detection, its capability of detecting hadrons and estimations their energy has been an additional advantage. The enhancement is not only due to the hadron energy, but also due to the correlation between the hadron energy and the muon momentum in an event. The analysis presented in this chapter uses hadron energy, muon energy and muon direction as separate observables in each event.

Significant improvements have been observed in the ICAL sensitivities, using this analysis. After including the E'_{had} information, 10 years of running can rule out the wrong hierarchy with $\Delta\chi^2_{\text{ICAL}-\text{MH}} \approx 9.5$ (for true NH), and $\Delta\chi^2_{\text{ICAL}-\text{MH}} \approx$ 8.7 (for true IH), which mark an improvement of about 40% over the muon-only analysis. It is observed that with the inclusion of E'_{had} information, 500 kt–yr of ICAL exposure would be able to measure $\sin^2\theta_{23}$ to a relative 1σ precision of 12% and $|\Delta m^2_{32}|$ to 2.9%. However, that the potential of distinguishing the θ_{23} octant with the ICAL data alone is rather weak. A 2σ identification of the octant is possible with the 500 kt–yr ICAL data alone only when, the true hierarchy is NH and the true octant is LO ($\sin^2\theta_{23}(\text{true}) < 0.395$).

Note that, due to the present status of understanding of the ICAL detector response as obtained from the simulations, certain assumptions had to be made in the course of this analysis. For example, it was assumed that the muon track and the hadron shower can be separated neatly in all events. The background hits and noise are neglected, and are assumed that they do not affect the hadron response of the detector. This analysis procedure is expected to be the preferred one for the ICAL physics reach. It is therefore crucial to look into the effects due to various assumptions. Also, improvement in the reconstruction of the observables would provide

further enhancement in this study. Various attempts on improving the reconstruction algorithms are being taken up.

The muon track reconstruction depends on the time information of the hits, to reconstruct the vertex. This also affects the hadron shower reconstruction, where the vertex information is used. One possible way of improving the time information is to use a detector with a better time resolution. In order to probe this as well as other applications, the Multigap RPC (MRPC) detectors [30, 31] have been developed. These detectors, due to the presence of a number of sub–gaps, are much faster than the RPC detectors. In Chapter 8, the development and performance of six–gap MRPC detectors, which achieve a time resolution of about 60 ps, will be discussed.

Chapter 8

DEVELOPMENT AND CHARACTERIZATION OF MRPC DETECTORS

The RPC detectors, which have a single gap for gas flow, have been chosen as the active detector elements for the magnetized Iron CALorimeter (ICAL) detector, due to their high efficiency, position and timing characteristics besides their long-term suitability for large detector coverage [6, 7]. The typical time resolution of the RPC detectors, to be used in ICAL, is in the range $1 - 1.5$ ns [120]. The muon track reconstruction uses the time information of the hits to determine the direction of the track, which is discussed in section 3.2 [9]. The time information of the hadron shower hits can also be used to determine their average direction (see Chapter 5). A detector with a better timing information would, therefore, improve the direction reconstruction of both muons and hadrons. A possible option may be the Multigap Resistive Plate Chamber (MRPC) detectors, which are the upgrades of the RPCs, with the introduction of multiple sub–gaps [30, 31]. The presence of multiple gas sub–gaps enable the detector to induce faster signals on the outer electrodes, thus

---

This chapter is based on [34], which has been submitted.

improving the detector's time resolution. Due to the excellent performance and relatively low cost, the MRPC detectors have found potential application in various Time–of–Flight (TOF) systems [143, 145, 144, 146].

The work described in this chapter involves the development and performance of single cell six–gap Glass MRPC detectors with each sub–gap being about 250 μm. These detectors have been developed to find application in the future upgradation of the ICAL detector, as well as TOF detector and other experiments. This chapter starts with an introduction to the MRPC detectors and their working principle. The fabrication procedure and the optimized design of the MRPCs, the experimental set–up including the trigger and data acquisition system and the MRPC characterization follow in the subsequent sections.

8.1 MRPC DETECTORS AND THEIR WORKING PRINCIPLE

The Multigap Resistive Plate Chambers (MRPCs) are gas ionization detectors with multiple gas sub–gaps made of highly resistive electrodes (glass in this case) having bulk resistivity of $10^{10} - 10^{12}$ Ω cm, spaced from one another using spacers of equal thickness. These detectors were conceptualized and first developed in 1996 [30, 31]. The high voltage (HV) is applied on the outer surfaces of outermost resistive plates to create a uniform and intense electric field across them, while the interior plates are left electrically floating. The external surface of the two outermost resistive plates are coated with a thin layer of graphite, in order to apply the high voltage uniformly. All the electrodes are kept apart by some spacers having a bulk resistivity greater than 10^{13} Ω cm. The narrower sub–gaps enhance their time resolution capability. Results from groups involved in the study of various MRPC configurations show that a time resolution of less than 100 ps can easily be obtained. MRPCs have been chosen as optimal elements for many Time–Of–Flight (TOF) de-

tector systems (including ALICE and STAR) due to their excellent time resolution and higher efficiency for particle detection. [143, 145, 144, 146]

The working principle, including the avalanche formation of an MRPC are similar to that of a single gap RPC, apart from the fact that, the additional sub–gaps make the signal collection faster. The internal plates would also allow the detector to withstand a higher operating voltage. The illustration of an ideal MRPC is shown in Fig. 8.1, where all the gas gaps are assumed to be of uniform width. The internal plates are electrically floating, and are maintained at equal voltages due to the flow of positive ions and electrons between them. The voltage across each sub–gap is the same. So, on an average, each sub–gap will produce the same number of avalanches when a flux of charged particles passes through it. This means the flow of electrons and ions into the plates bounding a gas gap will be identical for all the gaps, and the net charge to any of the internal plates would be zero. Avalanche in any of the sub–gaps induce the signals on the electrodes and it will travel very fast to the outermost electrodes, as the inner plates are transparent to the fast signals. The fast signals in case of MRPC are produced by the flow of electrons towards the anode. The resultant signal is the summation from all the gas gaps and it enhances the amplitude of the pulse. The surface resistivity of the conductive graphite coating is high enough so that the electrodes act as dielectrics, i.e., they are transparent to the fast signal generated by the avalanches inside each gas gap. The copper pickup strips placed outside the cathode and anode electrodes collect the signal, with a reduced time jitter, through induction.

A typical gas mixture, consisting largely of an electronegative gas and small fractions of the quenchers of UV photons and electrons, similar to those used for single gap RPC operation, may be used. Though the internal plates helps in quenching the streamers to avoid a spark breakdown, at higher operating voltages they are not sufficient, which leads to the use of the electron quencher gas in slightly higher fraction.
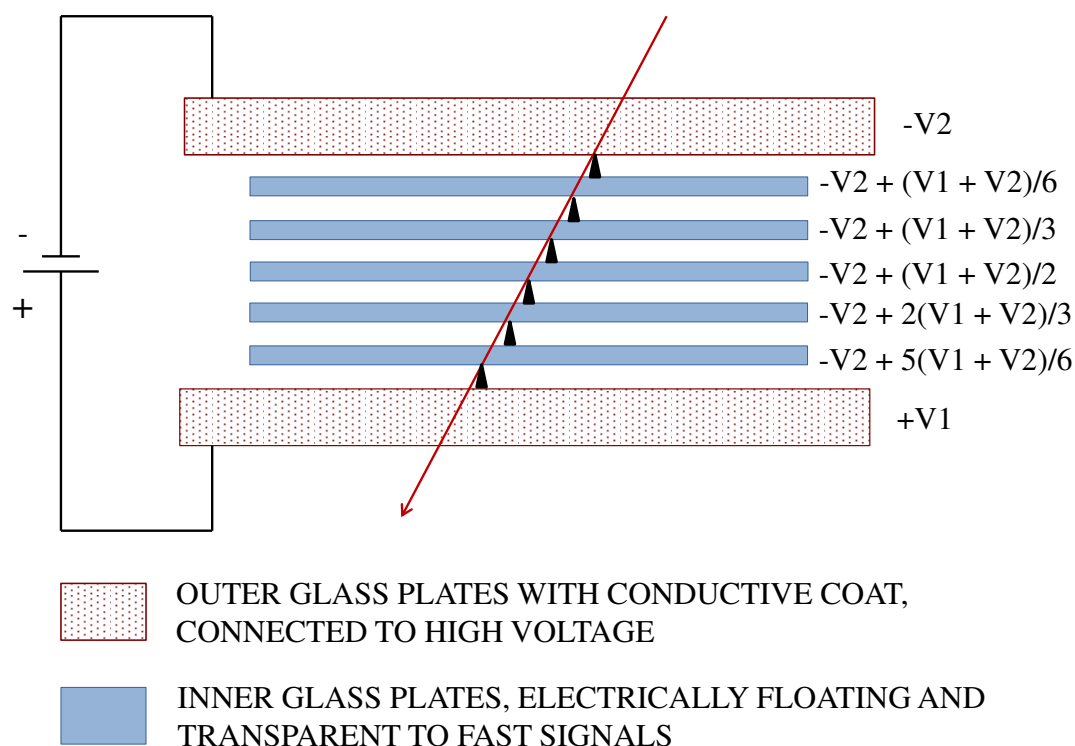
Figure 8.1: The illustration of an MRPC.

The intermediate plates also act as the physical barriers for the avalanche growing too big, and hence a higher electric field can be applied to the detector operated in the avalanche mode, compared to that of a single gap structure. This is advantageous in terms of the time resolution and rate capability of the device. The strong uniform electric field stimulates the avalanche process immediately after the primary ionization is created by a charged particle, leading to a very good time resolution.

The MRPCs may consist of a single stack with two external electrodes, or two stacks packed together with three external electrodes, the anode being common for both the stacks. Single cell (stack) configuration has a pair of external electrodes. As the number of floating electrodes increases, higher and higher operating voltage is needed to operate it. Double cell (stack) is basically two single cell MRPCs clamped together (usually the anodes). Bifurcating the floating electrodes in the two cells

helps in reducing the operating voltage at each of the electrodes.

8.2 DESIGN AND FABRICATION OF A 6–GAP MRPC

In this section the design and fabrication of six–gap glass MRPC detectors, with the single stack configuration, is discussed. We started with the fabrication of a six–gap MRPC with a small dimension (75 mm ×65 mm×7.67 mm), and later optimized the design to a larger dimension. The trial configurations, various problems encountered and the final optimized design are described in the following.

8.2.1 THE TRIAL CONFIGURATIONS

The first MRPC with six sub–gaps was of a dimension 70 mm ×60 mm ×7.67 mm. all the glass plates, including the two external ones were of the same thickness, i.e., 0.410 mm, and of the same area, i.e., 70 mm ×60 mm, as shown in Fig. 8.2a. Two sided non–conducting adhesive tapes of thickness 0.267 mm, cut in circular shapes of diameter 4 mm were used as spacers. Honeycomb panel with copper strips of width 1.4 cm were used to construct the pick up panel (five strips on each side). The whole set–up was sealed in an enclosure box of dimension 200 mm ×200 mm ×60 mm and gas was flown through it. The same gas mixture as mentioned in section 2.2, which is used in RPC detectors, was used. The gas flow rate was approximately 2.81 SCCM (i.e., Standard Cubic Centimeter per Minute) which corresponds to about 2 cycles a day.

However, this configuration gave rise to certain problems. The MRPC HV was slowly ramped up to 13 kV, where the chamber current was 25 nA. During this process, the MRPC broke down a few times, and a few sparks damaged the edges of a few inner plates, as shown in Fig. 8.2b. This problem appeared mainly due to the thin external electrodes which were unable to withstand such a high voltage. Also the edges of the interior plates were on the same line of the conductive coat on the two external electrodes. In order to solve this problem, the outer pair of conductive

(a)   (b)
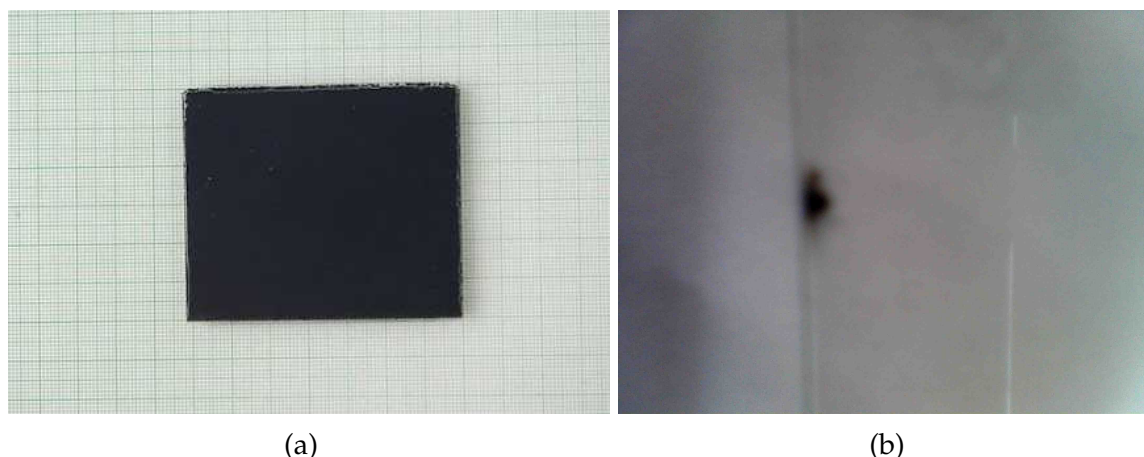
Figure 8.2: (a) The first six–gap configuration, which consisted of seven identical glass plates of thickness 0.410 mm. (b) The damage to the plates due to sparking.

electrode plates were replaced by plates of thickness 2 mm and slightly larger area (75 mm $\times 65$ mm). The graphite coating was confined to an area 58 mm $\times 58$ mm so that it remained well within the area of the interior plates. Fig. 8.3 shows various steps of the MRPC configuration. The new structure solved the issue of sparking.

The set–up was then tested with a trigger of two scintillator paddles in 2–fold coincidence, as shown in Fig. 8.4. A high voltage of 15 kV was applied across the two external glass plates of the MRPC. This detector, however, could detect only about 25% of the triggered events.

The next MRPC constructed was of a bigger dimension, 270 mm $\times 270$ mm $\times 7.58$ mm. The configuration, except the detector dimension, was similar to the previous MRPC. This detector was also enclosed in a chamber through which the gas mixture was flown. This detector too, was tested with a trigger formed by scintillator paddles in 2–fold coincidence, as shown in Fig. 8.5. A raw pulse, without any amplification, as detected in the detector is shown in Fig. 8.6

The strip efficiency is defined to be the ratio of the events detected by the MRPCs to the total triggered events. The strip efficiencies of the two MRPCs, as functions of the applied high voltage, are compared in Fig. 8.7. It can be seen that the larger MRPC attained an efficiency of about 80% at 15.9 kV.

(a)   (b)

(c)   (d)
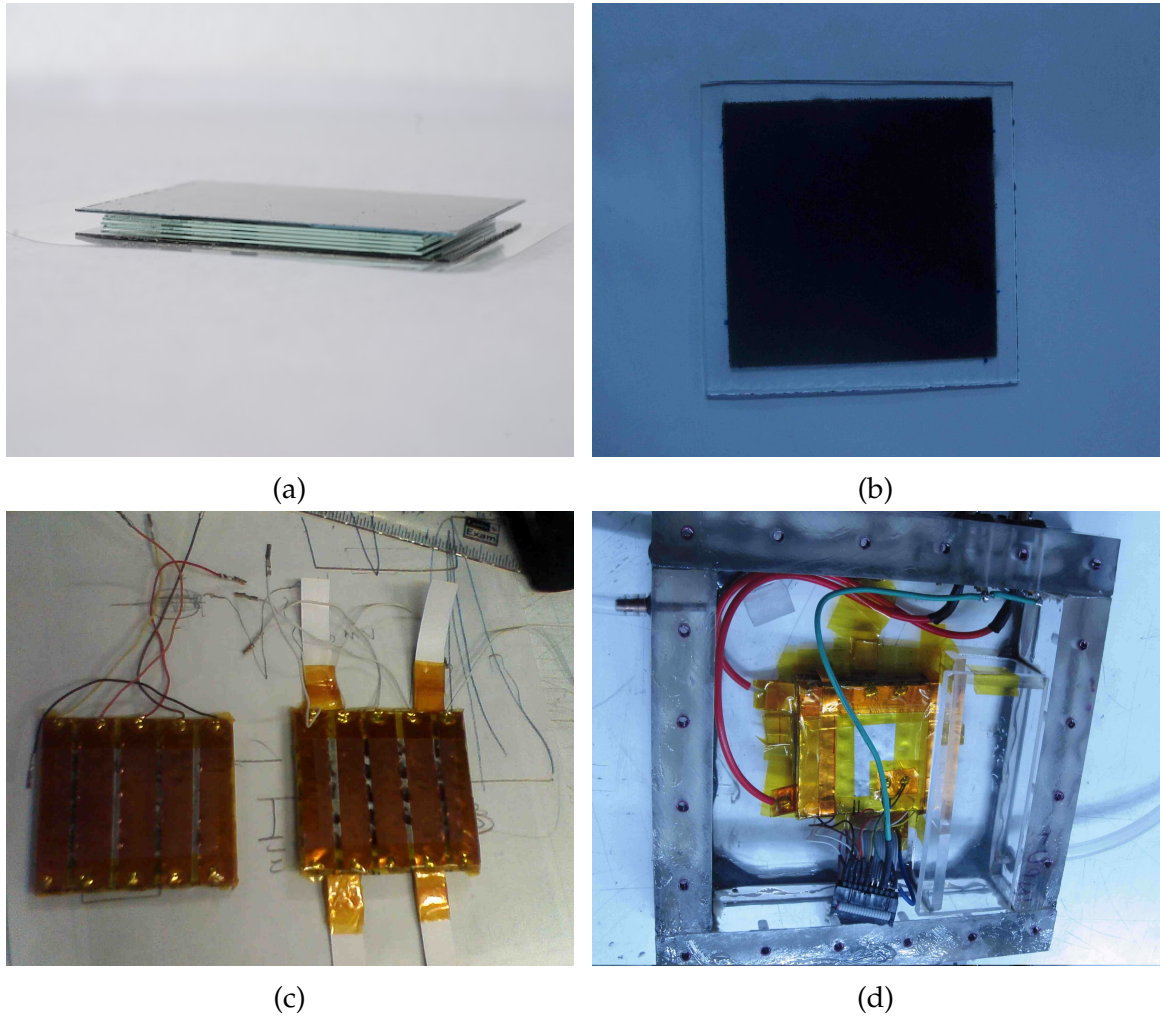
Figure 8.3: (a) The MRPC configuration to avoid sparking. The external plates are 2 mm thick, and larger than the internal plates. (b) The graphite coating on the exterior sides of the outer electrodes. (c) The honeycomb pickup panel. (d) The MRPC sealed in the enclosure.

As has been mentioned earlier, these two MRPCs were put in sealed enclosures through which the gas mixture was passed. This enclosed configuration made the alignment of the trigger consisting of the scintillator paddles difficult. Also, since the narrow sub–gaps would offer high resistances to the gas flow, compared to the rest of the enclosure, a complete uniform gas flow through all the gaps is not ensured. These difficulties have been taken care of in the fabrication of the next MRPCs. The optimized design of the six–gap MRPCs have been discussed in the following sub-section.
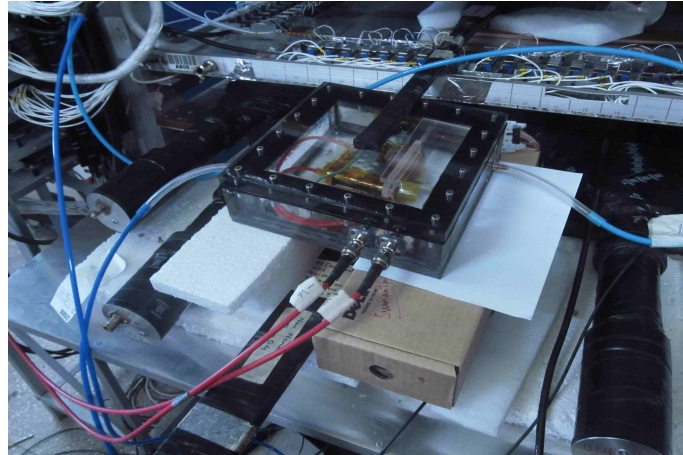
Figure 8.4: The set–up with the smaller MRPC. The trigger is a 2–fold coincidence with two scintillator paddles.
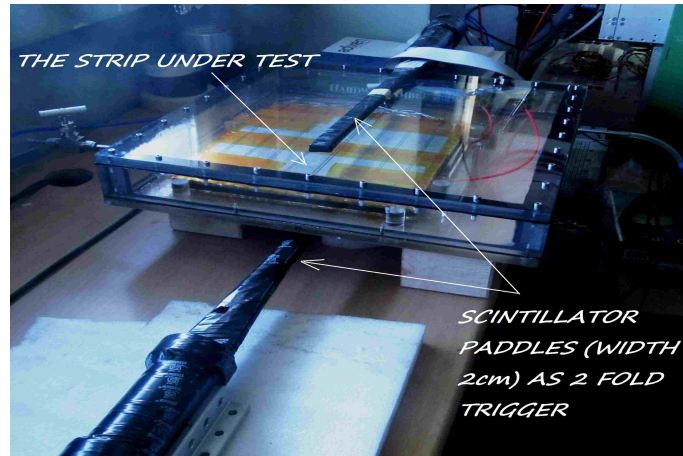
Figure 8.5: The set–up with the bigger MRPC. The trigger is a 2-fold coincidence with two scintillator paddles.

8.2.2 THE OPTIMIZED CONFIGURATION

The design of six–gap glass MRPCs with single cell structure of dimensions 305 mm $\times 305$ mm $\times 7.5$ mm has been optimized. A schematic of the configuration with dimensions of various components is shown in Fig 8.8. Note that the area of the internal glass plates are of dimension 256 mm $\times 256$ mm $\times 0.410$ mm.

Glasses of 2 mm thickness coated with a conductive layer using NEROLAC paint were used for the outer electrodes. The surface resistance of the conductive coat was in the range $(0.5 - 1)$ M$\Omega/\square$. Two sided non conducting adhesive tapes were stuck to both sides of a mylar sheet to make small circular spacers of diameter 4 mm and
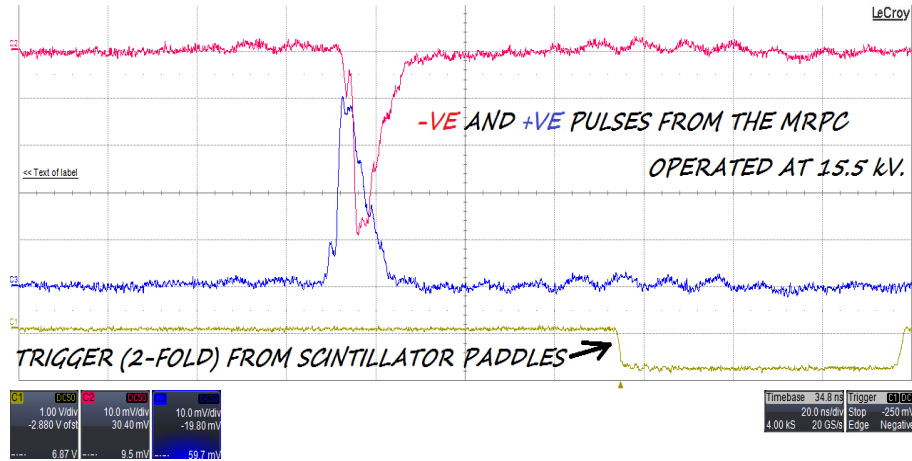
Figure 8.6: A raw pulse collected at both the anode and the cathode of the detector at an operating voltage of 15.5 kV. The trigger signal is also shown for reference.
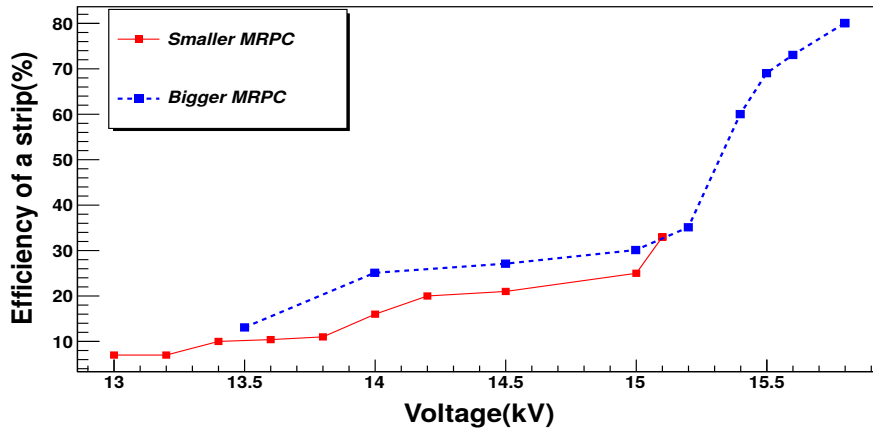
Figure 8.7: The strip efficiencies of the two MRPCs, as functions of the applied high voltage.

thickness 250 μm. Each gas gap were maintained by 25 such spacers. The placement of the spacers are shown in Fig. 8.9 (left panel). A few trials were first made by placing this configuration in an enclosed box filled with the gas mixture. Such an enclosed structure had some drawbacks like difficulty in alignment and the problem in ensuring sufficient and uniform gas flow through the sub–gaps. The configuration was optimized with sealing the gas gaps by gluing side spacers between the outermost electrodes. As can be seen from Fig. 8.8 and Fig. 8.9, there is a gap of about 2.7 cm from the edges of the external electrodes to the edges of the internal electrodes. There is a possibility of gas following that path instead of flowing through the sub–gaps which would offer high resistances. In order to ensure a proper flow through
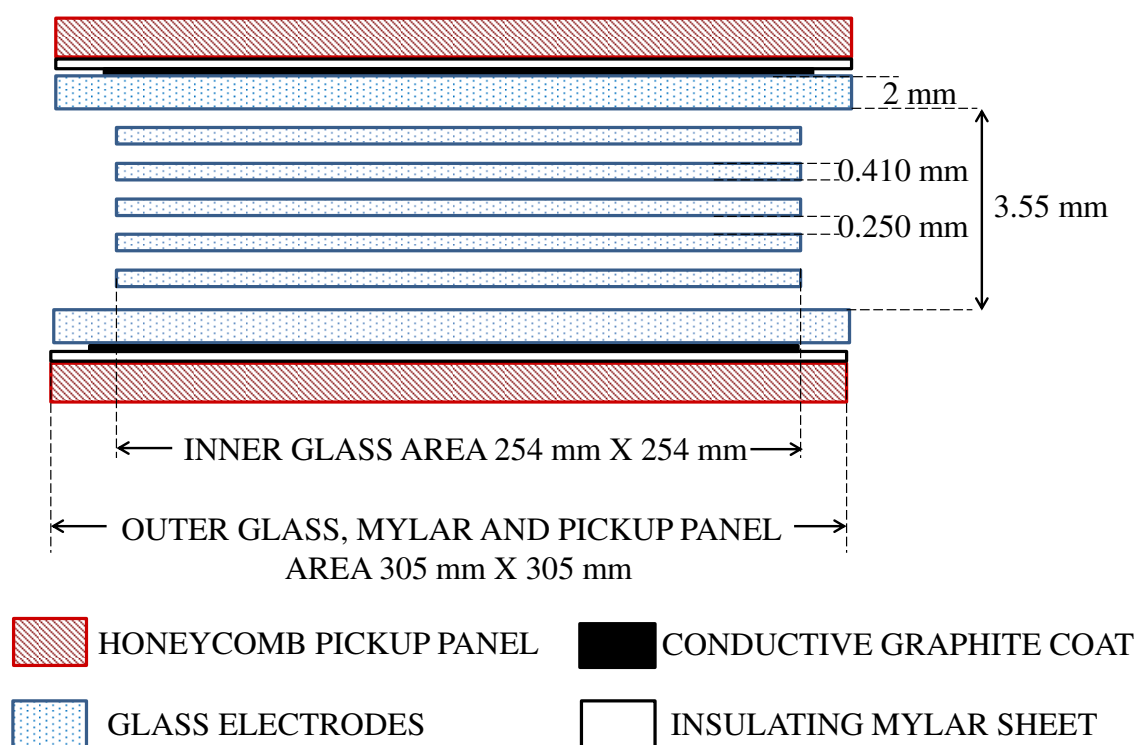
Figure 8.8: The schematic (with dimensions) of the optimized six–gap MRPCs.

the sub–gaps, we introduced some blockers at appropriate places (one each near the gas inlets and two each near the gas outlets). This is illustrated in Fig. 8.10. The pickup panel consists of honeycomb panels laminated with copper strips of width 2.8 cm. The pickup strips on both the sides of an MRPC were placed parallel to each other.
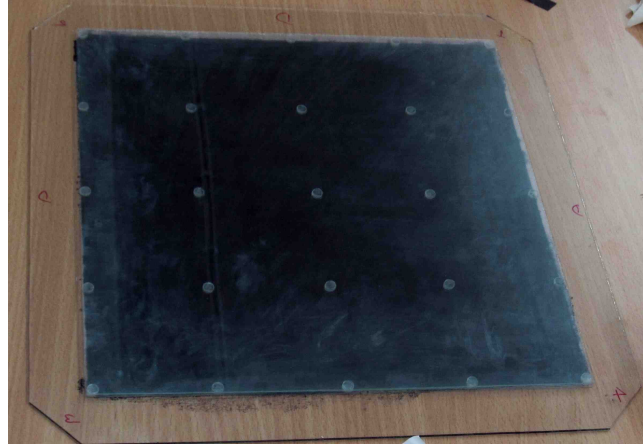
Figure 8.9: The placement of the spacers. There are 25 spacers in each sub–gap in a 5×5 array, the gap between any two consecutive spacers being 6.4 cm.
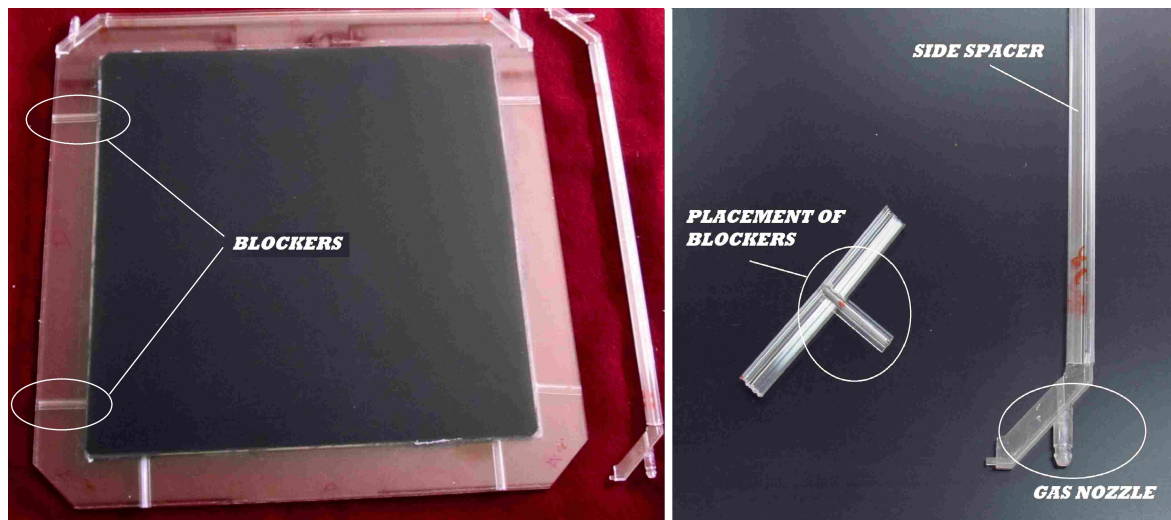
Figure 8.10: The placement of the blockers and side spacer. As shown in the left panel, two blockers are placed near each gas inlet while one blocker each are placed near each gas outlet, to ensure a proper gas flow through the sub gaps. The right panel shows a side spacer, fitted with a gas nozzle. A segment of a side spacer with a blocker attached is also shown.

8.3   THE EXPERIMENTAL SET–UP

The experimental set–up to test three MRPCs with the optimized design is described here. A cosmic muon telescope consisting of three scintillator paddles has been set up. The details of the telescope, the preamplifier and the data acquisition system are as in the following subsections.

8.3.1   THE COSMIC MUON TELESCOPE

The MRPCs are operated in avalanche mode and are characterized using cosmic muons. Three scintillator paddles of width 2 cm each (two on the top of the MRPCs under test and one at the bottom) were set up in a geometry to construct a cosmic ray muon telescope as illustrated in Fig. 8.11. Time coincidence of signals from these paddles indicates passage of a cosmic ray muon particle through the detector set–up. This coincidence signal has been used to trigger the data acquisition system. The set–up including three MRPCs and three scintillator paddles is shown in Fig. 8.12.

8.3.2   NINO ASIC

For amplification and digitization, NINO ASIC, an ultra fast front end preamplifier-discriminator chip which was developed for the ALICE TOF experiment, was used [33]. Each chip has 8 amplifier and discriminator channels. Each channel is designed with an amplifier with < 1 ns peaking time, a discriminator with a minimum detection threshold of 10 fC, and an output stage. As shown in Fig. 8.13, each channel in the NINO ASIC chip takes differential signals from the pickup strips as input, and amplifies them in a four–stage cascade amplifier.

With a 50 Ω termination across the pickup strips of the MRPCs, no signal was obtained using the NINO ASIC. Without a termination across the strips, the signals could be recorded, and for the rest of the study the strips were kept in *open* condition. The threshold to the discriminator stage of the chip was optimized to 157mV after

(a) LONG SIDE VIEW   (b) SHORT SIDE VIEW
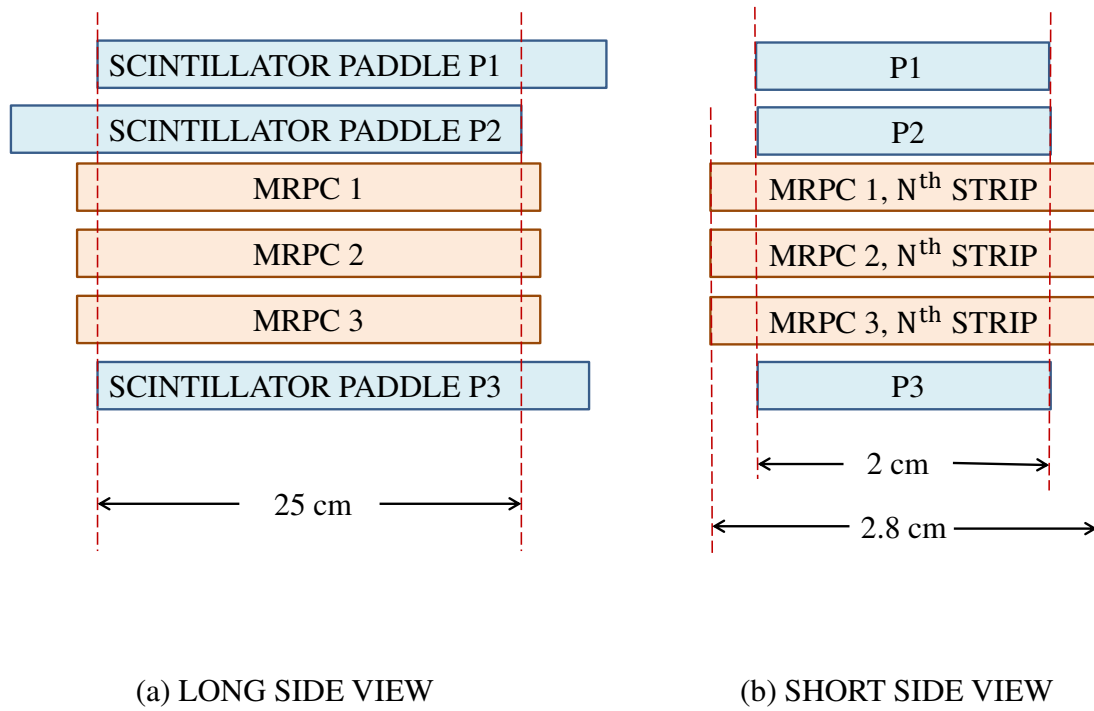
Figure 8.11: The scheme for the cosmic ray muon telescope. P1, P2 and P3 are scintillator paddles of width 2 cm each, and they are aligned on a pick-up strip of width 2.8 cm. The effective area of this telescope is 25 cm $\times 2$ cm.

studying counting rates of the detector at various values as summarized in Table 8.1.

Table 8.1: Counting rates of an MRPC strip at different NINO thresholds.

NINO thr. (mV)	Counting rate (kHz)	NINO thr. (mV)	Counting rate (kHz)
310.4	7.2	157	60
220.1	8	151	100
190.2	12	149	200
181.8	14	115.3	300

8.3.3 THE DATA ACQUISITION SYSTEM

A CAMAC based data acquisition (DAQ) system has been assembled for the MRPC detector test set–up. MRPC pickup strips are amplified and digitized by NINO ASIC and then taken with the time coincidence of the trigger. The differential (LVDS)
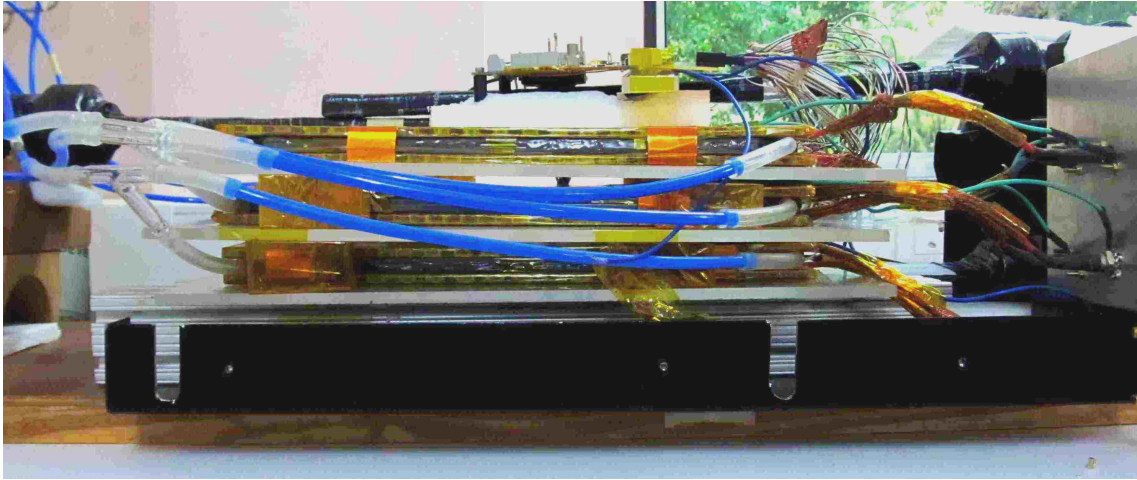
Figure 8.12: The experimental set–up.
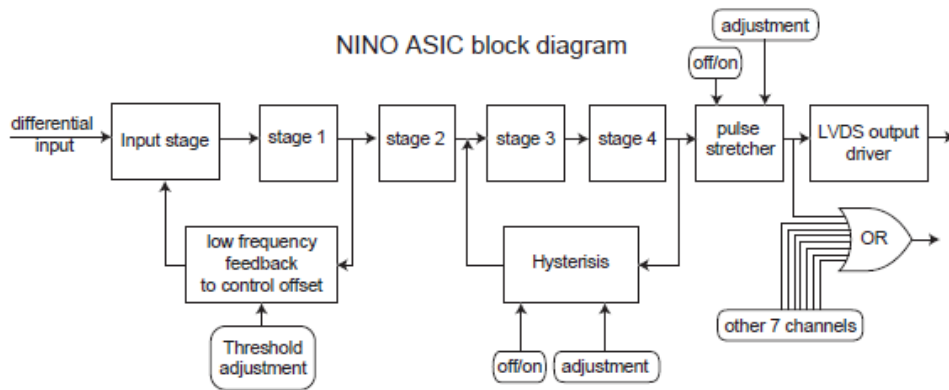
Figure 8.13: The schematic of the NINO ASIC [33].

signals obtained from NINO outout are converted to ECL and then according to the requirement of the scalar and TDC used directly or further converted to NIM signals. The counting rate of the individual strips are recorded with a ECL scalar. The trigger (T) is formed by putting the signals from the three scintillator paddles P1, P2 and P3 in coincidence mode. The efficiency of the MRPC strips are then obtained from the coincidence of the trigger and the strip count:

$$\text{Strip efficiency} = \frac{\text{MRPC strip count}}{T}.$$
(8.1)

The trigger is also given as the start signal to the TDC module to get the time count, where the stop signal comes from the MRPC strips. The DAQ scheme to obtain the

counting rate, efficiency and timing has been shown in Fig. 8.14.
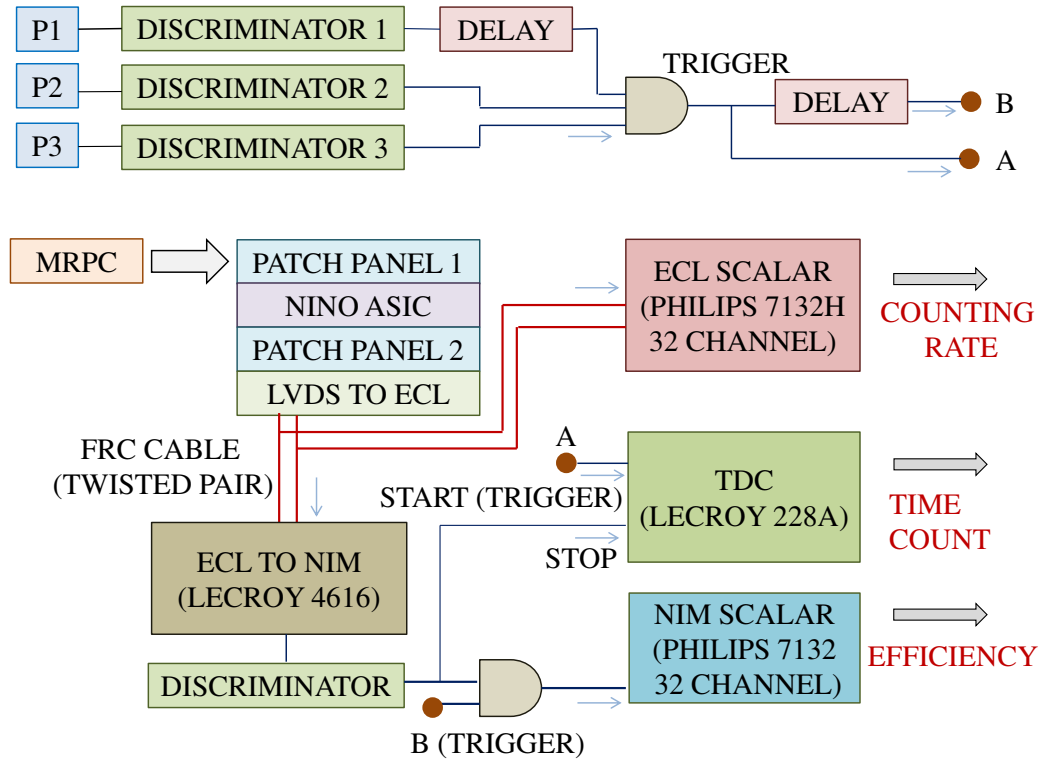
Figure 8.14: The DAQ scheme to obtain the strip counting rate, efficiency and time count.

8.4 THE MRPC PERFORMANCE

The characteristics of the MRPC detectors, obtained by adjusting various parameters like the gas mixture composition, HV etc., have been discussed here. The I–V characteristics, strip count rate, efficiency and the time resolution are discussed in the following.

8.4.1 MRPC CHARACTERIZATION AS A FUNCTION OF HV AND GAS MIXTURE

The gas mixture is composed of R134A, C_4H_{10} and SF_6. Studies showed that the MRPCs would be operated with around 5% of SF_6 [32, 148], unlike the standard
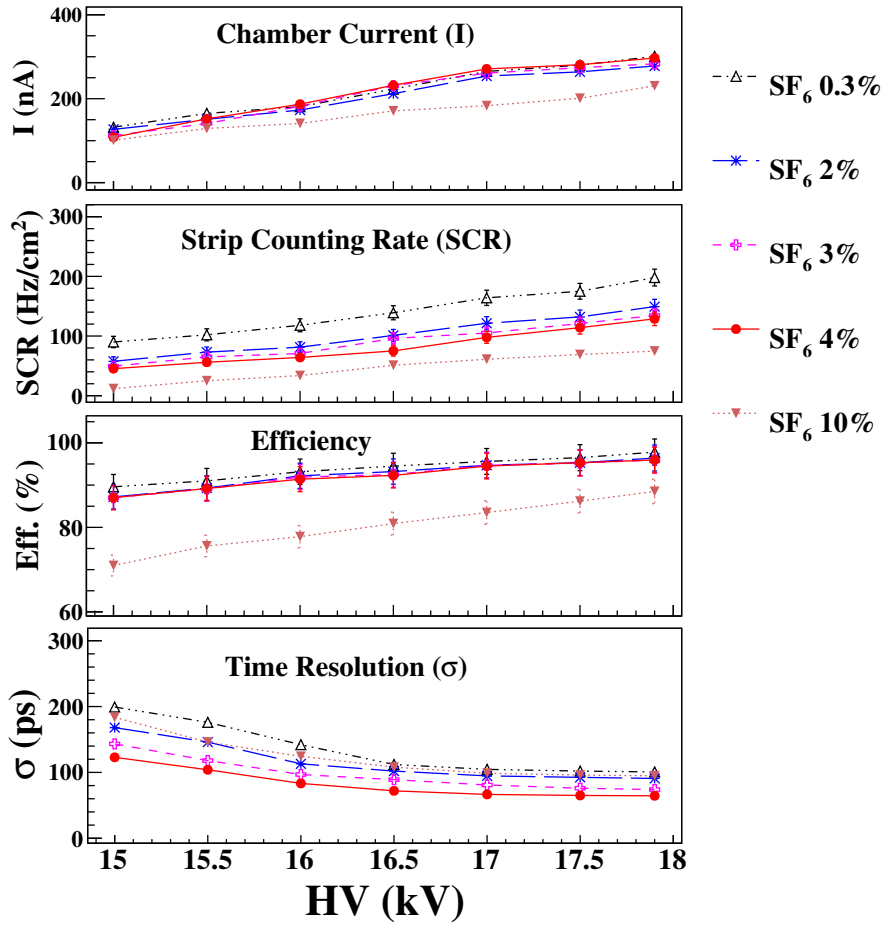
Figure 8.15: The characteristics of an MRPC strip as functions of the high voltage applied across the gas gap at different concentrations of the gas mixture of R134A, C_4H_10 and SF_6.

composition with very less amount of SF_6 ($\approx$ 0.3%) [7] that is used to operate single gap RPCs. With increasing SF_6 fraction, two competing processes affect the MRPC characteristics. Higher electric fields would be required with increasing fractions of SF_6, which would also increase the drift velocity and as a result improve the time resolution. On the contrary, since SF_6 has large capture cross–sections for low energy electrons, increasing the SF_6 concentration would reduce the avalanche significantly. This would degrade the MRPC counting rate, efficiency, time resolution etc. So, it is required to optimize the gas mixture for these two contradictory effects.

A study with various concentrations of SF_6 at different applied high voltages has also been performed to obtain an optimized set. For this, the proportion of

C_4H_{10} was kept fixed at 5%, and the other two were varied. Figure 8.15 shows the efficiency, counting rate per area of the pick-up strip, the chamber current and the time resolution of an MRPC strip. The operating HV was varied between $(15-17.9)$ kV. We see that at $\sim 4\%$ of SF_6, the time resolution is best and the noise rate and chamber current are reasonable without deteriorating the efficiency. So for further study, we have used the gas mixture of R134A (91%), C_4H_{10} (5%) and SF_6 (4%). We see that even at 17.9 kV the chamber current and counting rate do not shoot up too much. In Fig. 8.15, the time resolution after correcting from the time jitter has been shown. This correction is done via a calibration of the time count with the total charge deposited in an event. This has been described in the following.

8.4.2 TIME RESOLUTION

The introduction of smaller gas sub–gaps would result in an enhanced time resolution in MRPCs. For an accurate measurement of the timing, it is important to reduce any fluctuations which may occur during the generation of the timing logic signal. A major source of such fluctuations is the *walk* effect. This effect is caused by the variation in the signal amplitudes and/or rise time. The signals with different amplitudes would cross the discriminator threshold at different times, resulting in a time shift (walk) in the logic signal. An additional walk effect arises due to the finite amount of charge that is required to be integrated on a capacitor to trigger the discriminator. We reduce the time walk by calibrating the time counts with the charge deposited. Fig. 8.16 shows a typical raw time distribution (before correcting for the time walk). Here the trigger is provided by the scintillator paddles in coincidence, as have been described in section 8.3.1, and this has been used as the start to the TDC. We have corrected the time distributions for the time walk according to the charge of the signal. Note that, the charge is obtained from the analog output signal from the MRPC strips. Since NINO ASIC provides LVDS output only, for this study it has been replaced with ANUSPARSH, the ASIC designed for the ICAL experiment.

A scatter plot of time vs charge is shown in Fig. 8.17. This is fitted to a function $\exp[-a_0/x + a_1] + a_2$. The time of each event is then corrected according to the charge information by employing a calibration through the fit parameters. Fig. 8.18 shows the comparison of raw and corrected time distributions at 17.9 kV and with the optimized gas mixture.
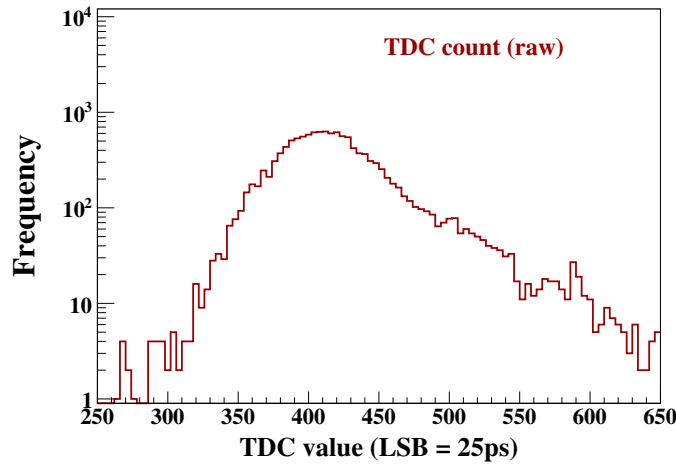
Figure 8.16: The raw MRPC time distribution with respect to the trigger at 17.9 kV and with the gas mixture R134A (91%), C_4H_{10} (5%) and SF_6 (4%).
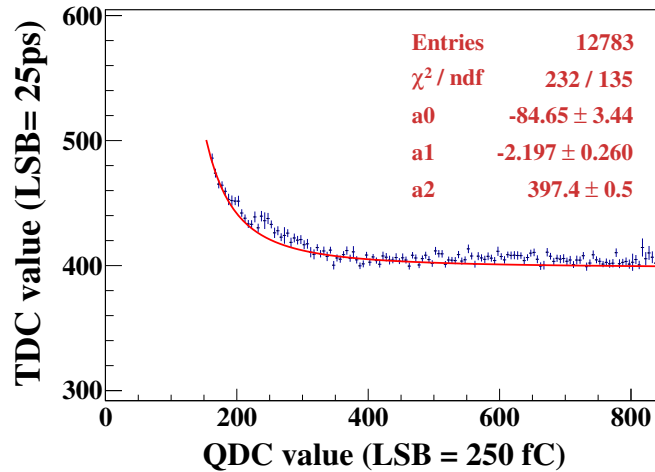
Figure 8.17: The calibration graph for correcting of the MRPC time distribution for time-walk, fitted to $\exp[-a_0/x + a_1] + a_2$.

As shown in Fig. 8.18, at 17.9 kV, the time resolution is ~ 60 ps, which also includes $15 - 25$ ps of jitter due to electronic channels. This jitter has been estimated by replacing the MRPC strip signals with a pulser and observing the obtained time
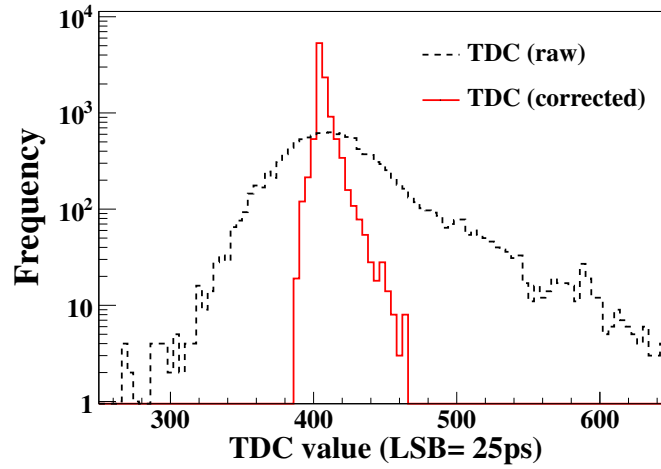
Figure 8.18: The MRPC time distribution with respect to the trigger at 17.9 kV and with the gas mixture R134A (91%), C_4H_{10} (5%) and SF_6 (4%). The black line shows the raw distribution, while the red one shows the distribution after applying the time walk correction.

count.

8.4.3   STUDY USING Cs-137 SOURCE

Earlier a cosmic muon telescope was employed to study the characteristics of the MRPC. Since the cosmic muon flux is scattered over θ and ϕ, so the paddles and the MRPC strip are hit from muons in a wide cone, and also at various points of the strip, which may deteriorate the time resolution, in particular. To verify that, a Cs–137 source of strength 3×10^6 dps has also been used. In Fig. 8.19 the efficiency and time resolution as functions of the high voltage are shown.

8.4.4   MRPC AS A PART OF TRIGGER

One of the potential timing applications of MRPC is then probed by adding it to the external trigger system for a single–gap RPC. In Fig. 8.20 the three different set–ups are shown. The various characteristics of the single-gap RPC from these three trigger set–ups are listed in Table 8.2. It can be seen that the introduction of the MRPC in the trigger system helps in improving the time resolution.
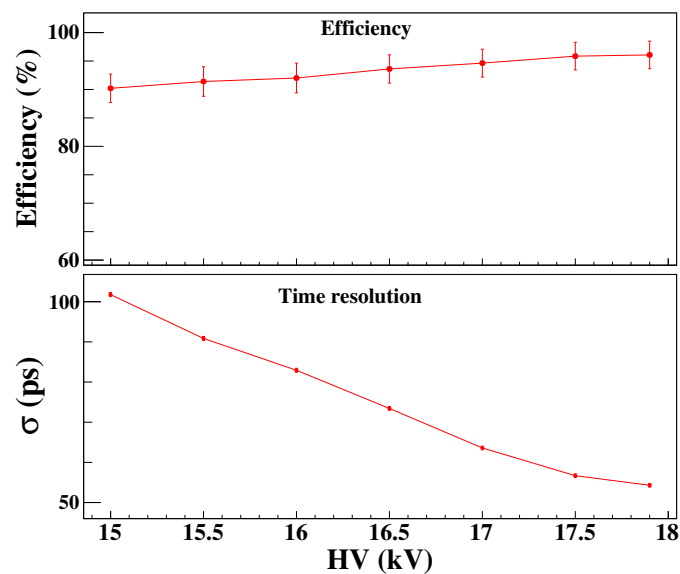
Figure 8.19: The efficiency and time resolution of the MRPC with a Cs-137 source, as functions of high voltage.

(a) SET-UP I   (b) SET-UP II   (c) SET-UP III
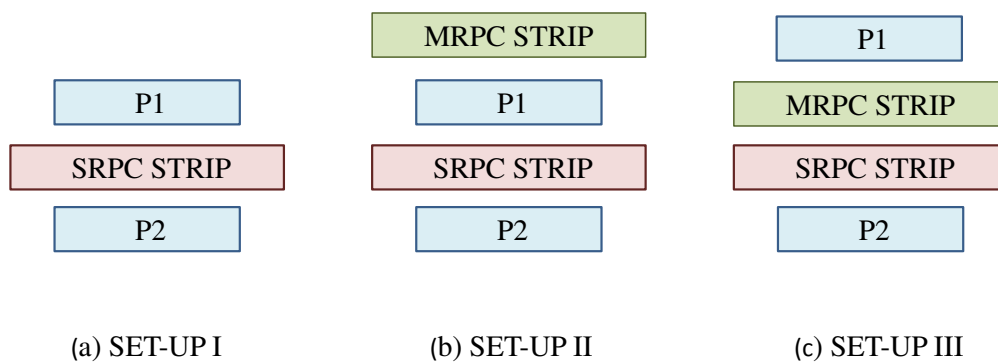
Figure 8.20: The three set–ups under study. Set–up I consists only the scintillator paddles P1 and P2 in coincidence to form the trigger. The other two set–ups use an MRPC in addition to the paddles.

Table 8.2: The MRPC characteristics for different trigger set–up.

Set–up	Trigger	Eff.(%)	Time res.(ns)	Noise($\frac{Hz}{cm^2}$)	I(nA)
I	P1, P2	85	1.42	1.5	305
II	P1, P2, MRPC	85.9	0.87	2.85	312
III	P1, P2, MRPC	87.8	0.85	1.87	311

8.5 REMARKS

This chapter describes the design of the MRPCs with six sub–gaps and the optimization of the single stacked configuration. The detectors are characterized with a cosmic telescope set–up and their characteristics have been studied. The parameters like the applied voltage, the gas mixture are also been optimized. The detectors are now being operated in a stable condition, with the strip efficiency being about 95% and the time resolution being $60 - 100$ ps, and the stack is ready for the further study to assess its potential for various applications. It has already shown promising result when used as the part of a trigger set–up. Now, the stack is being planned to be used for a TOF measurement study which, however, is beyond the scope of this thesis.

Chapter 9

SUMMARY AND FUTURE SCOPE

The work on the simulation of the hadron response of the ICAL detector and their contribution to the enhancement in the ICAL sensitivity to the neutrino oscillation study, and the development of the multigap RPC detectors which may be probed to further enhance the reconstruction of the muon and the hadrons in the ICAL; which have been discussed in the preeceding chapters, have been summarized here. The future scopes to improve this work have also been highlighted.

9.1   SUMMARY

The INO collaboration plans to study the neutrino oscillations in the atmospheric sector, with a 50 kt magnetized ICAL detector. The R&D program for the ICAL is now running at a full pace. This detector is primarily designed to measure the muon momentum. The magnetic field would also allow us to distinguish between the muon and the antimuon, and hence between the incident neutrino and the antineutrino.

The main aim of the detector is to identify the true mass hierarchy, through the study of the Earth matter effects experienced by the neutrinos and the antineutrinos, separately. Apart from that, ICAL would also contribute in the precise measurement of the atmospheric neutrino parameters $|\Delta m_{32}^2|$, θ_{23} and its octant. The ICAL would also look for the hint of any new physics. Apart from the muons, ICAL is also ca-

pable of detecting the hadron shower and measure its momentum. The information on the hadrons provides an additional boost to the physics potential of ICAL.

A simulation study has been performed to quantify the detector response to the muons and hadrons produced in the atmospheric muon neutrino interactions. The muon leaves a long track in the detector, and its momentum and direction is obtained through a track reconstruction algorithm based on the Kalman Filter techniques. However, the hadrons produce a shower of hits within a close proximity of the interaction vertex. The hadron energy, parametrized in terms of $E'_{\mathrm{had}} \equiv E_\nu - E_\mu$, is estimated from the hadron hit multiplicity which follows the Vavilov PDF. A calibration of E'_{had} for the number of hadron hits in an event has also been obtained. The hadron energy resolution of ICAL is in the range $(80\% - 35\%)$ for E'_{had} between $1 - 15$ GeV. The calibration of the hadron energy from the hadron hits, in terms of the Vavilov fit parameters, may further be used to reconstruct the hadron energy for the ICAL physics potential analysis.

The shower shape and spread, in terms of the position vectors of the hits, are further used to reconstruct the average direction of the hadron shower, either by obtaining the direction of the centroid of the shower, or by forming an orientation matrix to take care of the higher order moments. This information enables to study the hadron energy response as a function of the shower direction, which shows marginal direction dependence. The shower spread is also used to discriminate between the DIS and RS events.

The energy and direction of the incident neutrino in CC interaction events, are then reconstructed using the reconstructed information of the muon and the hadrons, via the conservation of the four momentum. The neutrino energy response of the ICAL is in the range $20\% - 25\%$, while the zenith angle resolution is $7° - 15°$. On the other hand, the hadron shower is the only hint of an NC interaction event.

The reach of ICAL is then studied using the correlated information on the muons and the hadrons. A statistical χ^2 analysis procedure, with the events divided in bins

of the muon energy, the muon zenith angle and the hadron energy, is performed, and it is found that the inclusion of the hadron information enhances the ICAL physics potentials by significant amounts. It is found that the ICAL, with 500 kt –yr exposure, would be able to determine the neutrino mass hierarchy with a significance of $\Delta\chi^2_{\text{ICAL}-\text{MH}} \approx 9$, which implies about 40% enhancement over the muon-only analysis. The atmospheric neutrino mixing parameters can also be measured more precisely by the inclusion of hadron energy information. It has been found that, 10 years of running of the ICAL would be able to constrain $\sin^2\theta_{23}$ to a relative 1σ precision of 12% and $|\Delta m^2_{32}|$ to 2.9%.

The time information from the RPC detectors in the ICAL, with respect to the trigger, would be used to determine the direction of the muon track. It would also be used in an approach to measure the average hadron shower direction. The RPC time resolution is about $1 - 1.5$ ns, and an improvement in the time information would make it possible to boost the direction reconstruction of the muons and the hadrons in ICAL. As a part of the extended R&D in ICAL, MRPC detectors, which are much faster as compared to the RPCs, are fabricated and their performance are studied in order to probe their potential in the upgrades of ICAL as well as other applications such as, TOF experiment.

A stack of MRPC detectors, with six sub gaps in each of them, has been developed. The design and construction of these detectors have been optimized after several trials, and they are characterized as a function of various input parameters, e.g., the operating voltage and the gas mixture. The gas mixture has also been optimized to obtain improved efficiency and the time resolution. a time resolution of about 60 ps has been obtained. As a first attempt to probe their potential, the MRPCs have been used in the external trigger system for the characterization of single–gap RPCs. The stack, comprising of three MRPC detectors, is now being operated under stable condition for a substantial time and is ready for further probes.

The work documented in this thesis, has thus facilitated the enhancement of the ICAL potential in attaining its goals. The study of the hadron response of ICAL has been quite effective, as the inclusion of this information has significantly improved the sensitivity of the detector in determining the neutrino mass hierarchy and the atmospheric mixing parameters. The successful development of the MRPC detectors, and their satisfactory performance provides lead to the scope of studying their applications in the future upgradation in the ICAL as well as other experiments that would require faster detectors.

9.2   FUTURE SCOPE

The ability of ICAL in reconstructing the hadron energy and direction has provided plentiful opportunity to extract and use the information to improve on the detector's potential. The work described in this thesis assumes that, the muon and hadron hits in the ICAL are separable with a cent percent efficiency. However, the separation of the muon track and the hadron shower hits would be crucial to use the real data, once ICAL becomes operational. Thus a simulation study to develop an efficient track-shower separation algorithm is important.

The hadron energy response has been obtained using the number of hits in each shower. An attractive alternative approach would be to use the shower shape and spread to reconstruct the energy. A quantity parameterizing the shower shape may be picked to calculate the energy response. A possible improvement in the energy response would provide better sensitivity of the physics study with ICAL. Also, the neutrino response of the ICAL is coarse, and can be improved by stricter cuts, and with possible improvement in the measurements of the muon momentum and the hadron momentum.

The statistical approach, that has been used to study the ICAL physics reach, uses the CC interaction events only. Since partial information on the NC events, in terms of the hadron shower, are also available, this approach may be extended for the NC

events. A possible way to use the NC events would be a one dimensional binning of the events with the observable E'_{had}. The hadron direction resolution may also be included in the further study of both the CC and NC events. Another promising work is to modify the oscillation analysis algorithm to study the ICAL potential to detect the sterile neutrinos.

The MRPC detectors show good stability, good detection efficiency and time resolution, and they are now ready to be tested for possible applications as trigger detector, and in TOF experiments.

Bibliography

[1] W. Pauli, "Letter to the participants of workshop at Tübingen, Germany," (1930).

[2] C. L. Cowan, Jr., *et al.* "Detection of the Free Neutrino: A Confirmation," Science **124**, 103 (1956).

[3] F. Reines and C. L. Cowan, Jr., "The Neutrino," Nature **178**, 446 (1956).

[4] B. Pontecorvo, "Mesonium and anti–mesonium," J.Exptl. Theoret. Phys. **33** (1957) 549 [Sov. Phys. JETP 6 (1958) 429].

[5] B. Pontecorvo, "Inverse beta processes and nonconservation of lepton charge," J.Exptl. Theoret. Phys. **34** (1958) 247 [Sov. Phys. JETP 7 (1958) 172].

[6] M. S. Athar *et al.* [INO Collaboration], "India-based Neutrino Observatory: Project Report. Volume I.," INO-2006-01.

[7] V. M. Datar, S. Jena, S. D. Kalmani, N. K. Mondal, P. Nagaraj, L. V. Reddy, M. Saraf and B. Satyanarayana *et al.*, "Development of glass resistive plate chambers for INO experiment," Nucl. Instrum. Meth. A **602**, 744 (2009).

[8] S. Agostinelli *et al.* [GEANT4 Collaboration], "GEANT4: A Simulation toolkit," Nucl. Instrum. Meth. A **506**, 250 (2003), http://geant4.cern.ch/.

[9] A. Chatterjee, K. K. Meghna, K. Rawat, T. Thakore, V. Bhatnagar, R. Gandhi, D. Indumathi and N. K. Mondal *et al.*, "A Simulations Study of the Muon

Response of the Iron Calorimeter Detector at the India-based Neutrino Observatory," JINST **9**, P07001 (2014) [arXiv:1405.7243 [physics.ins-det]].

[10] M. M. Devi, A. Ghosh, D. Kaur, L. S. Mohan, S. Choubey, A. Dighe, D. Indumathi and S. Kumar *et al.*, "Hadron energy response of the Iron Calorimeter detector at the India-based Neutrino Observatory," JINST **8**, P11003 (2013) [arXiv:1304.5115 [physics.ins-det]].

[11] L. S. Mohan, A. Ghosh, M. M. Devi, D. Kaur, S. Choubey, A. Dighe, D. Indumathi and M. V. N. Murthy *et al.*, "Hadron energy resolution as a function of iron plate thickness at ICAL," JINST **9**, T09003 [arXiv:1401.2779 [physics.ins-det]].

[12] M. M. Devi, L. S. Mohan, A. Dighe, D. Indumathi, "The hadron and neutrino direction resolutions of ICAL," in preparation.

[13] D. Casper, "The Nuance neutrino physics simulation, and the future," Nucl. Phys. Proc. Suppl. **112**, 161 (2002) [hep-ph/0208030]; see also, http://nuint.ps.uci.edu/nuance/.

[14] B. Schorr, "Programs for the Landau and the Vavilov distributions and the corresponding random numbers," Comp. Phys. Commm. **7**, 215 (1974);

[15] A. Rotondi, P. Montagna, "Fast calculation of Vavilov distribution," Nucl. Instrum. Meth. B **47**, 215 (1990).

[16] R. Brun, F. Rademakers and S. Panacek, "ROOT, an object oriented data analysis framework,"

[17] N. I. Fisher *et al.* "Statistical Analysis of Spherical Data," Cambridge University Press [page 32 – 34].

[18] A. Ghosh, T. Thakore and S. Choubey, 'Determining the Neutrino Mass Hierarchy with INO, T2K, NOvA and Reactor Experiments," JHEP **1304**, 009 (2013) [arXiv:1212.1305 [hep-ph]].

[19] T. Thakore, A. Ghosh, S. Choubey and A. Dighe, "The Reach of INO for Atmospheric Neutrino Oscillation Parameters," JHEP **1305**, 058 (2013) [arXiv:1303.2534 [hep-ph]].

[20] M. M. Devi, T. Thakore, S. K. Agarwalla and A. Dighe, "Enhancing sensitivity to neutrino parameters at INO combining muon and hadron information," JHEP **1410**, 189 (2014) [arXiv:1406.3689 [hep-ph]].

[21] M. Honda, T. Kajita, K. Kasahara and S. Midorikawa, "A New calculation of the atmospheric neutrino flux in a 3-dimensional scheme," Phys. Rev. D **70**, 043008 (2004) [astro-ph/0404457].

[22] V. D. Barger, K. Whisnant, S. Pakvasa and R. J. N. Phillips, "Matter effects on three-neutrino oscillations," Phys. Rev. D **22**, 2718 (1980).

[23] D. V. Forero, M. Tortola and J. W. F. Valle, "Neutrino oscillations refitted," [arXiv:1405.7540 [hep-ph]].

[24] NuFIT webpage, http://www.nu-fit.org/.

[25] F. Capozzi, G. L. Fogli, E. Lisi, A. Marrone, D. Montanino and A. Palazzo, "Status of three-neutrino oscillation parameters, circa 2013," Phys. Rev. D **89**, 093018 (2014) [arXiv:1312.2878 [hep-ph]].

[26] M. C. Gonzalez-Garcia and M. Maltoni, "Atmospheric Neutrino Oscillations and New Physics," Phys. Rev. D **70**, 033010 (2004) [hep–ph/0404085].

[27] A. Himmel [SK Collaboration], "Recent results from Super-Kamiokande," AIP Conf. Proc. **1604**, 345 (2014) [arXiv:1310.6677 [hep-ex]].

[28] P. Adamson *et al.* [MINOS Collaboration], "Combined analysis of ν_μ disappearance and $\nu_\mu \to \nu_e$ appearance in MINOS using accelerator and atmospheric neutrinos," Phys. Rev. Lett. **112**, 191801 (2014) [arXiv:1403.0867 [hep-ex]].

[29] K. Abe *et al.* [T2K Collaboration], "Precise Measurement of the Neutrino Mixing Parameter θ_{23} from Muon Neutrino Disappearance in an Off-Axis Beam," Phys. Rev. Lett. **112**, no. 18, 181801 (2014) [arXiv:1403.1532 [hep-ex]].

[30] E. C. Zeballos *et al.*, "A new type of resistive plate chamber: The multigap RPC," Nucl. Instrum. Meth. A **374**, 132–135 (1996).

[31] M. C. S. Williams, "The multigap RPC: the time-of-flight detector for the ALICE experiment," Nucl. Instrum. Meth. A **478**, 183–186 (2002).

[32] A. N. Akindinov et al., "Latest results on the performance of the multigap resistive plate chamber used for the ALICE TOF," Nucl. Instrum. Meth. A **533**, 74–78 (2004).

[33] F. Anghinolfi et al., "NINO: an ultra-fast and low- power front-end amplifier/discriminator ASIC designed for the multigap resistive plate chamber," Nucl. Instrum. Meth. A **533**, 183–187 (2004).

[34] M. M. Devi, N. K. Mondal, B. Satyanarayana, R. R. Shinde, "The development and performance of six–gap glass MRPC detectors," submitted to Nucl. Instrum. Meth. A.

[35] L. Meitner and W. Orthmann, "Über eine absolute Bestimmung der Energie der primären β–Strahlen von Radium E," Z. Phys. **60**, 143–155 (1930).

[36] N. Bohr., "Chemistry and Quantum Theory of Atomic Constitution (Faraday Lecture)," J. Chem. Soc. **135**, 349–384 (1932).

[37] W. Pauli, "Cambridge Monogr. Part. Phys. Nucl. Phys. Cosmol.," **14**, 1–22 (2000).

[38] E. Fermi., "Tentativo di una teoria dei raggi β (in Italian)," La Ricerca Scientifica **2**, 12 (1933).

[39] E. Fermi., "Versuch einer Theorie der beta-Strahlen (in German)," Z. Phys. **88**, 161 (1934).

[40] E. Fermi, "Tentativo di una teoria dei raggi β (in Italian)," Nuovo Cimento **11**, 1–19 (1934).

[41] H. Bethe and R. Peierls, "The Neutrino," Nature **133**, 532 (1934).

[42] G. Danby *et al.*, "Observation of High-Energy Neutrino Reactions and the Existence of Two Kinds of Neutrinos," Phys. Rev. Lett. **9**, 36–44 (1962).

[43] M. Perl *et al.*, "Evidence for Anomalous Lepton Production in e^+e^- Annihilation," Phys. Rev. Lett. **35**, 1489–1492 (1975).

[44] Kodama et al. [DONuT collaboration], "Observation of tau neu- trino interactions," Phys. Lett. B **504**, 218–224 (2001).

[45] T. D. Lee and C.N. Yang, "Question of Parity Conservation in Weak Interactions," Phys. Rev. **104**, 254–258 (1956).

[46] C. S. Wu, E. Ambler, R. W. Hayward, D. D. Hoppes and R. P. Hudson, "Experimental Test of Parity Conservation in Beta Decay," Phys. Rev. **105**, 1413–1414 (1957).

[47] R. P. Feynman and M. Gell-Mann, "Theory of the Fermi Interaction," Phys. Rev. **109**, 193–198 (1958).

[48] E. C. Sudarshan and R. E. Marshak, "Chirality Invariance and the Universal Fermi Interaction," Phys. Rev. **109**, 1860–1862 (1958).

[49] J. J. Sakurai, "Mass Reversal and Weak Interactions," Nuovo Cimento **7**, 649 (1958).

[50] J. N. Bahcall *et al.*, "Solar Neutrinos," I. Theoretical. Phys. Rev. Lett. **12**, 300–302 (1964).

[51] K. Hirata *et al.* [Kamiokande collaboration], "Observation of a neutrino burst from the supernova SN1987A," Phys. Rev. Lett. **58**, 1490–1493 (1987).

[52] R. M. Bionta *et al.* [IMB collaboration], "Observation of a neu- trino burst in coincidence with supernova 1987A in the Large Magellanic Cloud," Phys. Rev. Lett. **58**, 1494–1496 (1987).

[53] E. N. Alekseev *et al.*, "Possible detection of a neutrino signal on 23 February 1987 at the Baksan underground scintillation telescope of the Institute of Nuclear Research," JETP Lett. **45**, 589–592 (1987).

[54] M. G. Aartsen *et al.* [IceCube Collaboration], "First observation of PeV-energy neutrinos with IceCube," Phys. Rev. Lett. **111**, 021103 (2013) [arXiv:1304.5356 [astro-ph.HE]].

[55] M. G. Aartsen *et al.* [IceCube Collaboration], "Evidence for High-Energy Extraterrestrial Neutrinos at the IceCube Detector," Science **342**, 1242856 (2013) [arXiv:1311.5238 [astro-ph.HE]].

[56] M. G. Aartsen *et al.* [IceCube Collaboration], "Observation of High-Energy Astrophysical Neutrinos in Three Years of IceCube Data," Phys. Rev. Lett. **113**, 101101 (2014) [arXiv:1405.5303 [astro-ph.HE]].

[57] T. Araki *et al.* (KamLAND), "Experimental investigation of geologically produced antineutrinos with KamLAND," Nature **436**, 499 (2005).

[58] G. Bellini *et al.* (Borexino), "Observation of Geo-Neutrinos," Phys. Lett. **B687**, 299 (2010), [arXiv:1003.0284 [hep-ex]].

[59] G. Bellini *et al.* (Borexino), "Measurement of geo-neutrinos from 1353 days of Borexino," Phys.Lett. **B722**, 295 (2013), [arXiv:1303.2571 [hep-ex]].

[60] S. Weinberg., "A Model of Leptons," Phys. Rev. Lett. **19**, 1264–1266 (1967).

[61] A. Salam., "Proceedings of the 8th Nobel Symposium on Elementary Particle Theory, Relativistic Groups and Analyticity," Stockholm, Sweden, 367–377 (1969).

[62] S. L. Glashow, "Partial Symmetries of Weak Interactions," Nucl. Phys. **22**, 579–588 (1961).

[63] P. W. Higgs, "Broken symmetries, massless particles and gauge fields," Phys. Lett. **12**, 132–133 (1964).

[64] P. W. Higgs, "Broken Symmetries and the Masses of Gauge Bosons," Phys. Rev. Lett. **13**, 508–509 (1964).

[65] P. W. Higgs, "Spontaneous Symmetry Breakdown without Massless Bosons," Phys. Rev. **145**, 1156–1163 (1966).

[66] F. Englert and R. Brout, "Broken Symmetry and the Mass of Gauge Vector Mesons," Phys. Rev. Lett. **13**, 321–322 (1964).

[67] G. S. Guralnik, C. R. Hagen and T. W. B. Kibble, "Global Conservation Laws and Massless Particles," Phys. Rev. Lett. **13**, 585–587 (1964).

[68] T. W. B. Kibble, "Symmetry breaking in nonAbelian gauge theories," Phys. Rev. **155**, 1554–1561 (1967).

[69] F. J. Hasert *et al.*, "Search for Elastic ν_μ Electron Scattering," Phys. Lett. B **46**, 121–124 (1973);

[70] F. J. Hasert *et al.*, "Observation of Neutrino Like Interactions Without Muon Or Electron in the Gargamelle Neutrino Experiment," Phys. Lett. B **46**, 138–140 (1973);

[71] F. J. Hasert *et al.* (Gargamelle), "Observation of neutrino like interactions without muon or electron in the Gargamelle neutrino experiment," Nucl. Phys. **B73** 1 (1974).

[72] A. C. Benvenuti *et al.*, "Observation of Muonless Neutrino Induced Inelastic Interactions," Phys. Rev. Lett. **32**, 800 (1974).

[73] S. Chatrchyan *et al.* [CMS collaboration], "Observation of a new boson at a mass of 125 GeV with the CMS experiment at the LHC," Phys. Lett. B **716**, 30–61 (2012).

[74] G. Aad *et al.* [ATLAS collaboration], "Observation of a new particle in the search for the Standard Model Higgs boson with the ATLAS detector at the LHC," Phys. Lett. B **716**, 1–29 (2012).

[75] B. Adeva *et al.* [L3 collaboration], "A determination of the properties of the neutral intermediate vector boson Z_0," Phys. Lett. B, **231**, 509–518 (1989).

[76] D. Decamp *et al.* [ALEPH collaboration], "Determination of the number of light neutrino species," Phys. Lett. B **231**, 519–529 (1989).

[77] M. Z. Akrawy *et al.* (OPAL collaboration), "Measurement of the Z_0 mass and width with the opal detector at LEP," Phys. Lett. B **231**, 530–538 (1989).

[78] P. A. Arnio *et al.* [DEPHI collaboration], "Measurement of the mass and width of the Z_0 particle from multihadronic final states produced in $e^- e^+$ annihilations," Phys. Lett. B **231**, 539–547 (1989).

[79] B. Pontecorvo, "Neutrino Experiments and the Problem of Conservation of Leptonic Charge," Sov. Phys. JETP **26**, 984 (1968) [Zh. Eksp. Teor. Fiz. 53, 1717 (1967)].

[80] Z. Maki *et al.*, "Remarks on the Unified Model of Elementary Particles," Prog. Theor. Phys. **28**, 870–880 (1962).

[81] J. Beringer et al. [Particle Data Group], "2013 Review of Particle Physics," Phys. Rev. D86, 010001 (2012) and 2013 partial update for the 2014 edition. (http://pdg.lbl.gov)

[82] L. Wolfenstein., "Neutrino Oscillations In Matter," Phys. Rev. D, **17**, 2369 (1978).

[83] S. P. Mikheev and A.Y. Smirnov, "Resonance Enhancement Of Oscillations In Matter And Solar Neutrino Spectroscopy," Sov. J. Nucl. Phys., **42**, 913–917 (1985).

[84] K. Eguchi *et al.* [KamLAND Collaboration], "First results from KamLAND: Evidence for reactor anti-neutrino disappearance," Phys. Rev. Lett. **90**, 021802 (2003) [hep-ex/0212021].

[85] Y. Fukuda *et al.* (Super-Kamiokande Collaboration), "The Super-Kamiokande detector," Nucl. Instrum. Meth. A **501**, 418–462 (2003).

[86] Q. R. Ahmad *et al.*, "Measurement of the Rate of $\nu_e + d \rightarrow p + p + e^-$ Interactions Produced by ^8B Solar Neutrinos at the Sudbury Neutrino Observatory," Phys. Rev. Lett **87** 071301 (2001).

[87] Q. R. Ahmad *et al.*, "Direct Evidence for Neutrino Flavor Transformation from Neutral Current Interactions in the Sudbury Neutrino Observatory," Phys. Rev. Lett **89**, 011301 (2002).

[88] I. Ambats *et al.* [MINOS Collaboration], "The MINOS Detectors Technical Design Report," NUMI-L-337, FERMILAB-DESIGN-1998-02.

[89] Y. Itow *et al.* [T2K Collaboration], "The JHF-Kamioka neutrino project," [hep-ex/0106019].

[90] F. Ardellier, I. Barabanov, J. C. Barriere, M. Bauer, L. B. Bezrukov, C. Buck, C. Cattadori and B. Courty *et al.*, "Letter of intent for Double-CHOOZ: A Search for the mixing angle θ_{13}," [hep-ex/0405032].

[91] J. K. Ahn *et al.* [RENO Collaboration], "RENO: An Experiment for Neutrino Oscillation Parameter θ_{13} Using Reactor Neutrinos at Yonggwang," [arXiv:1003.1391 [hep-ex]].

[92] X. Guo *et al.* [Daya-Bay Collaboration], "A Precision measurement of the neutrino mixing angle θ_{13} using reactor antineutrinos at Daya-Bay," [hep-ex/0701029].

[93] D. S. Ayres *et al.* [NOvA Collaboration], "NOvA: Proposal to build a 30 kiloton off-axis detector to study nu(mu) —> nu(e) oscillations in the NuMI beamline," [hep-ex/0503053].

[94] T. Araki *et al.* [KamLAND Collaboration], "Measurement of Neu- trino Oscillation with KamLAND: Evidence of Spectral Distortion," Phys. Rev. Lett. **94**, 081801 (2005).

[95] R. Wendell *et al.* [Super-Kamiokande Collaboration], "Atmospheric neutrino oscillation analysis with sub-leading effects in Super-Kamiokande I, II, and III," Phys. Rev. D **81**, 092004 (2010) [arXiv:1002.3471 [hep-ex]].

[96] P. Adamson *et al.* (MINOS), "Improved search for muon-neutrino to electron-neutrino oscillations in MINOS," Phys. Rev. Lett. **107**, 181802 (2011), [arXiv:1108.0015 [hep-ex]].

[97] P. Adamson *et al.* (MINOS), "An improved measurement of muon antineutrino disappearance in MINOS," Phys. Rev. Lett. **108**, 191801 (2012), [arXiv:1202.2772 [hep-ex]].

[98] K. Abe *et al.* (T2K), "First Muon–Neutrino Disappearance Study with an Off–Axis Beam," Phys. Rev. **D85**, 031103 (2012), [arXiv:1201.1386 [hep-ex]].

[99] F. P. An *et al.* [Daya Bay Collaboration], "Spectral measurement of electron antineutrino oscillation amplitude and frequency at Daya Bay," Phys. Rev. Lett. **112**, 061801 (2014) [arXiv:1310.6732 [hep-ex]].

[100] F. P. An *et al.* [Daya Bay Collaboration], "Improved Measurement of Electron Antineutrino Disappearance at Daya Bay," Chin. Phys. C **37**, 011001 (2013) [arXiv:1210.6327 [hep-ex]].

[101] F. P. An *et al.* [DAYA-BAY Collaboration], "Observation of electron-antineutrino disappearance at Daya Bay," Phys. Rev. Lett. **108**, 171803 (2012) [arXiv:1203.1669 [hep-ex]].

[102] J. K. Ahn *et al.* [RENO Collaboration], "Observation of Reactor Electron Antineutrino Disappearance in the RENO Experiment," Phys. Rev. Lett. **108**, 191802 (2012) [arXiv:1204.0626 [hep-ex]].

[103] Y. Abe *et al.* [Double Chooz Collaboration], "Reactor electron antineutrino disappearance in the Double Chooz experiment," Phys. Rev. D **86**, 052008 (2012) [arXiv:1207.6632 [hep-ex]].

[104] Y. Abe *et al.* [DOUBLE-CHOOZ Collaboration], "Indication for the disappearance of reactor electron antineutrinos in the Double Chooz experiment," Phys. Rev. Lett. **108**, 131801 (2012) [arXiv:1112.6353 [hep-ex]].

[105] K. Abe *et al.* [T2K Collaboration], "Observation of Electron Neutrino Appearance in a Muon Neutrino Beam," Phys. Rev. Lett. **112**, 061802 (2014) [arXiv:1311.4750 [hep-ex]].

[106] K. Abe *et al.* [T2K Collaboration], "Evidence of Electron Neutrino Appearance in a Muon Neutrino Beam," Phys. Rev. D **88**, no. 3, 032002 (2013) [arXiv:1304.0841 [hep-ex]].

[107] K. Abe *et al.* [T2K Collaboration], "Indication of Electron Neutrino Appearance from an Accelerator-produced Off-axis Muon Neutrino Beam," Phys. Rev. Lett. **107**, 041801 (2011) [arXiv:1106.2822 [hep-ex]].

[108] P. Adamson *et al.* [MINOS Collaboration], "Electron neutrino and antineutrino appearance in the full MINOS data sample," Phys. Rev. Lett. **110**, no. 17, 171801 (2013) [arXiv:1301.4581 [hep-ex]].

[109] L. Wolfenstein, "Neutrino Oscillations in Matter," Phys.Rev. D **17**, 2369–2374 (1978).

[110] L. Wolfenstein, "Neutrino Oscillations and Stellar Collapse," Phys.Rev. D **20**, 2634–2635 (1979).

[111] V. D. Barger, K. Whisnant, S. Pakvasa, and R. J. N. Phillips, "Matter effects on three–neutrino oscillations," Phys. Rev. D **22**, 2718 (1980).

[112] S. P. Mikheev and A. Y. Smirnov, "Resonance enhancement of oscillations in matter and solar neutrino spectroscopy," Sov. J. Nucl. Phys. **42** 913–917 (1985). [Yad.Fiz.42:1441–1448,1985].

[113] [S. Mikheev and A. Y. Smirnov, "Resonant amplification of neutrino oscillations in matter and solar neutrino spectroscopy," Nuovo Cim. C **9** 17–26 (1986).

[114] M. Blennow and A. Y. Smirnov, "Neutrino propagation in matter," Adv. High Energy Phys. 972485 (2013), [arXiv:1306.2903].

[115] A. Y. Smirnov, "Neutrino mass hierarchy and matter effects," [arXiv:1312.7309].

[116] C. V. Achar *et al.*, "Detection of muons produced by cosmic ray neutrinos deep underground," Phys. Lett. **18**, 196–199 (1965).

[117] C. V. Achar *et al.*, "Observation of a non–elastic cosmic ray neutrino interaction," Phys. Lett. **19**, 78–80 (1965).

[118] R. Santonico and R. Cardarelli, "Development of resistive plate counters," Nucl. Instrum. Methods **187**, 377–380 (1981).

[119] W. R. Leo, "Techniques for Nuclear and Particle Physics Experiments," 2nd Ed., Springer-Verlag, (1994).

[120] B. Satyanarayana, "Design and Characterisation Studies of Resistive Plate Chambers," PhD thesis, (Department of Physics, IIT Bombay, PHY–PHD–10–701, 2009).

[121] J. A. Formaggio and G. P. Zeller, "From eV to EeV: Neutrino Cross Sections Across Energy Scales," Rev. Mod. Phys. **84**, 1307 (2012) [arXiv:1305.7513 [hep-ex]].

[122] Infolytica Corp., Electromagnetic field, http://www.infolytica.com/en/products/magnet/.

[123] R. E. Kalman, "A new approach to linear filtering and prediction problems," Journal of Basic Engineering **82 1**, 35–45 (1960).

[124] J. S. Marshall, "A study of muon neutrino disappearance with the MINOS detectors and the NuMI neutrino beam," PhD. Thesis, Univ. of Cambridge (2008).

[125] E. Wolin and L. Ho, "Covariance Matrices for Track Fitting with the Kalman Filter," Nucl. Instrum. Methods A **329** 493 (1993).

[126] D. Green, "Physics of particle detectors," Cambridge Monographs on Particle Physics, Nuclear Physics and Cosmology, Cambridge University Press, Cambridge U.K. (2000).

[127] D. Green, "Hadron calorimeter performance with a $PbWO_4$ EM compartment," FERMILAB–TM–1958 (1996), http://lss.fnal.gov/archive/test–tm/1000/fermilab–tm–1958.pdf.

[128] C. W. Fabjan, "Calorimetry in high energy physics," CERN–EP/85–54 (1985).

[129] K. Kleinknecht, "Particle detectors," Phys. Rept. **84**, 85 (1982).

[130] A. M. Dziewonski and D. L. Anderson, "Preliminary reference Earth model," Phys. Earth Planet. Interiors **25**, 297 (1981); S. V. Panasyuk, Reference Earth Model (REM) webpage, http://cfauves5.harvrd.edu/lana/rem/index.html.

[131] M. Ribordy and A. Y. Smirnov, "Improving the neutrino mass hierarchy identification with inelasticity measurement in PINGU and ORCA," Phys.Rev. D **87**, 113007 (2013), [arXiv:1303.0758].

[132] R. Bayes, A. Laing, F. Soler, A. Cervera Villanueva, J. Gomez Cadenas, *et al.*, "The Golden Channel at a Neutrino Factory revisited: improved sensitivities from a Magnetised Iron Neutrino Detector," Phys.Rev. D *86* 093015 (2012), [arXiv:1208.2735].

[133] M. Honda, T. Kajita, K. Kasahara and S. Midorikawa, "Improvement of low energy atmospheric neutrino flux calculation using the JAM nuclear interaction model," Phys. Rev. D **83**, 123001 (2011) [arXiv:1102.2688 [astro–ph.HE]].

[134] A. de Gouvea, J. Jenkins, and B. Kayser, "Neutrino mass hierarchy, vacuum oscillations, and vanishing U(e3)," Phys.Rev. D **71**, 113009 (2005), [hep–ph/0503079].

[135] H. Nunokawa, S. J. Parke, and R. Zukanovich Funchal, "Another possible way to determine the neutrino mass hierarchy," Phys.Rev. D **72**, 013009 (2005), [hep–ph/0503283].

[136] E. K. Akhmedov, R. Johansson, M. Lindner, T. Ohlsson and T. Schwetz, "Series expansions for three flavor neutrino oscillation probabilities in matter," JHEP **0404**, 078 (2004) [hep-ph/0402175].

[137] M. Blennow, P. Coloma, P. Huber and T. Schwetz, "Quantifying the sensitivity of oscillation experiments to the neutrino mass ordering," JHEP **1403**, 028 (2014) [arXiv:1311.1822 [hep-ph]].

[138] G. L. Fogli, E. Lisi, A. Marrone, D. Montanino, A. Palazzo and A. M. Rotunno, "Global analysis of neutrino masses, mixings and phases: entering the era of leptonic CP violation searches," Phys. Rev. D **86**, 013012 (2012) [arXiv:1205.5254 [hep-ph]].

[139] S. Choubey and P. Roy, "Probing the deviation from maximal mixing of atmospheric neutrinos," Phys. Rev. D **73**, 013006 (2006) [hep-ph/0509197].

[140] A. Chatterjee, P. Ghoshal, S. Goswami and S. K. Raut, "Octant sensitivity for large theta(13) in atmospheric and long baseline neutrino experiments," JHEP **1306**, 010 (2013) [arXiv:1302.1370 [hep-ph]].

[141] M. Ghosh, P. Ghoshal, S. Goswami and S. K. Raut, "Synergies between neutrino oscillation experiments: an 'adequate' configuration for LBNO," JHEP **1403**, 094 (2014) [arXiv:1308.5979 [hep-ph]].

[142] S. Choubey and A. Ghosh, "Determining the Octant of θ_{23} with PINGU, T2K, NOνA and Reactor Data," JHEP **1311**, 166 (2013) [arXiv:1309.5760 [hep-ph]].

[143] A. Akindinov, F. Anselmo, M. Basile, E. Cerron Zeballos, L. Cifarelli, F. Cindolo, J. Choi and B. Cozzoni *et al.*, "The multigap resistive plate chamber as a time-of-flight detector," Nucl. Instrum. Meth. A **456**, 16 (2000).

[144] A. Akindinov, A. Alici, F. Anselmo, P. Antonioli *et al.*, "Latest results on the performance of the multigap resistive plate chamber used for the ALICE TOF," Nucl. Instrum. Meth. A **533**, 74–78 (2004).

[145] Y. Wang *et al.*, "Study on the performance of multigap resistive plate chambers," Nucl. Instrum. Meth. A **538**, 425–430 (2005).

[146] S. Narita et al, "Construction and performance of multigap RPC in streamer and avalanche modes," Nucl. Instrum. Meth. A **602**, 814–816 (2009).

[147] B. Bonner *et al.*, "A single Time-of-Flight tray based on multigap resistive plate chambers for the STAR experiment at RHIC," Nucl. Instrum. Meth. A **508**, 181–184 (2003).

[148] A. Akindinov, A. Alici, F. Anselmo, P. Antonioli *et al.*, "Study of gas mixtures and ageing of the multigap resistive plate chamber used for the ALICE TOF," Nucl. Instrum. Meth. A **533**, 93–97 (2004).